

**DESIGN AND DEVELOPMENT OF FAULT TOLERANT
FLUSH AIR DATA SENSING (FADS) SYSTEM**

A Dissertation Presented to
The Department of Mechanical and Control Engineering

by

GOSSAMSETTI Guna Surendra

In Partial Fulfillment
of the Requirements for the Degree of
Doctor of Engineering in Faculty of Engineering

at

Kyushu Institute of Technology
[March 2019 of GRADUATION]

COPYRIGHT © 2019 BY [GOSSAMSETTI GUNA SURENDRA]

DESIGN AND DEVELOPMENT OF FAULT TOLERANT FLUSH AIR DATA SENSING (FADS) SYSTEM

Dissertation Committee:

Dr. Yonemoto Koichi,
Department of Mechanical and Control Engineering
Kyushu Institute of Technology

Dr. Tsuboyi Nobuyuki,
Department of Mechanical and Control Engineering
Kyushu Institute of Technology

Dr. Kurogi Shuichi,
Department of Mechanical and Control Engineering
Kyushu Institute of Technology

Dr. Honda Takashi,
Department of Applied Science for Integrated
System Engineering
Kyushu Institute of Technology

Date Approved: February 13, 2019

ACKNOWLEDGEMENTS

First and foremost, I would like to express my sincerest gratitude to my guru and supervisor Professor Yonemoto and Assistant Professor Fujikawa, who, through their impeccable sense of leadership, patiently and kindly supported me in my research and helped me broaden my knowledge and skills in reusable space transportation technology, systems engineering, team work and management, diplomacy, and more. I would also like to thank my dissertation committee members Professor Tsuboyi, Professor Kurogi and Professor Honda for their precious time and interest in this research. I would also like to acknowledge Prof. Nonaka and Mr. Yamauchi of JAXA-ISAS center for allowing me to conduct wind tunnel experiments.

I would also like to express my heartfelt appreciation to the members of the Space Systems Laboratory, whose insightful questions and comments during research seminars helped improving the work hereafter presented. Special thanks to Mr. Ichige, Mr. Ura, Mr. Thibault, Mr. Moriyama and Mr. Bruno who helped significantly in my research. My heartfelt appreciation also goes to Ms. Nakamoto and other non-teaching staff of the mechanical department and student affairs department, who helped me throughout my stay at Kyushu Institute of Technology. I also want to acknowledge Assuran Foundation for providing me with their scholarship.

Finally, my greatest indebtedness goes to my mother, Venkata Kanaka Durga, my father, Venkanna Babu, my Japanese mother Kumiko, my Japanese father Nojima, my brother, Hiteswar, my cousin Keerthana and other family members for supporting me and showing me the path to grow as a strong, independent, and capable person. Words cannot express for all of the sacrifices that were made on my behalf.

TABLE OF CONTENTS

ACKNOWLEDGEMENTS	iii
LIST OF TABLES	vi
LIST OF FIGURES	vii
LIST OF SYMBOLS AND ABBREVIATIONS	ix
SUMMARY	x
CHAPTER 1. Introduction	1
1.1 Overview of WIRES Project	6
1.1.1 Development Status of WIRES#013	9
1.1.2 Development Status of WIRES#015	10
1.1.3 Future Concepts for WIRES Project	12
1.2 Air Data Sensing System	13
1.3 Previous Research for Air Data Sensing System	16
1.3.1 Calculation of Calibration Coefficients	17
1.3.2 Calculation of Physical Quantities	22
1.4 Drawbacks of Research	25
CHAPTER 2. Wind Tunnel Experiments	26
2.1 Objective of the Experiments	26
2.1.1 FADS Wind Tunnel Test Model	26
2.1.2 Wind Tunnel Test Facility	30
2.2 Wind Tunnel Test Conditions	32
CHAPTER 3. AIR DATA SENSING ALGORITHM	35
3.1 Flush Air Data Sensing Pressure and Geometric Model	35
3.2 Flush Air Data Sensing Estimating Algorithm	39
3.2.1 The Triples Equation	41
3.2.2 Angle of Attack Triples Estimator	42
3.2.3 Sideslip Angle Triples Estimator	44
3.2.4 Incident Angle Estimations and Flow Correction Angles	46
3.2.5 Calibration Coefficient	46
3.2.6 Mach Number, Static Pressure, and Impact Pressure Estimator	48
3.3 Evaluation of the FADS Calibration	51
3.3.1 Angle of Attack Calibration	51
3.3.2 Sideslip Angle Calibration	52
3.3.3 Position Error ε Calibration	52
CHAPTER 4. Results and Analysis	54
4.1 Results of the Estimation Algorithm	54
4.1.1 Surface Pressure Distribution Results	54
4.1.2 Estimation for Calibration Coefficient ε	56
4.2 Analysis of the Estimation Results	63
4.2.1 Estimated Result of Local Sideslip Angle	63
4.2.2 Evaluation of Calibration Coefficient using Theoretical Approach	69

4.2.3	Features of Singularity	74
4.3	Countermeasures for Singularity	76
4.3.1	Cause of Singularity	76
4.3.2	Measures for Singularity	82
CHAPTER 5.	Fault tolerance Capability and Results	84
5.1	Concept of Fault Tolerance Capability	84
5.2	Fault Detection and Isolation Scheme	86
5.2.1	Fault Detection and Isolation for Pressure Ports	86
5.2.2	Fault Detection and Isolation in Estimation of Angle of Attack	89
5.2.3	Fault Detection and Isolation in Estimation of sideslip angle	90
5.3	Simulation Conditions of the Fault Tolerant Flush Air data Algorithm	92
5.4	Results of the Fault Tolerant Flush Air data Sensing Algorithm	93
5.4.1	Estimation Results for One Sensor Failure on Vertical Meridian When Mach Number 0.8	93
5.4.2	Estimation Results for One Sensor Failure on Vertical Meridian When Mach Number 1.0	95
5.4.3	Estimation Results for One Sensor Failure on Vertical Meridian When Mach Number 2.0	97
5.4.4	Estimation Results for Two Sensor Failure on Vertical Meridian When Mach Number 0.8	99
5.4.5	Estimation Results for One Sensor Failure on Vertical Meridian and Horizontal Meridian When Mach Number 0.8	101
CHAPTER 6.	ConclusionS	104
REFERENCES		108

LIST OF TABLES

Table 1 – Major specifications of WIRES#013 vehicle	10
Table 2 – Major specifications of WIRES#015 vehicle	12
Table 3 – Specifications of the wind tunnel facility	31
Table 4 – Test conditions carried out	33
Table 5 – Detailed wind tunnel test conditions	34
Table 6 – Pressure port position ϕ_i, λ_i	37
Table 7 – Pressure port combination and geometric angle of each port for angle of attack estimation	42
Table 8 – Pressure port combination and geometric angle of each port for sideslip angle estimation	44
Table 9 – Sideslip angle estimation for each port combination at $M=0.9$ (2015)	65
Table 10 – Sideslip angle estimation for each port combination at $M=0.5$	68
Table 11 – Sideslip angle estimation for each port combination at $M=1.0$	69
Table 12 – Local angle of attack estimates ($\beta_{target}=0$ [deg.], $M=0.5$)	73
Table 13 – Local sideslip angle estimates ($\beta_{target}=0$ [deg.], $M=0.5$)	74
Table 14 – Similarity of singularity in local slip angle estimation by theoretical pressure distribution	75
Table 15 – Value of A when estimating local angle of attack α_e	77
Table 16 – Calculated pressure measurement by the theoretical pressure distribution [kPa] ($M = 0.5$)	78
Table 17 – Conditions when singularity points occur	80
Table 18 – Value of A' when estimating local sideslip angle β_e	80
Table 19 – Calculated pressure measurement by the theoretical pressure distribution [kPa] ($M = 0.5$)	81

LIST OF FIGURES

Figure 1 – V-2 Rocket launched from test stand in 1943 (©GFA)	2
Figure 2 – First Human Landing on Moon Apollo 11 (©NASA)	2
Figure 3 – First flight of Spaceship One with White Knight mother vehicle (©Scaled Composites)	4
Figure 4 – Falcon 9 rocket lifts off from launch complex at Cape Canaveral (©SpaceX)	4
Figure 5 – HOPE-X launch vehicle of JAXA (©JAXA)	6
Figure 6 – Current development roadmap of WIRES project	7
Figure 7 – Validation tests of WIRES#014	8
Figure 8 – Future rocket consortium for the development of WIRES#013 and WIRES#015	9
Figure 9 – Overview of WIRES#013 vehicle	10
Figure 10 – Overview of WIRES#015 vehicle	11
Figure 11 – Future roadmap of WIRES project	13
Figure 12 - Shock wave propagation on sharp and blunt object	14
Figure 13 – Artistic depiction of WIRES and HYFLEX vehicles during re-entry (©JAXA)	15
Figure 14 – Conceptual design and wind tunnel test model of X-33 vehicle (©NASA)	15
Figure 15 – HYFLEX hypersonic flight experiment vehicle (©JAXA)	15
Figure 16 – FADS wind tunnel model of Todaka’s method	16
Figure 17 – Flowchart algorithm of FADS proposed by Todaka using Suenaga and Tashiro’s method	17
Figure 18 – Conical Pitot tube in Suenaga's method	18
Figure 19 – Pressure holes selection for calculating the coefficients of angle of attack sideslip angle	21
Figure 20 – View of FADS wind tunnel test model (front and side view)	27
Figure 21 – Drawing of FADS wind tunnel test model	28
Figure 22 - Position of pressure port	28
Figure 23 – Schlieren images taken during the wind tunnel experiments	29
Figure 24 – Schlieren images and pressure distribution comparison between the two wind tunnel experiments	29
Figure 25 – Subsonic (left) and supersonic (right) wind tunnel test facility of JAXA/ISAS	31
Figure 26 – Schematics of the wind tunnel facility	32
Figure 27 – Straight sting (left) and vent sting (right)	32
Figure 28 – Phase shift of roll angle 45 [deg.]	34
Figure 29 – Location of the pressure ports	37
Figure 30 – Calibration coefficients and estimation algorithms of FADS using NASA method	40
Figure 31 – Pressure port combination for angle of attack estimation	42
Figure 32 – Pressure port combination for sideslip angle estimation	44
Figure 33 – Color arrangement of pressure ports	55
Figure 34 – Pressure distribution measurements for various Mach numbers	55
Figure 35 – Local angle of attack and local sideslip angle estimation results for M=0.5	57

Figure 36 – Local angle of attack and local sideslip angle estimation results for M=0.9	57
Figure 37 – Local angle of attack and local sideslip angle estimation results for M1.0	58
Figure 38 – Local angle of attack and local sideslip angle estimation results for M2.0	58
Figure 39 – Results of incident angle θ_i ($\beta_{ref} = 0$ [deg.])	59
Figure 40 – Results of estimated calibration coefficient ε ($\beta_{ref} = 0, 2, 4$) [deg.]	60
Figure 41 – Calibrated angle of attack and sideslip angle results at $M=0.5$	61
Figure 42 – Calibrated angle of attack and sideslip angle results at $M=0.9$	61
Figure 43 – Calibrated angle of attack and sideslip angle results at $M=1.0$	62
Figure 44 – Calibrated angle of attack and sideslip angle results at $M=2.0$	62
Figure 45 – Dispersion of estimated sideslip angle	63
Figure 46 – Symmetry and asymmetry port combination for sideslip angle estimation	64
Figure 47 – Local Sideslip angle deviation at $M=0.9$ ($\beta_{ref} = 0$ [deg.])	66
Figure 48 – Local Sideslip angle deviation at $M=0.9$ ($\beta_{ref} = 2$ [deg.])	66
Figure 49 – Local Sideslip angle deviation at $M=0.9$ ($\beta_{ref} = 4$ [deg.])	66
Figure 50 – C_{pc} measured v.s. estimated value at $M=0.5$	71
Figure 51 – C_{pc} measured v.s. estimated value at $M=0.9$	71
Figure 52 – C_{pc} measured v.s. estimated value at $M=1.0$	72
Figure 53 – Combination of pressure holes where singularity point occurs	78
Figure 54 – Combination of pressure holes where singularity point occurs	82
Figure 55 – Port combinations for fault tolerance	85
Figure 56 – Various fault detection methods for single and multiple signals	85
Figure 57 – Change detection method for identifying the pressure sensor faults	87
Figure 58 – Fault detection case for one sensor failure (port 6)	88
Figure 59 – Fault detection case for two sensors failure (port 6 and 8)	88
Figure 60 – Pressure port combination for angle of attack estimation with fault tolerance	89
Figure 61 – Calibrated angle of attack and sideslip angle estimation results for M=0.8 (case 1)	94
Figure 62 – Mach estimation results for M=0.8 (case 1)	95
Figure 63 – Calibrated angle of attack and sideslip angle estimation results for M=1.0 (case 1)	96
Figure 64 - Mach estimation results for M=1.0 (case 1)	97
Figure 65 – Calibrated angle of attack and sideslip angle estimation results for M=2.0 (case 1)	98
Figure 66 – Mach estimation results for M=2.0 (case 1)	99
Figure 67 – Calibrated angle of attack and sideslip angle estimation results for M=0.8 (case 2)	100
Figure 68 – Mach estimation results for M=0.8 (case 2)	101
Figure 69 – Calibrated angle of attack and sideslip angle estimation results for M=0.8 (case 3)	102
Figure 70 – Mach estimation results for M=0.8 (case 3)	103

LIST OF SYMBOLS AND ABBREVIATIONS

p	: port pressure
P_∞	: free stream static pressure
q_c	: impact pressure
α	: angle of attack
α_e	: local angle of attack
α_∞	: free stream angle of attack
β	: sideslip angle
β_e	: local sideslip angle
β_∞	: free stream sideslip angle
$\delta\alpha$: angle of attack correction term
$\delta\beta$: sideslip angle correction term
θ	: local flow incident angle
ϕ	: clock angle of FADS port
λ	: cone angle of FADS port
Γ	: pressure difference of FADS port
ε	: position error calibration coefficient
M_∞	: free stream Mach number
γ	: specific heat ratio
i	: port index
j	: port index
k	: port index

SUMMARY

The primary goal of single-stage-to-orbit technology is to reduce the cost of transportation to and from space radically. The winged rocket developed by Kyushu Institute of Technology is a test bed and technology demonstrator for this effort. Winged rocket is one of the ideal types of space transportation system that has a high potential of reusability, operational flexibility including abort making it possible to fly back to its launch point. This vehicle can be the pioneer for the future space transportation such as cargo and human space flight. To successfully complete these missions, estimation of air data parameters such as angle of attack, Sideslip angle, Mach number and dynamic pressure during the flight is essential. Conventional pitot tubes are not suitable for operation in re-entry flight environments due to extreme heating of the nose with small radius. Therefore the concept of FADS (Flush Air Data Sensing) system, by which the aerodynamic pressure is measured on the airframe surfaces, has been proposed. This air data sensing system allows the continuous operation of high temperature supersonic and hypersonic re-entry flight. However, in the extreme thermal environment, pressure ports and sensors still have a high risk of failure that makes the acquisition of the air data unreliable, to result in loss of flight controllability. This research proposes innovative fault tolerant FADS by utilizing a large number of pressure holes on the airframe nose.

Chapter 1 discusses the outline and importance of this research based on the background of previous researches.

Chapter 2 discusses the FADS wind tunnel test model with 17 pressure holes and test cases carried out for calibration of air data estimation.

Chapter 3 discusses the air data estimation algorithm using the geometric model and aerodynamic models to calculate the angle of attack, Sideslip angle, Mach number and dynamic pressure. To perform this estimation, the air data must be related to the surface pressures by the aerodynamic model that covers over a wide range of Mach number, which is derived from the closed form potential flow solution for a blunt body applicable to subsonic speeds and the modified Newtonian flow model applicable to hypersonic speeds. Both the potential flow and the Newtonian flow describe the surface pressure at each port in terms of the geometrical incident flow angle. On the other hand, the geometric model represents the location of the pressure ports of the FADS wind tunnel test model. Based on the geometric model and aerodynamic model of the FADS, the aerodynamic parameters such as angle of attack, Sideslip angle, Mach number and dynamic pressure are estimated by the selection of some sets of various pressure port combinations. Since there are four aerodynamic parameters and a calibration parameter of the aerodynamic model to be estimated, at least five surface pressure port measurements must be available to derive the entire air data state. Using five pressure measurements to estimate the air data is equivalent to a high order spline fit and results in an air data estimating algorithm, which is sensitive to noise in the measured pressures. Providing an additional sixth sensing location mitigates the noise sensitivity, increases redundancy options, and results in a system that gives overall superior performance. On the other hand, wind tunnel test data, which have been performed for various speeds in both subsonic and supersonic regions with different angle of attack and sideslip angle, are used for the validation and calibration of the wind test model. Once the air data parameters are estimated, it is necessary to correct the mainstream angle of attack and the Sideslip angle using the flow correction angle parameters derived from the wind tunnel data. Additionally, a

shape and compressibility parameter also called as calibration coefficient is estimated with respect to various Mach number and angle of attack.

Chapter 4 discusses the results and analysis of the estimation algorithm carried out using the wind tunnel test data, and the improvements made for the estimation algorithm based on the analysis is proposed. It is found that the accuracy of the Sideslip angle deteriorates as high the angle of attack increases. In order to understand the cause of the deterioration, a theoretical approach using the pressure distribution method was employed. In this method, the pressure at each port is estimated using the geometrical and aerodynamic model for various speeds and attitudes which is the inverse of the FADS estimation algorithm. From this study, it was understood that at some particular attitude of the FADS module the pressure at some of the ports was equal. During the estimation of angle of attack or Sideslip angle, we select some sets of pressure port combinations and in these combinations if two surface pressure ports have same value, the expression for estimation will become indefinite. This causes the indeterminate values called singularity points, when estimating angle of attack and Sideslip angle. It was understood that, these singularity points are the reason for deterioration of the sideslip angle accuracy at higher angle of attack.

Chapter 5 discusses the fault tolerance capability of the FADS system for the fault detection and isolation scheme when singularity points arise during flight. To overcome this issue, the selection of appropriate ports and increasing the number of ports from 6 to 9 for the estimation is one of the suitable solutions for improving the accuracy and fault tolerance. Therefore, for angle of attack estimation 10 combinations of pressure ports and for sideslip angle estimation 55 combinations can be employed in the algorithm. When the port combinations are increased, there is a

wide selection of combinations for various attitudes of the flight to eliminate the combinations that cause the singularity and still achieve the accuracy. Additionally, the FADS hardware for WIRES vehicles is summarized in this section.

Chapter 6 summarizes the research results of the algorithm with the fault tolerance capability and future works to be carried out in this field are included.

CHAPTER 1. INTRODUCTION

Humans have always fascinated to reach the stars, explore the space ever since the beginning of the civilization. This is particularly significant because it is humanity's least explored frontier. Human space exploration helps to address fundamental questions about our place in the Universe and the history of our solar system. Through addressing the challenges related to human space exploration we expand technology, create new industries, and help to foster a peaceful connection with other nations. Curiosity and exploration are vital to the human spirit and accepting the challenge of going deeper into space.

The journey to space started during the World War II with the testing of V2 rockets like Figure 1 below, which became the first human-made objects in space on June 20, 1944. After the war, the scientists developed the rockets for both military and civilian research. The space race began in 1950s with the development of satellites and launch vehicles increasing rapidly with Soviet Union launching the first artificial satellite Sputnik 1 on October 4, 1957, first human Yuri Gagarin in earth orbit on April 12, 1961. The "race" peaked with the July 20, 1969, US landing of the first humans on the Moon with Apollo 11 (in Figure 2). The USSR attempted several crewed lunar missions but eventually canceled them and concentrated on Earth orbital space stations. A period of détente followed with the April 1972 agreement on a cooperative Apollo–Soyuz Test Project, resulting in the July 1975 rendezvous in Earth orbit of a US astronaut crew with a Soviet cosmonaut crew. The end of the Space Race is harder to pinpoint than its beginning, but it was over by the December 1991 dissolution of the Soviet Union, after which spaceflight cooperation between the US and Russia flourished. The Space Race has left a legacy of Earth communications and

weather satellites, and continuing human space presence on the International Space Station. It has also sparked increases in spending on education and research and development, which led to beneficial spin-off technologies.



Figure 1 – V-2 Rocket launched from test stand in 1943 (©GFA)



Figure 2 – First Human Landing on Moon Apollo 11 (©NASA)

Also, many private organizations started their business ventures in the space transportation system which started the so called private space race (NewSpace). This private industry space race of the 21st century involves sounding rockets to the ignerosphere (mesosphere and thermosphere), orbital launch rockets, and suborbital

tourist spaceflights. In the 1990s, Peter Diamandis, dissolute with the state of space development, decided to spur it on and spark the suborbital space tourism market, by initiating a prize, the X Prize. This led to Paul Allen becoming involved in the competition, creating the Scaled Composites Tier One platform of SpaceShip One and White Knight One (in Figure 3) which won the Ansari X-Prize in the 2000s. The technology of the winning entrant was then licensed by Richard Branson's Virgin Group as a basis to found Virgin Galactic. The base techniques of Tier One also form the basis for Stratolaunch Systems of Vulcan Aerospace. Elon Musk, founder of Space X accelerated this race with successful launch of his “Falcon 9” rocket in May 25, 2012 (in Figure 4) followed by Blue Origin owned by Jeff Bezos launched their test vehicle “New Shepard” on April 29, 2015.



**Figure 3 – First flight of SpaceShip One with White Knight mother vehicle
(©Scaled Composites)**



**Figure 4 – Falcon 9 rocket lifts off from launch complex at Cape Canaveral
(©SpaceX)**

The billionaire space race shows the aims of billionaires extend beyond just fulfilling government contracts, with their own gilding of the space age, in extending capabilities and their own luster. However, one of the major hurdles in this new space race is the cost per flight which can be achieved by reusability and the reliability of the launch vehicles.

Humans are on the threshold of exploring space in new and sustainable ways which are very different from the current space missions. The need for reliable launch vehicle for various missions is evident. Along with technology requirement to achieve this feat, one of the major hurdles for space travel is cost per flight. This cost can be reduced if the same launch vehicle can be reused for multiple launches which is concept for the airline industries. Many organizations are developing reusable launch vehicles such as Falcon 9 of Space X, New Sheppard of Blue Origin, SpaceShip Two of Virgin Galactic are some examples. But the requirements of complex infrastructure or not fully reusable are some of the setbacks in these vehicles. For instance in falcon 9 vehicles, a landing zone and complex vertical landing system where engine re-ignition is needed. For SpaceShip Two, a mother vehicle and complex ground support system is needed. Therefore, there is a need to develop a simple fully reusable launch vehicle.

Since 2005, Kyushu Institute of Technology has been designing and developing sub-scale rockets to validate the necessary technologies for reusable suborbital winged launch vehicle called WIRES (WInged REusable Sounding) rocket. Consolidating the research experience of HIMES and HOPE-X (in Figure 5) launch vehicles studied by ISAS of JAXA in 1980s and 1990s, the winged rocket project is in the forefront of the Japanese reusable space vehicles. Winged rocket is one of the ideal types of space transportation system that has a high potential of reusability, operational flexibility including abort making it possible to fly back to its launch point. All the essential technologies demonstrated on the WIRES vehicle will be employed to develop the future reusable space transportation systems.



Figure 5 – HOPE-X launch vehicle of JAXA (©JAXA)

1.1 Overview of WIRES Project

WIRES vehicle employs the original aerodynamic shape of the HIMES, as essential aerodynamic research has been carried out by ISAS which cleared the initial hiccup of determining the shape for the vehicle. The research showed that, the HIMES vehicle shape has stability, high lift to drag ratio, trim capability from subsonic to supersonic regime, and employing a wing can increase the maneuverability and glide capability. From 2008, flight tests have been carried out to validate the various technologies such as attitude control system, two stage recovery system using parachutes and parafoil on sub-scale version of WIRES vehicles. Fundamental researches on aerodynamics, advanced NGC, cryogenic composite tanks are currently studied for future application on WIRES vehicles. This step by step approach will facilitate to resolve all the technology hurdles and gain operational experience to launch such rockets. Currently, three experimental vehicles are in the operational phase (WIRES#014-3A) and design phase (WIRES#013 and WIRES#015) as shown in Figure 6.

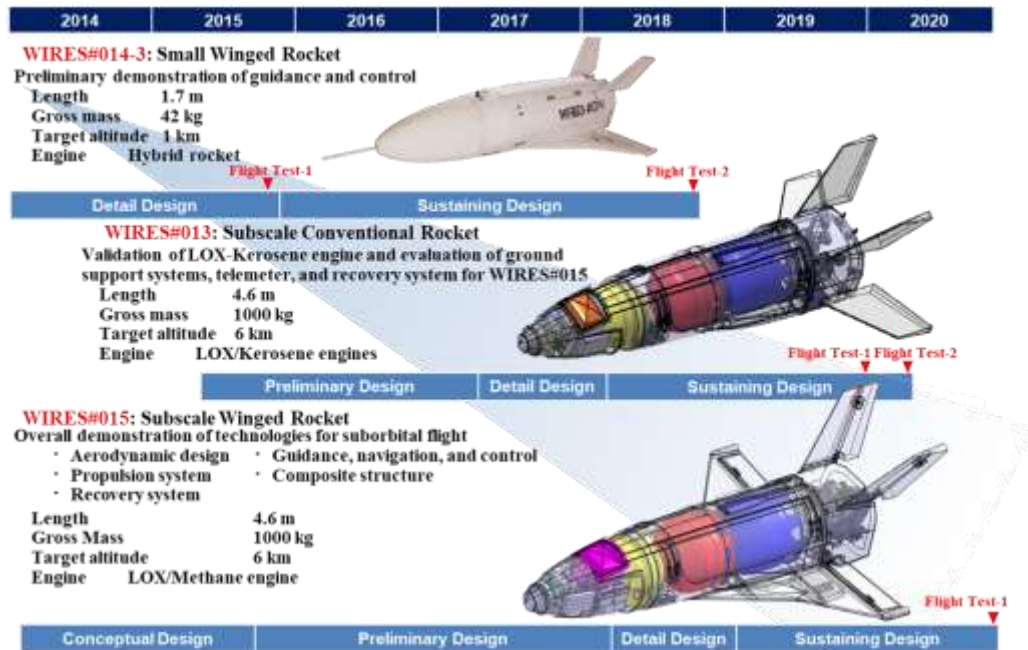


Figure 6 – Current development roadmap of WIRES project

Since 2012, Kyutech has been developing WIRES#014^[1,], which has a total length of 1.7 m and a weight of 42kg. The objective of this vehicle is to demonstrate the preliminary technology of onboard autonomous NGC system in collaboration with JAXA. During the development of WIRES#014, three variants have been fabricated with improvement in each subsystem. For WIRES#014-1, the structure had a skin, longeron and frame and employed CAMUI hybrid rocket engine of Hokkaido University. The flight test was conducted in 2013, but failed its controlled flight due to the malfunction of ADS system. Next WIRES#014-2 was fabricated and had a monocoque structure reducing the structural weight without any loss of strength and employed a simpler COTS hybrid rocket engine Hypertek M1000. However, during the ground combustion in 2014, the vehicle was lost due to the unexpected explosion caused due to the failure of the engine nozzle. Finally in 2015, authors have fabricated WIRES#014-3, made additional reinforcement to the Hypertek M1000 nozzle which caused the previous explosion. The flight test was conducted and the vehicle was

successfully recovered using the two stage parachute system. Figure 7 shows the validation test of all the three variants of WIRES#014. These vehicles are jointly developed with various academia, industries and national agencies.



Figure 7 – Validation tests of WIRES#014

Currently, to validate the reusability and rectify minor issues revealed during the post flight analysis such as leak in air data sensing system resulting in malfunctioning of ADS, poor attitude controllability due to the insufficient performance of control surface actuators, and failure of emergency telemeter transmission due to the inappropriate installation of antennas both on board and ground from the previous flight test, WIRES#014-3A is under final development and testing phase and is expected to be launched in March, 2019. In the initial half of this paper, authors will discuss the development progress of WIRES#013 and WIRES#015^[2, 3, 4] developed in collaboration with the member institutions of Future Rocket Research Consortium (in Figure 8), such as JAXA, Kawasaki Heavy Industries Ltd., IHI, IHI Aerospace, Toray Carbon Magic Inc., Chugoku Kogyo Ltd., and Xenocross Corporation. USC is working along with this consortium in the development of WIRES#013.

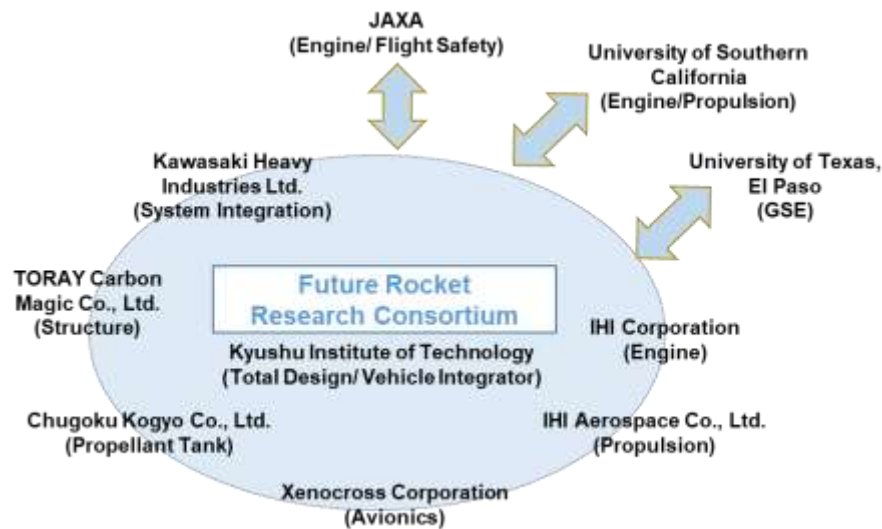


Figure 8 – Future rocket consortium for the development of WIRES#013 and WIRES#015

1.1.1 Development Status of WIRES#013

WIRES#013 is a subscale non-winged rocket, propelled by two LOX-Kerosene engines of total 20kN thrust provided by USC as test bed for the winged WIRES#015 vehicle. It has the total length of 4.6m, with a lift-off mass of 1000kg and expected to reach the altitude of about 6km. WIRES#013 does not have aerodynamic control surfaces, and guidance and control will not be performed. However, there is a consideration to employ reaction control system for attitude control at apogee. This vehicle is expected to be launched in March 2020.

The mission objectives for this vehicle are as follows:

- Validation of LOX-Kerosene engines
- Recovery system using 2 stage parachutes and airbags
- Reaction control system for attitude control at the apogee
- Telemeter and ground communication system
- Ground support equipment

The major specifications and overview of the vehicle are shown in Figure 9 and Table 1.

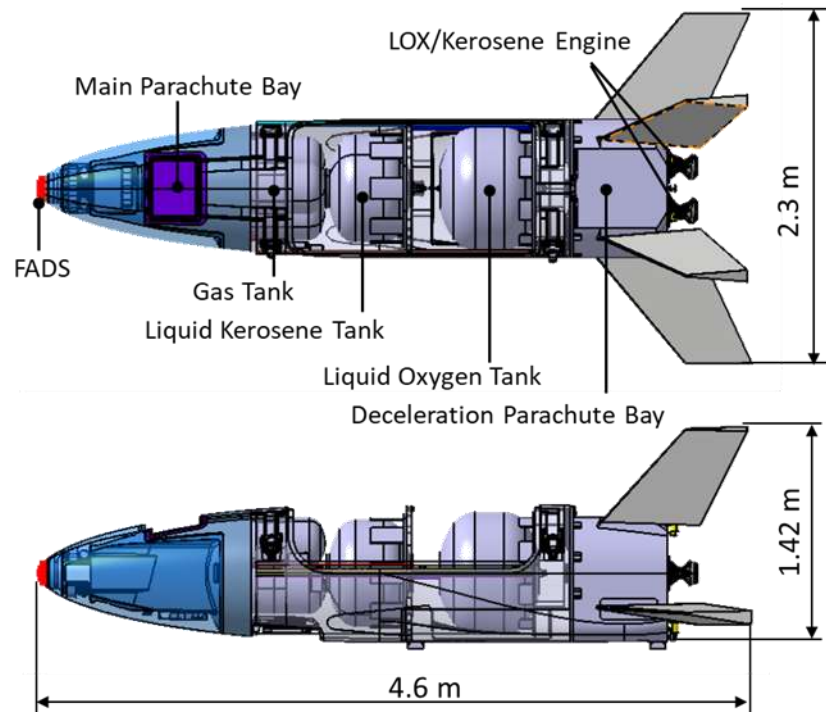


Figure 9 – Overview of WIRES#013 vehicle

Table 1 – Major specifications of WIRES#013 vehicle

Major Specifications	
Initial mass (kg)	1000
Total length (m)	4.6
Maximum thrust (kN)	10 x 2
Combustion duration (s)	25~
Maximum altitude (km)	6
Engine	2 Liquid Oxygen and Kerosene

1.1.2 Development Status of WIRES#015

WIRES#015 is a subscale winged rocket, propelled by LOX-Methane engine with 20kN thrust provided by JAXA. It has the total length of 4.6m, with a lift-off mass of 1000kg and expected to reach the altitude of about 6km. The purpose of

WIRES#015 is to validate the major critical technologies for the suborbital flight.

This vehicle is expected to be launched in March, 2021.

The mission objectives for this vehicle are as follows:

- Validation of LOX-Methane engine
- Advanced nonlinear flight control system
- Real-time optimal flight guidance system
- Recovery system using 2 stage parachutes and airbags
- Reaction control system for attitude control at the apogee

The major specifications and overview of the vehicle are shown in Figure 10 and Table 2.

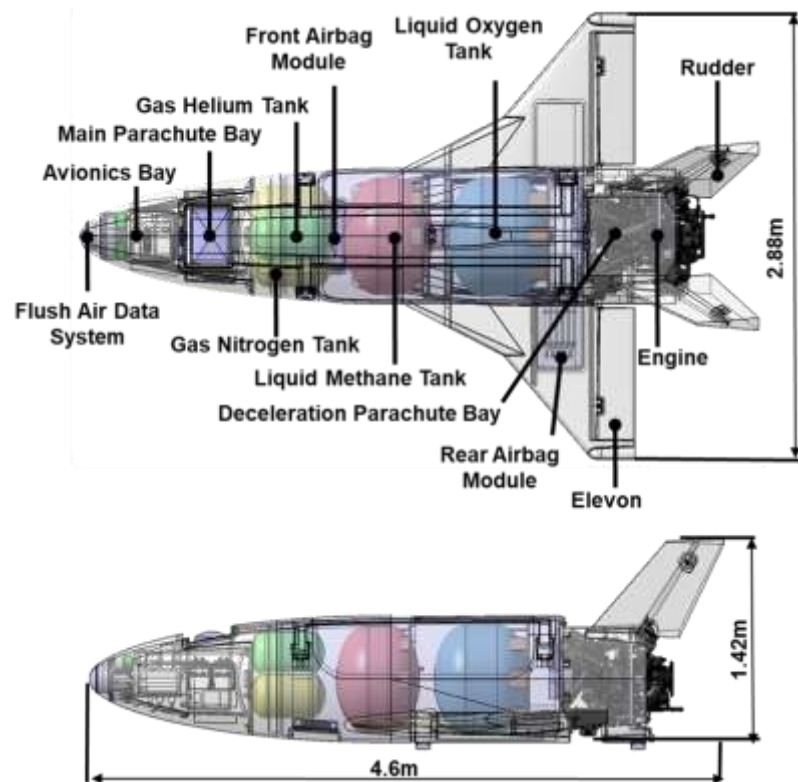


Figure 10 – Overview of WIRES#015 vehicle

Table 2 – Major specifications of WIRES#015 vehicle

Major Specifications	
Initial mass (kg)	1000
Total length (m)	4.6
Maximum thrust (kN)	20 → 13
Combustion duration (s)	30
Maximum altitude (km)	6
Engine	
Liquid Oxygen and Methane	

1.1.3 Future Concepts for WIRES Project

The WIRES#013 will be fabricated and shipped to United States by mid-2019, and the first flight test is planned in March, 2020. Subsequently, the flight test of WIRES#015 will be conducted in March, 2021 in order to validate major necessary technologies for the future reusable suborbital vehicle. These technologies will be applied to unmanned and manned suborbital space vehicles of Space Walker Inc., whose conceptual development studies are currently conducted by the authors as well. The first flight of the suborbital spaceplane for scientific research will be in 2022 and put into operational services from 2023. The next suborbital plane for small satellite launch will have its first flight test in 2024 to put into the operational services in 2025. The final suborbital spaceplane for space tourism makes its first flight test in 2026 and commercially operated from 2027. The future road map is shown in Figure 11.

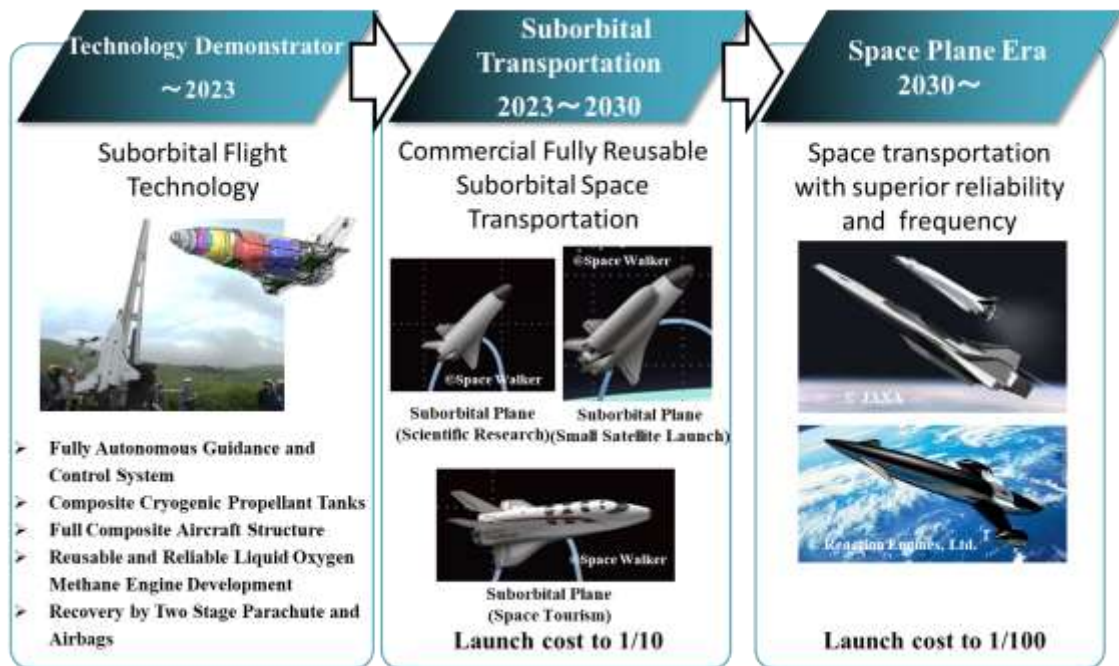


Figure 11 – Future roadmap of WIRES project

1.2 Air Data Sensing System

The primary goal of Single-Stage-to-Orbit technology is to radically reduce the cost of transportation to and from space. Already, many private organizations are developing reusable space planes for commercial use. Since 2005, the Kyushu Institute of Technology, Japan has been developing a suborbital winged rocket called WIRES (Winged Reusable Sounding rocket) for use in research projects of future, fully reusable space transportation. To successfully complete these missions, estimation of air data parameters are vital. Conventional pitot tubes are not suitable for operation in hypersonic flight environments due to extreme heating of the Pitot tube caused by its small radius. Also, the shock and expansion wave created by conventional pitot tubes have a damaging effect on the spacecraft, hence the concept of FADS, in which the air data is inferred from nonintrusive surface pressure measurements (in Figure 12). This innovation allows for the continued operation of instrumentation during high temperature supersonic re-entry, which extends the useful

range of the air data measurement system to hypersonic flow regime. FADS (Flush Air Data System) is also utilized for estimation of the air data parameters on WIRES#013 and WIRES#015, whose flight control system requires air data acquisition with high precision and high reliability.

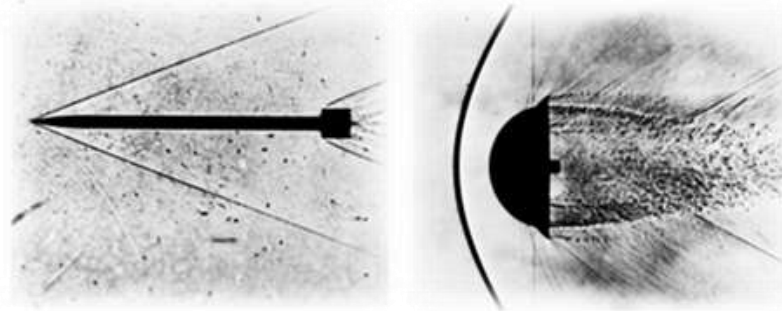


Figure 12 - Shock wave propagation on sharp and blunt object

However, in the extreme thermal environment of re-entry (in Figure 13), pressure ports still have a high risk of failure, making the acquisition of the air data unreliable and adversely affecting flight control. From the 1980s, NASA has been studying the implementation of FADS for hypersonic vehicles such as the X-15 and X-33 (in Figure 14). JAXA had also been studying the implementation of FADS in a hypersonic vehicle called HYFLEX^[5] (Hypersonic FLight EXperiment) shown in Figure 15, but was never practically implemented due to the cancellation of the project. In addition, due to the severe conditions during re-entry, the failure risk of the measuring apparatus was even higher. Therefore, by utilizing a large number of pressures holes and developing FADS with fault tolerance design, the authors aim to create a system that is able to operate in any environment.



Figure 13 – Artistic depiction of WIRES and HYFLEX vehicles during re-entry (©JAXA)

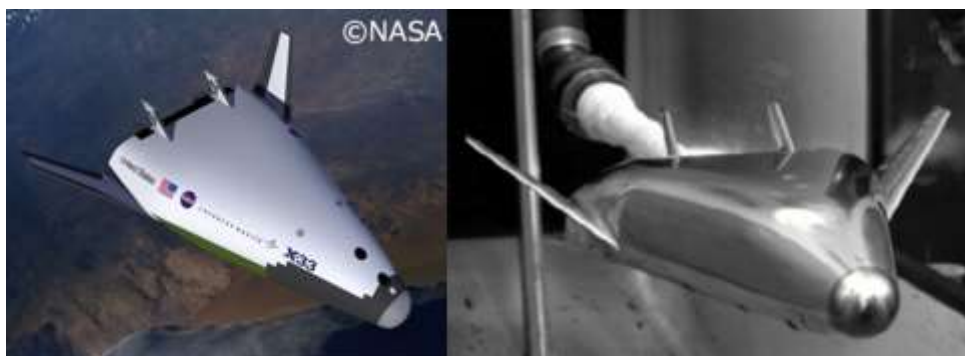


Figure 14 – Conceptual design and wind tunnel test model of X-33 vehicle (©NASA)



Figure 15 – HYFLEX hypersonic flight experiment vehicle (©JAXA)

1.3 Previous Research for Air Data Sensing System

Recently, Todaka et al. proposed a 17 hole FADS (in Figure 16) estimation algorithm based on Tashiro's method^[6] of calculating static pressure and referred to Suenaga's method to calculate the calibration factor for a FADS specimen. In the method of Suenaga^[7] et al., Flow measurement is performed using a conical 7-hole pitot tube. In addition, static pressure measurement is basically acquired from the static pressure hole of the vehicle, from the viewpoint of redundancy it was decided to make it possible to calculate the static pressure from the surface pressure distribution of FADS. Regarding the calculation method of static pressure, authors referred Tashiro's method which obtains static pressure by using a perforated yaw meter. The flowchart for this FADS estimation algorithm is shown in Figure 17 .

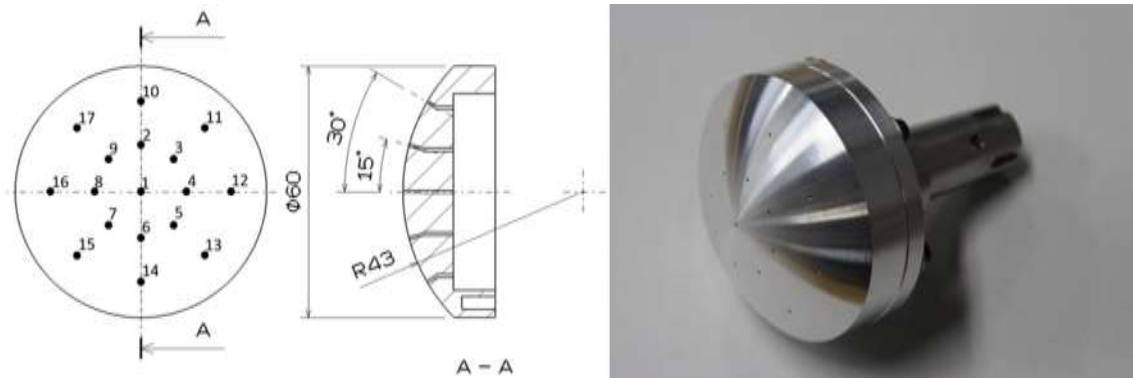


Figure 16 – FADS wind tunnel model of Todaka's method

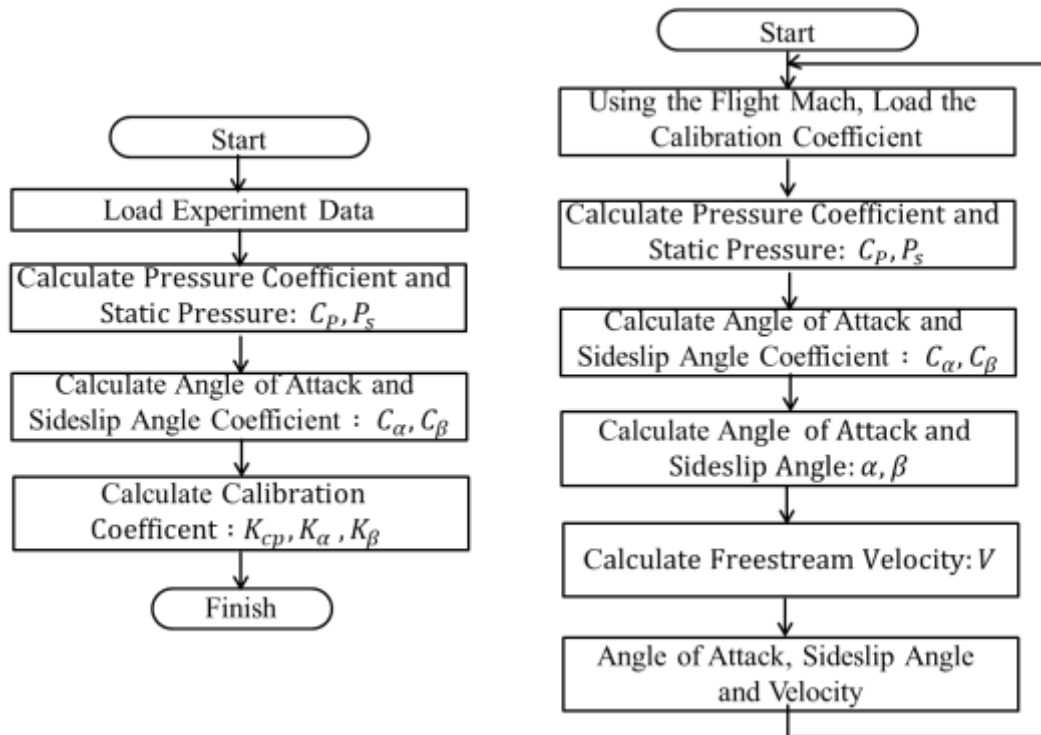


Figure 17 – Flowchart algorithm of FADS proposed by Todaka using Suenaga and Tashiro’s method

1.3.1 Calculation of Calibration Coefficients

1.3.1.1 Calculation of Static Pressure

First, static pressure is calculated by the method proposed by Suenaga et al., from the port pressure of the pressure holes other than port 1 of the conical Pitot tube, and it is corrected by the static pressure coefficient obtained from the wind tunnel experiments (in Figure 18).

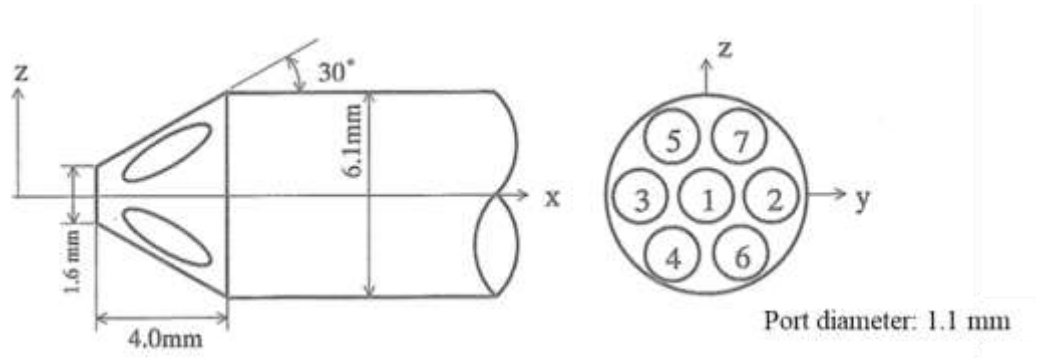


Figure 18 – Conical Pitot tube in Suenaga's method

However, in the case of FADS, since the surface shape is spherical, it is impossible to use the calculation formula of Suenaga's method as it is. Therefore, a method of measuring static pressure from the FADS surface pressure distribution was examined with reference to the method of Tashiro et al. which performed the static pressure independent of the probe shape. In this method, the pressure coefficient of each pressure hole for different angle of incident and angle of attack is calculated. Then, two holes are arbitrarily selected from the pressure holes, and the static pressure is obtained by using the measured pressure and the pressure coefficient of the selected pressure hole. First, the pressure coefficient is needed to be estimated. The pressure coefficient is obtained by taking the dynamic pressure of the wind tunnel in the denominator and the dynamic pressure of each pressure hole of the FADS to the numerator as follows in equation 1.

$$C_{P(\alpha,\beta)} = \frac{P_n - P_{s_wt}}{(\rho_{wt} V_{wt}^2)/2} \quad (1)$$

C_P : Pressure coefficient [-]

P_n : Pressure of nth hole [kPa]

P_{s_wt} : Wind tunnel Static Pressure [kPa]

ρ_{wt} : Wind tunnel air density [kg/m³]

V_{wt} : Wind tunnel velocity [m/s²]

Next, two pressure measurements of m and n pressure holes namely P_m and P_n are arbitrarily selected from the 17 pressure holes of FADS, then the notation for the pressure coefficients is C_{Pm} and C_{Pn} respectively. Then the pressure hole difference is expressed by the following equation 2:

$$\Delta P_{mn} = (P_m - P_n) = (C_{Pm} - C_{Pn})(\rho_{wt} V_{wt}^2)/2 \quad (2)$$

ΔP_{mn} : Pressure difference of m, nth Pressure hole [kPa]

P_m : Pressure of mth hole [kPa] P_n : Pressure of nth hole [kPa]

C_{Pm} : Pressure coefficient of mth hole [-] C_{Pn} : Pressure Coefficient of nth hole [-]

From Expressions 1 and 2, the static pressure can be obtained from the surface pressure distribution of FADS by the following equation 3.

$$P_s = P_m - C_{Pm} \frac{P_m - P_n}{C_{Pm} - C_{Pn}} \quad (3)$$

P_s : Static pressure obtained from surface pressure distribution [kPa]

From equations 1 and 3, if pressure coefficients of each pressure hole are previously obtained by wind tunnel experiment for each angle of attack and sideslip angle, the free flow static pressure can be obtained. In this static pressure calculation method, two pressure holes are arbitrarily selected from the pressure holes of 17 holes to be used for calculation. Therefore, there are 136 combinations for selecting two pressure holes, and since the calculation results of static pressure are the same for any combination of pressure holes, there is an advantage that the static pressure acquisition method is with high redundancy.

1.3.1.2 Calculation for Coefficients of Angle of Attack and sideslip angle

Next, we calculate the coefficients of angle of attack and sideslip angle. According to Suenaga's method, the angle of attack coefficient is determined as the ratio of the pressure difference for the ports in the pitch direction of the perforated pitot tube and the dynamic pressure, and the sideslip angle coefficient is obtained as the ratio of the pressure difference in the yaw direction of the perforated pitot tube and the dynamic pressure (in Figure 19). For the 17 holes FADS, since the number of pressure holes are more, it can be expressed by the following equations 4 and 5.

$$C_{\alpha} = \frac{\left(\frac{P_5 + P_6 + P_7 + P_{13} + P_{14} + P_{15}}{6}\right) - \left(\frac{P_2 + P_3 + P_9 + P_{10} + P_{11} + P_{17}}{6}\right)}{P_i - P_s} \quad (4)$$

$$C_{\beta} = \frac{\left(\frac{P_7 + P_8 + P_9 + P_{15} + P_{16} + P_{17}}{6}\right) - \left(\frac{P_3 + P_4 + P_5 + P_{11} + P_{12} + P_{13}}{6}\right)}{P_i - P_s} \quad (5)$$

C_{α} : Coefficient of angle of attack [-] C_{β} : Coefficient of sideslip angle [-]

P_i : Maximum pressure from the surface pressure distribution [kPa]

$P_1 \sim P_{17}$: Pressure of each Hole [kPa] P_s : Static pressure [kPa]

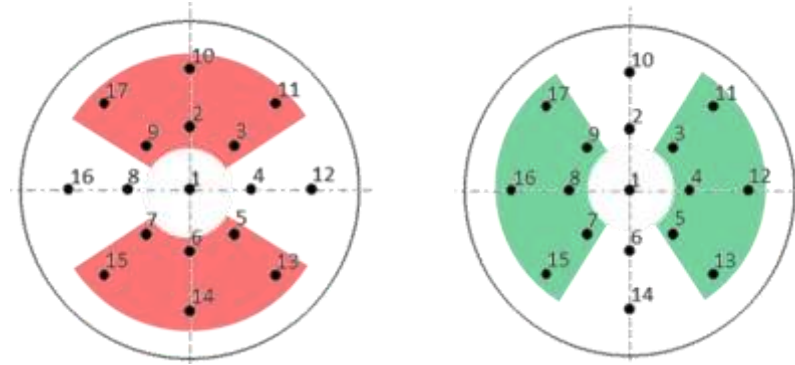


Figure 19 – Pressure holes selection for calculating the coefficients of angle of attack sideslip angle

1.3.1.3 Calculation of Calibration Coefficient

The calibration coefficient is necessary when calculating the angle of attack, sideslip angle, and the pressure coefficients for each pressure hole during the flight. First, we assume that the angle of attack or sideslip angle can be expressed using the 3 degree polynomial equation with the coefficients of angle of attack and the sideslip angle obtained from the previous section as shown in the follow equation 6.

$$A = K_1 + K_2 C_\alpha + K_3 C_\beta + K_4 C_\alpha^2 + K_5 C_\alpha C_\beta + K_6 C_\beta^2 + K_7 C_\alpha^3 + K_8 C_\alpha^2 C_\beta + K_9 C_\alpha C_\beta^2 + K_{10} C_\beta^3 + \text{ignored higher order terms} \quad (6)$$

A : α , β , C_p (one of the value is input) $K_1 \sim K_{10}$: Calibration Coefficients [-]

C_α : Coefficient of Angle of Attack [-] C_β : Coefficient of Sideslip [-]

A varies depending on the calculation target such as angle of attack, sideslip angle, and the pressure coefficient of each pressure hole. From equations 7 and 10 calibration coefficients are estimated for each calculation target.

$$\begin{pmatrix} A_1 \\ A_2 \\ A_3 \\ \vdots \\ A_n \end{pmatrix} = \begin{pmatrix} 1 & C_{\alpha 1} & C_{\beta 1} & \cdots & C_{\beta 1}^3 \\ 1 & C_{\alpha 2} & C_{\beta 2} & \cdots & C_{\beta 2}^3 \\ 1 & C_{\alpha 3} & C_{\beta 3} & \cdots & C_{\beta 3}^3 \\ \vdots & \vdots & \vdots & \vdots & \vdots \\ 1 & C_{\alpha n} & C_{\beta n} & \cdots & C_{\beta n}^3 \end{pmatrix} \begin{pmatrix} K_1 \\ K_2 \\ K_3 \\ \vdots \\ K_{10} \end{pmatrix} \quad (7)$$

Then the equation can be reduced as the following equation 8.

$$[A] = [C][K] \quad (8)$$

Here n is number of samples. In the above equation, for the target calibration coefficient, in column matrix [A] and the matrix [C] are known from the wind tunnel test data, the column vector [K] of the calibration coefficients can be calculated.

1.3.2 Calculation of Physical Quantities

1.3.2.1 Acquisition of Physical Mach Number

From the FADS calibration, calibration coefficients for static pressure, angle of attack, and sideslip angle at each Mach number are obtained. Therefore, during the flight test, it is necessary to first detect the Mach region and to read the calibration coefficient accordingly. However, since the estimation method of the Mach number has not been determined at this time, the Mach number will be updated after the estimation.

1.3.2.2 Calculation of Static Pressure

The static pressure calculation during the implementation (flight test) is the same as mentioned in the calibration method. During the flight test, calibration coefficients $K_{cp1} \sim K_{cp10}$ relating to pressure coefficients are obtained for the

respective Mach number of the flow, from which the pressure coefficient C_p of each pressure hole is obtained as follows in equation 9.

$$C_p = K_{cp1} + K_{cp2}C_\alpha + K_{cp3}C_\beta + K_{cp4}C_\alpha^2 + K_{cp5}C_\alpha C_\beta + K_{cp6}C_\beta^2 + K_{cp7}C_\alpha^3 + K_{cp8}C_\alpha^2 C_\beta + K_{cp9}C_\alpha C_\beta^2 + K_{cp10}C_\beta^3 + \text{ignored higher order terms} \quad (9)$$

C_p : Pressure coefficient [-] $K_{cp1} \sim K_{cp10}$: Calibration coefficient (for C_p) [-]

During the flight test, C_α and C_β are calculated for the previous pressure distribution measured. The new pressure coefficients for each pressure hole are calculated by a three degree polynomial equation which has the previous pressure coefficient and calibration coefficient. Now, 2 holes are selected arbitrarily from the 17 hole FADS and static pressure is calculated from equation 3. Here, as mentioned earlier, there are 136 combinations when selecting 2 holes from 17 holes. The 136 combinations of static pressure are calculated and the average value gives the estimated static pressure.

1.3.2.3 Calculation of Freestream Angle of Attack and Sideslip Angle

The coefficients of angle of attack and sideslip angle are calculated in the same way as mentioned in section 1.3.1.2 and applied to the following equations 10 and 11 to estimate the free stream angle of attack and sideslip angle.

$$\alpha = K_{\alpha1} + K_{\alpha2}C_\alpha + K_{\alpha3}C_\beta + K_{\alpha4}C_\alpha^2 + K_{\alpha5}C_\alpha C_\beta + K_{\alpha6}C_\beta^2 + K_{\alpha7}C_\alpha^3 + K_{\alpha8}C_\alpha^2 C_\beta + K_{\alpha9}C_\alpha C_\beta^2 + K_{\alpha10}C_\beta^3 + \text{ignored higher order terms} \quad (10)$$

$$\beta = K_{\beta1} + K_{\beta2}C_\alpha + K_{\beta3}C_\beta + K_{\beta4}C_\alpha^2 + K_{\beta5}C_\alpha C_\beta + K_{\beta6}C_\beta^2 + K_{\beta7}C_\alpha^3 \quad (11)$$

$$+K_{\beta 8}C_{\alpha}^2C_{\beta} + K_{\beta 9}C_{\alpha}C_{\beta}^2 + K_{\beta 10}C_{\beta}^3 + \text{ignored higher order terms}$$

α : Angle of attack [rad] $K_{\alpha 1} \sim K_{\alpha 10}$: Calibration coefficient (for C_{α}) [-]

β : Sideslip angle [rad] $K_{\beta 1} \sim K_{\beta 10}$: Calibration coefficient (for C_{β}) [-]

1.3.2.4 Calculation of Airspeed

In the Suenaga's et al. method, the pressure coefficient and static pressure coefficient are obtained beforehand from wind tunnel experiment, and during the flight test, the total pressure and the static pressure are calculated using the same calculation model. Then, the total pressure and static pressure are substituted into the formula of dynamic pressure to obtain the velocity of the flow. However, since the value of the pressure hole of 1 is used for obtaining the total pressure and the static pressure, if the pressure hole fails, it is impossible to calculate the static pressure and the total pressure. Therefore, with reference to Tashiro's method, it is necessary to obtain the airspeed by using the pressure coefficient as shown in equation 12.

$$V = \sqrt{\frac{2(P_m - P_n)}{\rho(C_{Pm} - C_{Pn})}} \quad (12)$$

V : Airspeed [m/s^2]

ρ : Density [kg/m^3]

P_m : Pressure of m^{th} hole [kPa]

P_n : Pressure of n^{th} hole [kPa]

C_{Pm} : Pressure coefficient of m^{th} hole [-]

C_{Pn} : Pressure coefficient of n^{th} hole [-]

Similar to static pressure calculation, there are 136 combinations when selecting 2 holes out of 17 holes of the FADS. Airspeed is calculated for all combinations and the average value is the estimated airspeed.

1.4 Drawbacks of Research

FADS system will be utilized for estimation of the air data parameters on WIRES#013 and WIRES#015, whose flight control system requires air data acquisition with high precision and high reliability. If one of the pressure sensors (out of 17 pressure holes) fails during flight, the faulty sensor has to be detected and isolated from the algorithm when estimating the air data parameters. If the method proposed in the previous section is employed, there are the following drawbacks when incorporating the fault detection. One such drawback is, when estimating the angle of attack and sideslip angle, average value of the pressure values obtained from each pressure hole are used. Since the average value is used, it is difficult to detect the fault location of a particular sensor. Also, since the whole algorithm is based on black box modelling, it is impossible to confirm the consistency of the calculation process. Also, the proposed FADS system will be employed for future WIRES vehicle where the flights are in the supersonic region or higher and estimation of the Mach number is necessary. Therefore considering the above limitations, it is considered difficult to develop algorithms based on perfect white box modelling, but NASA has been developing FADS algorithm for their X-33 experimental vehicle based on grey box modelling where the Mach number can also be estimated. Therefore, a new method is proposed in this research, with reference to NASA's X-33 method^[8, 9, 10, 11] and it will be applied to the WIRES vehicle. For this research, the wind tunnel test model of FADS has been developed and wind tunnel experiment has been performed. This data will be utilized for the calibration of the FADS system.

CHAPTER 2. WIND TUNNEL EXPERIMENTS

2.1 Objective of the Experiments

Pressure distribution measurements are measured using wind tunnel tests every year and surface pressure distribution data which will be used for the calibration of the FADS test model under various conditions (angle of attack, Sideslip angle, Mach number) is measured. In this section, the FADS test model and the high-speed wind tunnel facility of the JAXA Sagamihara campus used and the test conditions which are carried out are described.

2.1.1 *FADS Wind Tunnel Test Model*

As mentioned in the previous chapter, the FADS system will be employed on the winged rockets WIRES#013, WIRES#015. For this reason, the FADS wind tunnel test model is designed from the aerodynamic shape of the nose cone of the WIRES vehicle. In the 2013, wind tunnel experiments are conducted for test model mentioned in Figure 16. As a result of the experiment, it was found that the expansion wave generated along the model shape in the subsonic range (Mach 0.5, 0.8, 1.0) reached the last layer of pressure holes position and affected the pressure data acquired. This problem was solved by extending the shape of the model to the downstream side. The new wind tunnel model was reproduced. The external view and the drawing of the FADS test model are shown in Figure 20 and Figure 21. The diameter of the FADS specimen is 110 mm and the radius of curvature of the tip is 43 mm. The arrangement of the pressure holes is the same as the model of last year. As shown in Figure 22, the FADS specimen has one hole at the centre and two layers of holes radially from the centre with a total of 17 holes. The specimen consists of three parts, a tip part, an

intermediate part, and an interface part. The tip part and the intermediate part were manufactured with A2017, but since the interface part is a part connected to the Sting of the wind tunnel, it was made with SUS 303 in order to avoid surface wear. Experimental Schlieren images are shown in Figure 23 for Mach number. Red colour in colour schlieren image is compression wave (including shock wave in supersonic flow) and blue colour visualizes expansion waves. Figure 24 shows the comparison results for the two wind tunnel test models.

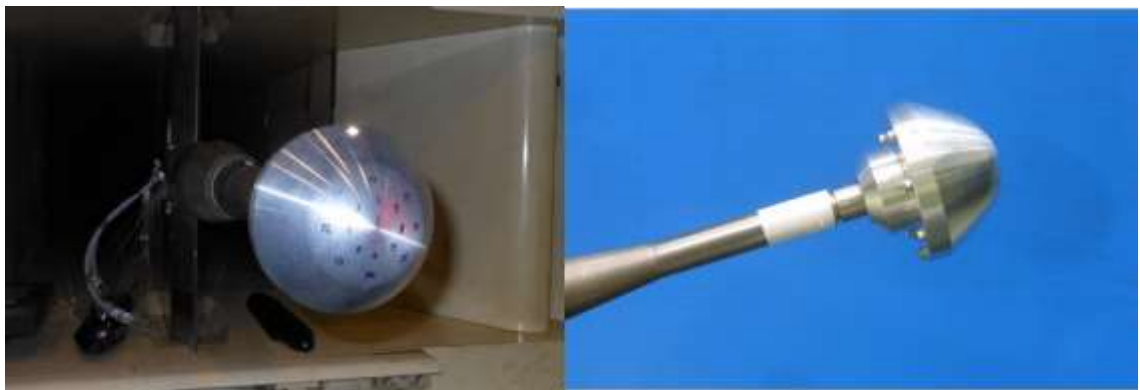


Figure 20 – View of FADS wind tunnel test model (front and side view)

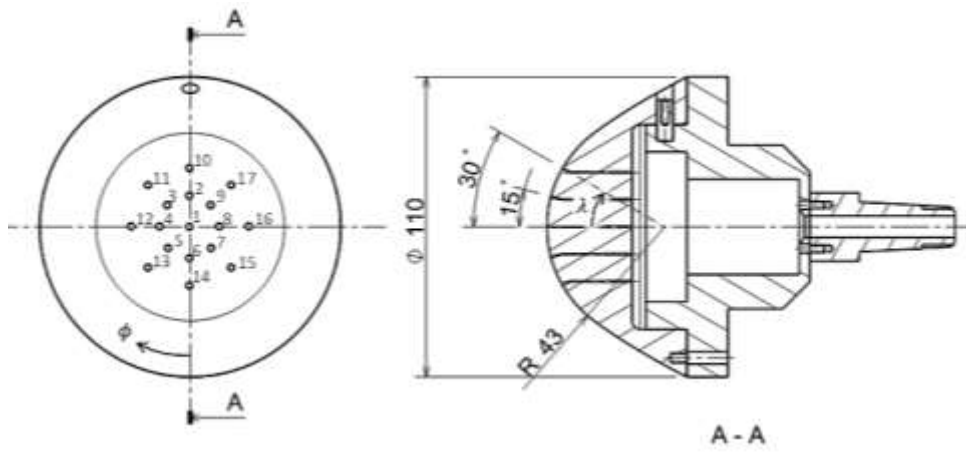


Figure 21 – Drawing of FADS wind tunnel test model



Figure 22 - Position of pressure port

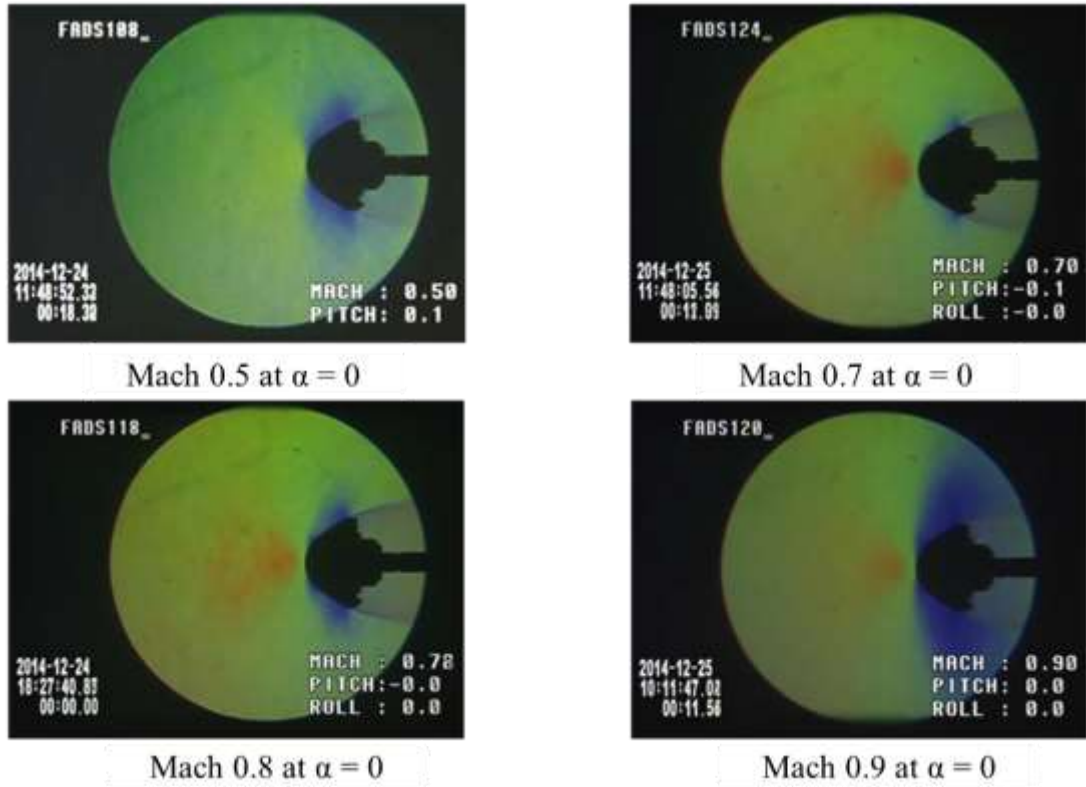


Figure 23 – Schlieren images taken during the wind tunnel experiments

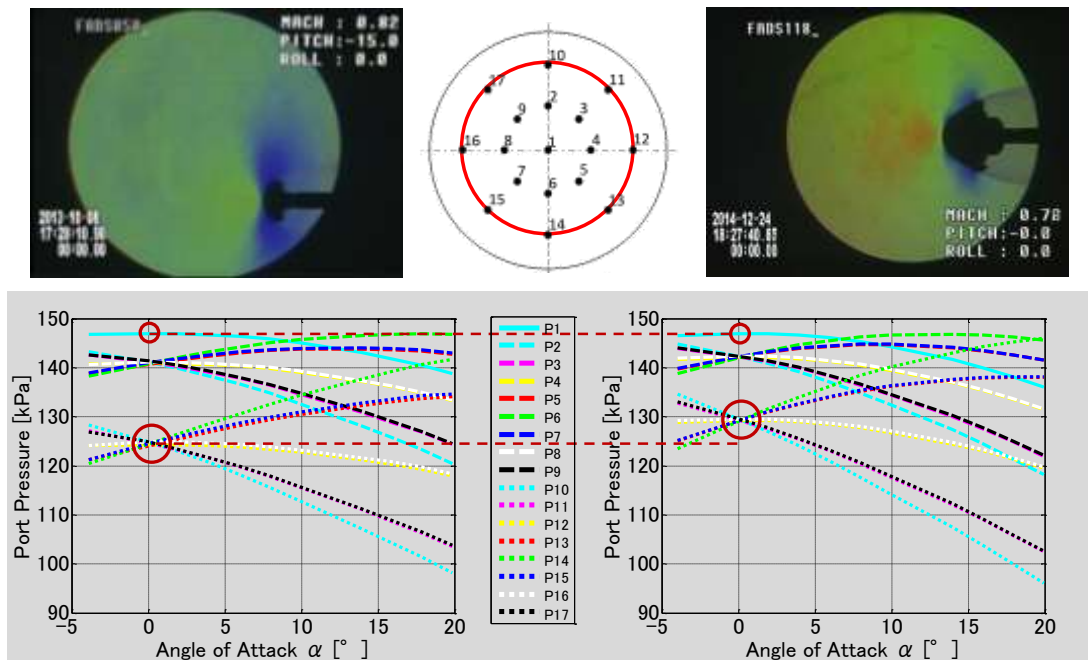


Figure 24 – Schlieren images and pressure distribution comparison between the two wind tunnel experiments

2.1.2 *Wind Tunnel Test Facility*

The measurement of the surface pressure distribution used for the calibration of the FADS system was carried out using the subsonic wind tunnel and the supersonic wind tunnel (in Figure 25) in the high speed air flow comprehensive experimental facility of the JAXA/ISAS Sagamihara campus. Both wind tunnels are intermittent blow-down type, air is stored in the gas storage tank by the compressor, and air flow is generated by releasing the outlet valve of the gas storage tank. Table 3 shows the specifications of wind tunnel facility. This facility is two stories, with main wind tunnel facilities (in Figure 26) on the first floor and measurement rooms on the second floor. The sting used to support the specimen in the wind tunnel facility has two kinds, straight sting and vent sting (in Figure 27). In addition, the angle deflection device of the wind tunnel test facility is controlled by pitch angle and roll angle, and the combination of these two angles is used to obtain the target angle of attack and sideslip angle.



Figure 25 – Subsonic (left) and supersonic (right) wind tunnel test facility of JAXA/ISAS

Table 3 – Specifications of the wind tunnel facility

Wind tunnel	Subsonic	Supersonic
Mach range	0.3 ~ 1.3	1.5 ~ 4.0
Type	Intermittently downwash	
Test cross section	600 mm × 600 mm	
Measurement time	More than 30 sec	

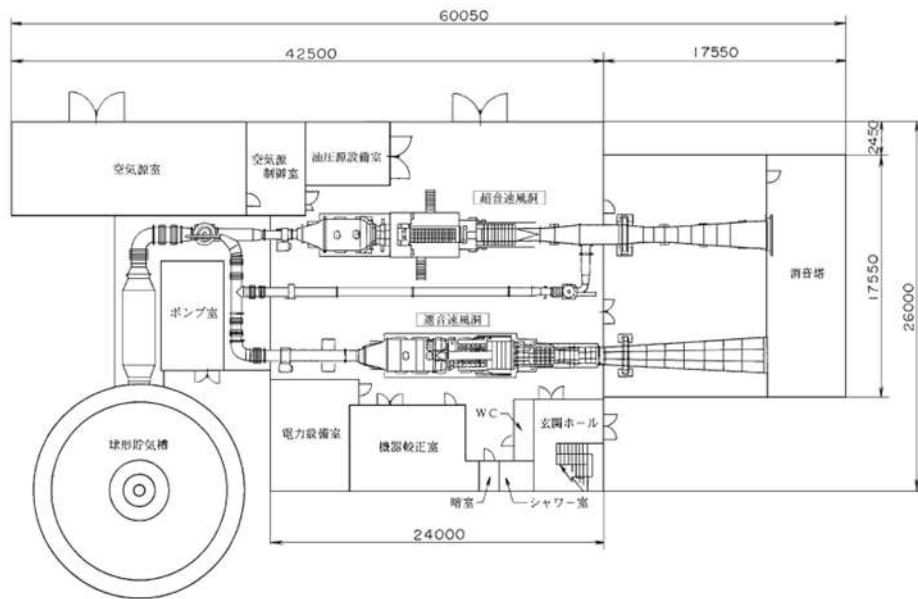


Figure 26 – Schematics of the wind tunnel facility



Figure 27 – Straight sting (left) and vent sting (right)

2.2 Wind Tunnel Test Conditions

The specimen is tested according to the test conditions in Table 4. The experimental data of the FADS from the wind tunnel tests is used for the calibration algorithm discussed in next chapter.

Table 4 – Test conditions carried out

Mach number	0.3, 0.5, 0.7, 0.8, 0.9, 1.0, 2.0, 3.0
Angle of attack	$-4^{\circ} \sim 20^{\circ}$ (every 2°)
Sideslip angle	$0^{\circ} \sim 4^{\circ}$ (every 2°)

The measurement conditions for the surface pressure distribution in the wind tunnel test are as follows. The sampling frequency is set to 1 msec. In the wind tunnel test, since the measurement is performed under multiple conditions at a time for a certain Mach number condition, considering the settling time after every angular deflection, the measurement time is set to 3 seconds. There are cases in which some wind tunnel tests could not be carried out due to failure of the angle deflection device of the wind tunnel facility. The test conditions that have been carried out for each fiscal year including the conditions that cannot be implemented are shown in Table 5 below. The various background colors in Table 5 are, orange for successfully tested and blue for cases where roll and pitch angles are given as inputs for the desired angle of attack and sideslip angle and the angle deflection device was not able to achieve the desired attitude. So phase shift in roll direction of 45 [deg.] was performed for the data measurement as shown in Figure 28. In addition, the “X” mark indicates the case where the tests could not be performed even if the phase of the specimen was shifted, and the case where there is a blank are not yet carried out.

Table 5 – Detailed wind tunnel test conditions

Mach	α [°]		β [°]												
			-4	-2	0	2	4	6	8	10	12	14	16	18	20
0.3	0		□	□	△	△	△	△	△	△	△	△	△	△	△
	2		□	□	□	□	□	□	□	□	□	□	□	□	□
	4		□	□	□	□	□	□	□	□	□	□	□	□	□
0.5	0		○	○	○	○	○	○	○	○	○	○	○	○	○
	2		○	○	○	○	○	○	○	○	○	○	○	○	○
	4		○	○	○	○	○	○	○	○	○	○	○	○	○
0.7	0		◇	◇	◇	◇	◇	◇	◇	◇	◇	◇	◇	◇	◇
	2		◇	◇	◇	◇	◇	◇	◇	◇	◇	◇	◇	◇	◇
	4		◇	◇	◇	◇	◇	◇	◇	◇	◇	◇	◇	◇	◇
0.8	0		◇	◇	◇	◇	◇	◇	◇	◇	◇	◇	◇	◇	◇
	2		◇	◇	◇	◇	◇	◇	◇	◇	◇	◇	◇	◇	◇
	4		◇	◇	◇	◇	◇	◇	◇	◇	◇	◇	◇	◇	◇
0.9	0		△	△	△	△	△	△	△	△	△	△	△	△	△
	2		△	△	△	△	△	△	△	△	△	△	△	△	△
	4		△	△	△	△	△	△	△	△	△	△	△	△	△
1.0	0		△	△	△	△	△	△	△	△	△	△	△	△	△
	2		△	△	△	△	△	△	△	△	△	△	△	△	△
	4		△	△	△	△	△	△	△	△	△	△	△	△	△
2.0	0		◇	◇	◇	◇	◇	◇	◇	◇	◇	◇	◇	◇	◇
3.0	0		◇	◇	◇	◇	◇	◇	◇	◇	◇	◇	◇	◇	◇

○ : 2014, ◇ : 2015, △ : 2016, □ : 2017

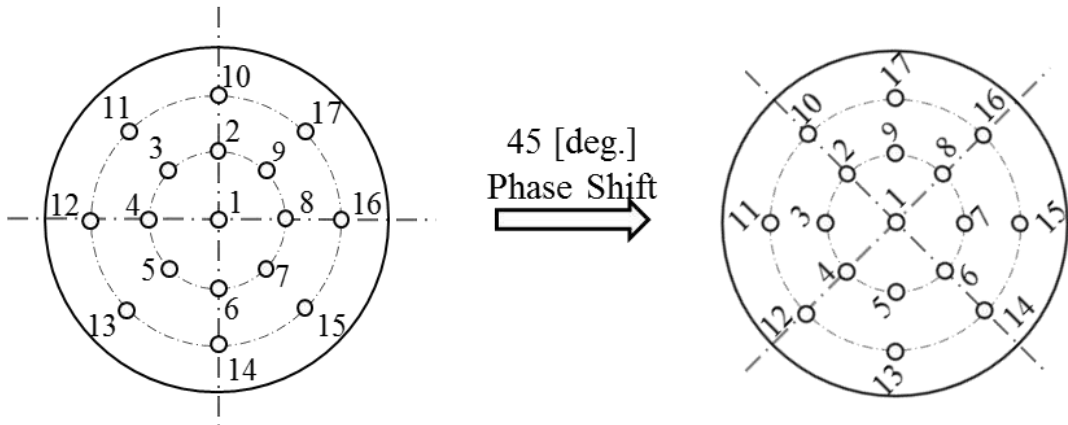


Figure 28 – Phase shift of roll angle 45 [deg.]

*The phase shift method is not the appropriate way for calibration as the FADS hole sizing will not be taken into account. So for all future tests, phase shift method will not be employed.

CHAPTER 3. AIR DATA SENSING ALGORITHM

The design concept of the flush air data sensing system (FADS) was presented by the American National Aeronautics and Space Administration in the 1960s in order to meet the control requirements of the space shuttle. FADS has some significant advantages over traditional sensors, including the higher measurement accuracy and lighter equipment weight. Also, the overall system is installed inside the body such that the vehicle configuration can adapt to the complicated flight environment with consideration of the large angle of attack and high flight dynamic pressure. As a result, FADS can be suitably used in unconventional vehicles such as hypersonic vehicles and Mars entry vehicles. The flush air data sensing model proposed by NASA for X-33 vehicle is explained in this chapter^[13, 14].

3.1 Flush Air Data Sensing Pressure and Geometric Model

The fundamental concept of the FADS system is that air data parameters can be estimated from flush surface pressure measurements. To perform this estimation, the air data states must be related to the surface pressures by an aerodynamic model that captures the salient features of the flow, and is valid over a large Mach number range. To be useful, the model must be simple enough to be inverted in real-time so that the air data parameters can be extracted. To solve the problem of describing a complex flow scenario with a simple model, the FADS aerodynamic model was derived as a splice of the closed form potential flow solution for a blunt body, applicable at low subsonic speeds in equation 13; and the modified Newtonian flow model in equation 14, applicable at hypersonic speeds. Both potential flow and

modified Newtonian flow describe the measured pressure coefficient in terms of the local surface incident angle^[12, 15, 16].

$$C_p(\theta) = \frac{p(\theta) - p_\infty}{q_\infty} = 1 - \frac{9}{4} \sin^2(\theta) = -\frac{5}{4} + \frac{9}{4} \cos^2(\theta) \quad (13)$$

$$C_p(\theta) = \frac{p(\theta) - p_\infty}{q_\infty} \cos^2(\theta) = C_p \cos^2(\theta) \quad (14)$$

Where C_p is the pressure coefficient at a point on the fore body and θ is the incident angle between the surface normal at the pressure port and the local velocity vector as shown in Figure 29. The incident angle is geometrically related to the effective (local) angle of attack α_e and effective (local) sideslip angle β_e . In equation 15, ϕ and λ are the local surface coordinates referred to as the clock and cone angles, respectively. The clock angle is measured clockwise around the longitudinal axis looking aft starting from the bottom. Cone angle is the total angle the normal to the surface makes with respect to the longitudinal axis of the fore body. Figure 29 shows the clock and cone angle definitions.

$$\begin{aligned} \cos(\theta_i) &= \frac{\vec{R} \cdot \vec{V}}{\|\vec{R}\| \|\vec{V}\|} \\ &= \cos(\alpha_e) \cos(\beta_e) \cos(\lambda_i) \\ &\quad + \sin(\beta_e) \sin(\phi_i) \sin(\lambda_i) \\ &\quad + \sin(\alpha_e) \cos(\beta_e) \cos(\phi_i) \sin(\lambda_i) \end{aligned} \quad (15)$$

$$\cos\theta_i = \cos\beta_e(a_i + b_i \tan\beta_e) \quad 15a)$$

$$a_i = \cos\alpha_e \cos\lambda_i + \sin\alpha_e \cos\phi_i \sin\lambda_i, \quad b_i = \sin\phi_i \sin\lambda_i$$

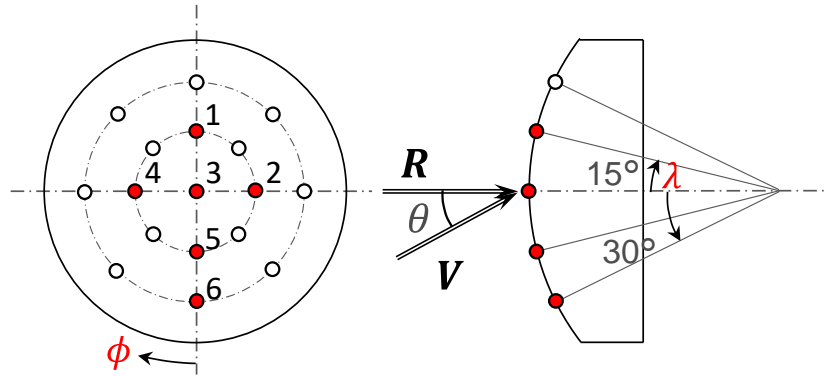


Figure 29 – Location of the pressure ports

Table 6 – Pressure port position ϕ_i, λ_i

Port No.	ϕ_i [deg.]	λ_i [deg.]
1	180	15
2	270	15
3	0	0
4	90	15
5	0	15
6	0	30

Where i is the pressure port index.

The effective angles of attack and sideslip, α_e and β_e are the flow direction angles as locally sensed on the blunt fore body. These angles have been deflected from the free-stream flow direction by expansion around the fore body and by up wash and side wash induced by the rest of the vehicle. The true free-stream flow incident angles are related to the effective angles by a set of calibrations of the forms mentioned in equation 16 and 17.

$$\delta\alpha [M_\infty, \alpha_e] = \alpha_e - \alpha_{ref} \quad (16)$$

$$\delta\beta [M_\infty, \beta_e] = \beta_e - \beta_{ref} \quad (17)$$

The calibrations must be empirically determined using a reference air data set obtained from the wind tunnel. equations 13 and 14 can be spliced together to give a flow model that is applicable to a large Mach number range by the parameterization as shown in equation 18.

$$C_p \theta = X M_\infty, \alpha_e, \beta_e + Y M_\infty, \alpha_e, \beta_e \cos^2 \theta \quad (18)$$

where the coefficients X and Y are a function of Mach number and the effective flow angles. At 0° incident angle, equation 18 must satisfy subsonic flow conditions shown in equation 19:

$$C_p \theta = X + Y = \frac{P_i - P_\infty}{q_\infty} = \frac{q_c}{q_\infty} \quad (19)$$

and supersonic flow conditions shown in equation 20:

$$C_p \theta = X + Y = \frac{P_{t2} - P_\infty}{q_\infty} = \frac{q_c}{q_\infty} \quad (20)$$

By setting as shown in equations 21 and 22

$$X M_\infty, \alpha_e, \beta_e = \frac{q_c}{q_\infty} \varepsilon M_\infty, \alpha_e, \beta_e \quad (21)$$

And

$$Y M_{\infty, \alpha_e, \beta_e} = \frac{q_c}{q_{\infty}} [1 - \varepsilon M_{\infty, \alpha_e, \beta_e}] \quad (22)$$

The constraints of equations 19 and 20 are satisfied for all Mach numbers. To blend the two solutions over a large range of Mach numbers, a calibration parameter ε was allowed for. This parameter must be empirically calibrated to allow for the effects of flow compression, body shape, and other systematic effects such as shock wave compression or Prandtl-Meyer expansion on the fore body^[17, 18]. The general pressure model will be expressed in equation 23:

$$\begin{aligned} C_p \theta &= X + Y \cos^2 \theta = \frac{q_c}{q_{\infty}} \varepsilon + \frac{q_c}{q_{\infty}} (1 - \varepsilon) \cos^2 \theta \\ &= \frac{q_c}{q_{\infty}} \cos^2 \theta + \varepsilon \sin^2 \theta = \frac{P_i - P_{\infty}}{q_{\infty}} \end{aligned} \quad (23)$$

Equation 23 can be further simplified as shown in equation 24:

$$P_i = q_c \cos^2 \theta_i + \varepsilon \sin^2 \theta_i + P_{\infty} \quad (24)$$

In equations 19 to 24, q_{∞} is the freestream dynamic pressure and q_c is the impact pressure.

3.2 Flush Air Data Sensing Estimating Algorithm

Equation 24 states that the local surface pressure at any point on a spherical (blunt) fore body is a function of the free-stream flight conditions, the angle between the effective flow vector and the surface normal, and a calibration parameter ε . Because flow incident angles α_e and β_e are imbedded in θ and ε , equation 24 is inherently nonlinear. Usually five or more pressure measurements are used to solve

for the minimum air data state $q_\infty, P_\infty, \alpha_e$ and β_e although the air data can be calculated with as few as four. The minimum air data state is sufficient to calculate all other important air data parameters (pressure altitude, Mach number, equivalent airspeed) except true airspeed, which requires a measurement or estimate of the free-stream temperature in order to calculate the speed of sound. The estimation algorithm consists of two different flows, one used for the calibration using wind tunnel test data and other for onboard estimation (in Figure 30). Most the equations used in both the algorithms are same. Therefore, in the following subsections, the air data parameters estimation equations are described for both algorithms^[19].

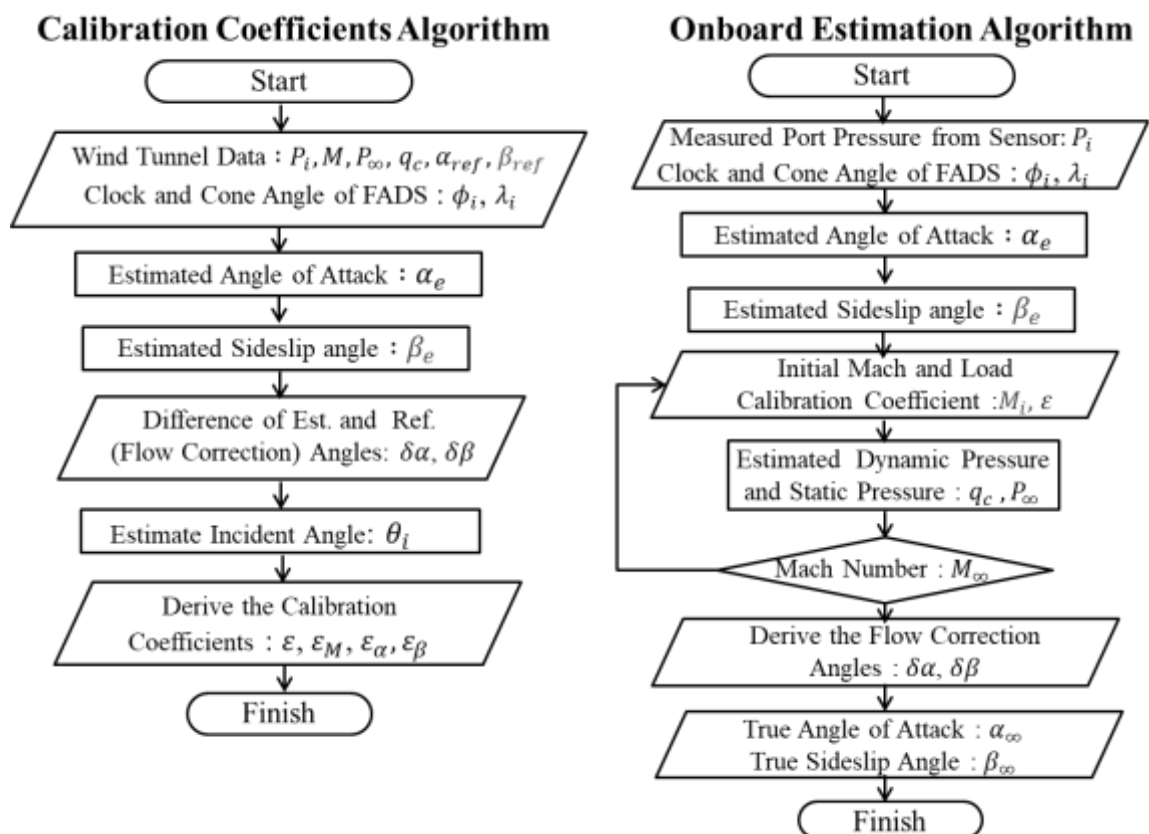


Figure 30 – Calibration coefficients and estimation algorithms of FADS using NASA method

3.2.1 The Triples Equation

By taking strategic combinations of three surface sensor measurements (“triples”), $q_\infty, P_\infty, \varepsilon$, and are eliminated from equation 24. The resulting equation 25 is shown as follows:

$$\begin{aligned}
 \frac{P_i - P_j}{P_j - P_k} &= \frac{\left[q_c \cos^2 \theta_i + \varepsilon \sin^2 \theta_i + P_\infty \right] - \left[q_c \cos^2 \theta_j + \varepsilon \sin^2 \theta_j + P_\infty \right]}{\left[q_c \cos^2 \theta_j + \varepsilon \sin^2 \theta_j + P_\infty \right] - \left[q_c \cos^2 \theta_k + \varepsilon \sin^2 \theta_k + P_\infty \right]} \\
 &= \frac{\left[1 - \varepsilon \cos^2 \theta_i + \varepsilon \right] - \left[1 - \varepsilon \cos^2 \theta_j + \varepsilon \right]}{\left[1 - \varepsilon \cos^2 \theta_j + \varepsilon \right] - \left[1 - \varepsilon \cos^2 \theta_k + \varepsilon \right]} \\
 &= \frac{\cos^2 \theta_i - \cos^2 \theta_j}{\cos^2 \theta_j - \cos^2 \theta_k}
 \end{aligned} \tag{25}$$

Rearranging equation 25 yields equations 26 and 27

$$\Gamma_{ik} \cos^2 \theta_j + \Gamma_{ji} \cos^2 \theta_k + \Gamma_{kj} \cos^2 \theta_i = 0 \tag{26}$$

where

$$\begin{aligned}
 \Gamma_{ik} &= P_i - P_k \\
 \Gamma_{ji} &= P_j - P_i \\
 \Gamma_{kj} &= P_k - P_j
 \end{aligned} \tag{27}$$

and P_i, P_j and P_k are the pressures used in the triple equation. Although equation 25 is still nonlinear, ε has been removed, thus decoupling the local flow angles from the calibration parameter.

3.2.2 Angle of Attack Triples Estimator

The effective angle of attack α_e can be further decoupled from sideslip angle β_e by using only pressures aligned along a vertical meridian (where $\phi = 0^\circ$ or 180° shown in Figure 31 and Table 7). In this geometry arrangement, terms related to sideslip angle β_e are eliminated from equation 26. The result is a quadratic expression in $\tan(\alpha_e)$ of the form shown in equation 30 .

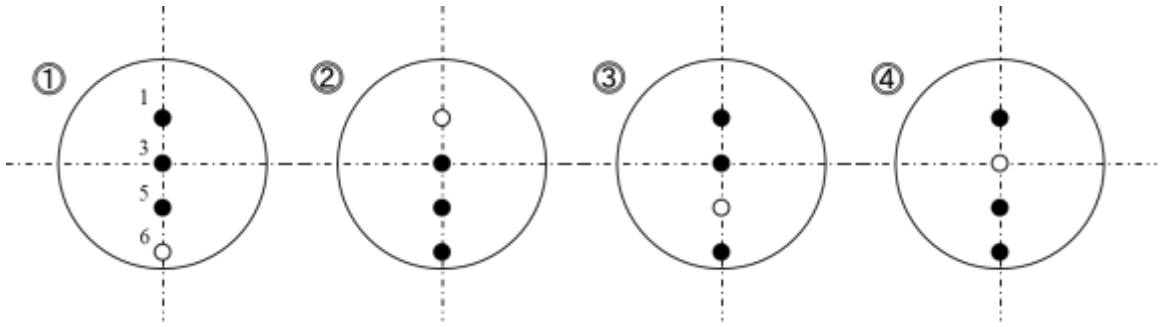


Figure 31 – Pressure port combination for angle of attack estimation

Table 7 – Pressure port combination and geometric angle of each port for angle of attack estimation

Combination No.	Port No.	ϕ_i [deg.]	λ_i [deg.]	Port No.	ϕ_i [deg.]	λ_i [deg.]	Port No.	ϕ_i [deg.]	λ_i [deg.]
1	1	180	15	3	0	0	5	0	15
2	3	0	0	5	0	15	6	0	30
3	1	180	15	3	0	0	6	0	30
4	1	180	15	5	0	15	6	0	30

By rearranging pressure equation 26 with equation 15a :

$$\Gamma_{ik} (a_j + b_j \tan \beta_e)^2 + \Gamma_{ji} (a_k + b_k \tan \beta_e)^2 + \Gamma_{kj} (a_i + b_i \tan \beta_e)^2 = 0 \quad (28)$$

The equation 28 is simplified because of the selection of ports on the vertical meridian

$$\Gamma_{ik} a_j^2 + \Gamma_{ji} a_k^2 + \Gamma_{kj} a_i^2 = 0 \quad (29)$$

Further, the local angle of attack is estimated by rearranging

$$A(\tan^2 \alpha_e - 1) + 2B \tan \alpha_e = 0 \quad (30)$$

$$\alpha_e = \tan^{-1} \left(\frac{-B \pm \sqrt{B^2 - A^2}}{A} \right)$$

where $A = (P_i - P_j) \sin^2 \lambda_k + (P_j - P_k) \sin^2 \lambda_i + (P_k - P_i) \sin^2 \lambda_j$

$$B = (P_i - P_j) \cos \phi_k \cos \lambda_k \sin \lambda_k + (P_j - P_k) \cos \phi_i \cos \lambda_i \sin \lambda_i \\ + (P_k - P_i) \cos \phi_j \cos \lambda_j \sin \lambda_j$$

The output angle of attack estimate is determined as the mean of the values computed using the four individual triples as shown in equation 31. This averaging procedure provides a measure of noise rejection for the estimator. Clearly, if one of the ports along the vertical meridian is deemed unusable and is weighted out of the algorithm, then only one valid triple remains for computing the angle of attack.

$$\alpha_e = \frac{1}{n} \sum_{x=1}^n \alpha_{e_{(i,j,k)_x}} \left[P_{\{i,j,k\}}, \lambda_{\{i,j,k\}}, \phi_{\{i,j,k\}} \right] \Big|_{n=4} \quad (31)$$

3.2.3 Sideslip Angle Triples Estimator

Once the local angle of attack has been estimated, then the sideslip angle may be evaluated using any combination of the available ports (in Figure 32), other than the obvious set in which all three ports lie on the vertical meridian.

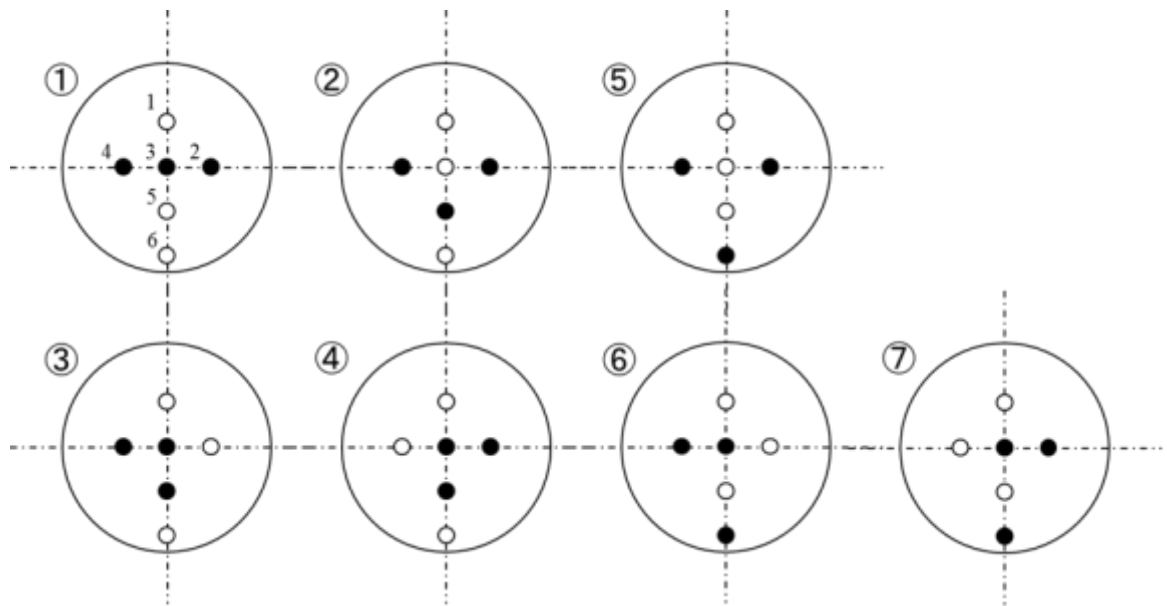


Figure 32 – Pressure port combination for sideslip angle estimation

Table 8 – Pressure port combination and geometric angle of each port for sideslip angle estimation

Combination No.	Port No.	ϕ_i [deg.]	λ_i [deg.]	Port No.	ϕ_j [deg.]	λ_j [deg.]	Port No.	ϕ_k [deg.]	λ_k [deg.]
1	3	0	0	4	90	15	2	270	15
2	5	0	15	4	90	15	2	270	15
3	3	0	0	4	90	15	5	0	15
4	3	0	0	2	270	15	5	0	15
5	6	0	30	4	90	15	2	270	15
6	3	0	0	4	90	15	6	0	30
7	3	0	0	2	270	15	6	0	30

Using equation 28,

$$\Gamma_{ik} (a_j + b_j \tan \beta_e)^2 + \Gamma_{ji} (a_k + b_k \tan \beta_e)^2 + \Gamma_{kj} (a_i + b_i \tan \beta_e)^2 = 0$$

The result is a quadratic expression in $\tan(\beta_e)$ of the form shown in equation 32 .

$$A' \tan^2 \beta_e + 2B' \tan \beta_e + C' = 0$$

$$\beta_e = \tan^{-1} \left(\frac{-B' \pm \sqrt{B'^2 - A'C'}}{A'} \right) \quad (32)$$

where $A' = (P_i - P_k) \sin \phi_j \sin \lambda_j^2 + P_j - P_i \sin \phi_k \sin \lambda_k^2 + (P_k - P_j) \sin \phi_i \sin \lambda_i^2$

$$B' = \left\{ \begin{array}{l} (P_i - P_k) (\cos \alpha_e \cos \lambda_j + \sin \alpha_e \cos \phi_j \sin \lambda_j) (\sin \phi_j \sin \lambda_j) \\ + (P_j - P_i) (\cos \alpha_e \cos \lambda_k + \sin \alpha_e \cos \phi_k \sin \lambda_k) (\sin \phi_k \sin \lambda_k) \\ + (P_k - P_j) (\cos \alpha_e \cos \lambda_i + \sin \alpha_e \cos \phi_i \sin \lambda_i) (\sin \phi_i \sin \lambda_i) \end{array} \right\}$$

$$C' = \left\{ \begin{array}{l} (P_i - P_k) (\cos \alpha_e \cos \lambda_j + \sin \alpha_e \cos \phi_j \sin \lambda_j)^2 \\ + (P_j - P_i) (\cos \alpha_e \cos \lambda_k + \sin \alpha_e \cos \phi_k \sin \lambda_k)^2 \\ + (P_k - P_j) (\cos \alpha_e \cos \lambda_i + \sin \alpha_e \cos \phi_i \sin \lambda_i)^2 \end{array} \right\}$$

Equation 32 has two solutions. However, unlike the solution for angle of attack these solutions cannot be reduced to a single obvious choice for the sideslip angle roots. Determining which root is correct depends on the port arrangement used to determine the sideslip angle. Since only four sideslip angle ports are required for a redundant measurement system, the number of possible sideslip angle triples to be considered is reduced to a more manageable number by removing the upper 20° port (port number 1) on the vertical meridian.

As with the angle of attack algorithm, the output sideslip angle estimate are determined as the mean of the values computed using the seven individual triples as shown in equation 33. Clearly, if of the ports along the vertical meridian is deemed unusable and is weighted out of the algorithm, and then only one valid triple remains for computing the sideslip angle.

$$\beta_e = \frac{1}{n} \sum_{x=1}^n \beta_{e(i,j,k)_x} \left[P_{i,j,k}, \lambda_{i,j,k}, \phi_{i,j,k}, \alpha_e \right]_{n=7} \quad (33)$$

3.2.4 Incident Angle Estimations and Flow Correction Angles

Once the angle of attack and sideslip estimate are calculated, the incident angle for each port can be calculated by the equation 15. Similarly, the flow correction parameters $\delta\alpha$ and $\delta\beta$ are calculated using the wind tunnel reference data as shown in equations 16 and 17

3.2.5 Calibration Coefficient

Calculation of the calibration coefficient ε is performed by using the incident angle θ_i estimated from the equation 15 using the local angle of attack α_e , the local Sideslip angle β_e , and the pressure hole arrangement angles ϕ_i , λ_i and the incident angle θ_i estimated for each pressure hole using the pressure value P_i , the uniform flow static pressure P_∞ , the impact pressure q_c , and the pressure field model expressed in equation 24.

First, equation 24 can be transformed to equation 34. The left side of this equation 34 can be expressed as a pressure coefficient C_{P_c} as shown in the following equation 35.

Since there are six holes of pressure holes, by summarizing the respective pressure

field models and setting the calibration coefficient ε as a function of the Mach number M_∞ , the local angle of attack α_e and the local sideslip angle β_e , the equation 36 can be expressed

$$\frac{P_i \theta_i - P_\infty}{q_c} = \cos^2 \theta_i + \varepsilon \sin^2 \theta_i \quad (34)$$

$$C_{p_c} \theta_i \equiv \frac{P_i \theta_i - P_\infty}{q_c} = \frac{P_i \theta_i - P_\infty}{P_t - P_\infty} \quad (35)$$

$$\begin{bmatrix} C_{p_c} \theta_1 - \cos^2 \theta_1 \\ \vdots \\ C_{p_c} \theta_6 - \cos^2 \theta_6 \end{bmatrix} = \begin{bmatrix} \sin^2 \theta_1 \\ \vdots \\ \sin^2 \theta_6 \end{bmatrix} * \varepsilon M_\infty, \alpha_e, \beta_e \quad (36)$$

In this equation 36, the incident angle is a value determined by the local angle of attack α_e and the local sideslip angle β_e , and there is almost no change to the incident angle θ_i due to the difference in pressure value distribution. Therefore, this equation 36 shows the relationship between the calibration coefficient ε and the pressure distribution for specific conditions of (Mach number M_∞ , local angle of attack α_e , local Sideslip angle β_e). Actually, the pressure coefficients $C_{p_c}(\theta_i)$ obtained from the pressure value P_i of each pressure hole have different geometrical relationships, so the values of the respective calibration coefficients ε_i obtained for each pressure hole are different. However, in this algorithm, since the calibration coefficient ε is defined from the Mach number M_∞ , the local angle of attack α_e and the local sideslip angle β_e , the calibration coefficient approximation is reproduced by using the least squares method so that the error between ε_i and the calibration coefficient ε is minimized (in Equation 37).

$$\varepsilon M_\infty, \alpha_e, \beta_e = \frac{\sum_{i=1}^n \sin^2 \theta_i [C_{p_c} \theta_i - \cos^2 \theta_i] \Big|_{n=6}}{\sum_{i=1}^n \sin^4 \theta_i \Big|_{n=6}} \quad (37)$$

The estimate of derived from equation 37 gives the minimum fit error with respect to the pressure distribution. The estimate, however, may not give the minimum error with respect to the reference Mach number.

$$\varepsilon^{(m+1)} = \varepsilon^{(m)} + \frac{\partial \varepsilon^{(m)}}{\partial M} [M_{ref} - M^{(m)}] \quad (38)$$

In equation 38, $\frac{\partial \varepsilon^{(m)}}{\partial M}$ is the sensitivity derivative of the calibration parameter with respect to Mach number, and $M^{(m)}$ is the Mach number solution at the m^{th} iteration. The derivative $\frac{\partial \varepsilon^{(m)}}{\partial M}$ is numerically determined by perturbing Mach number and determining the change in $\varepsilon^{(m)}$.

3.2.6 Mach Number, Static Pressure, and Impact Pressure Estimator

Once the values of α_e and β_e have been determined, then the incident angles at all of the ports are evaluated, and only q_c and P_∞ remain as unknowns in the pressure equations. As we know, ε is a function of Mach number and it is implicitly a function of P_∞ and q_c and the resulting system of equations is nonlinear. The solutions for P_∞ and q_c must be extracted iteratively. Defining the matrices as shown in equations 39 and 40:

$$M_j = \begin{bmatrix} \cos^2\theta_1 + \varepsilon^j \sin^2\theta_1 & 1 \\ \vdots & \vdots \\ \cos^2\theta_6 + \varepsilon^j \sin^2\theta_6 & 1 \end{bmatrix} \quad (39)$$

$$Q = \begin{bmatrix} q_1 & 0 & 0 & 0 & 0 & 0 \\ 0 & q_2 & 0 & 0 & 0 & 0 \\ 0 & 0 & q_3 & 0 & 0 & 0 \\ 0 & 0 & 0 & q_4 & 0 & 0 \\ 0 & 0 & 0 & 0 & q_5 & 0 \\ 0 & 0 & 0 & 0 & 0 & q_6 \end{bmatrix} \quad (40)$$

The original flow model (equation 24) can be used to develop an iterative estimator of the form shown in equation 41.

$$\begin{bmatrix} \hat{q}_c \\ \hat{P}_\infty \end{bmatrix}_{j+1} = \begin{bmatrix} M_{(j)}^T Q M_{(j)}^{-1} & M_{(j)}^T Q \end{bmatrix} \begin{bmatrix} P_1 \\ \vdots \\ P_6 \end{bmatrix} \quad (41)$$

The subscript (j) refers the result of the jth iteration. The notation $M_{(j)}$ refers to the matrix of equation 41, with being evaluated ε , using the values for Mach number resulting from the previous iteration. The q_i terms are weights which have a nominal value of 1.0. Setting the value of q_i to zero, weights the ith pressure reading out of the algorithm. Once q_c and P_∞ are estimated, Mach number can be computed using normal one-dimensional fluid mechanics relationships. Subsonically, Mach number can be calculated directly using isentropic flow laws expressed as shown in equations 42, 43 and 44, where for $\gamma = 1.4$.

$$\frac{p_0}{p_\infty} = \left(1 + \frac{\gamma-1}{2} M_\infty^2\right)^{\frac{\gamma}{\gamma-1}} \quad (42)$$

$$\frac{q_c}{p_\infty} = \left(1 + \frac{\gamma-1}{2} M_\infty^2\right)^{\frac{\gamma}{\gamma-1}} - 1 \quad (43)$$

$$M_\infty = \sqrt{\frac{2}{\gamma-1} \left\{ \left(\frac{q_c}{p_\infty} + 1\right)^{\frac{\gamma-1}{\gamma}} - 1 \right\}} \quad (44)$$

Supersonically, the solution is computed using the Rayleigh pitot equation which is derived from adiabatic normal shock wave relationships shown in equation 45.

For $\gamma = 1.4$

$$\begin{aligned} \frac{P_{02}}{P_\infty} &= \frac{P_{02}}{P_{01}} \frac{P_{01}}{P_\infty} \\ &= \left\{ \left(\frac{\gamma+1}{\gamma-1} \frac{M_\infty^2}{M_\infty^2+2} \right) \left(1 + \frac{\gamma-1}{2} M_\infty^2 \right) \right\}^{\frac{\gamma}{\gamma-1}} \times \left(\frac{\gamma+1}{2\gamma M_\infty^2 - \gamma - 1} \right)^{\frac{1}{\gamma-1}} \\ &= \left(\frac{\gamma+1}{2} \frac{M_\infty^2}{M_\infty^2+2} \right)^{\frac{\gamma}{\gamma-1}} \left(\frac{\gamma+1}{2\gamma M_\infty^2 - \gamma - 1} \right)^{\frac{1}{\gamma-1}} \end{aligned} \quad (45)$$

Where P_{01} the total pressure ahead of the shock wave is, P_{02} is the total pressure behind the shock wave. Equation 44 is solved using a Taylor series expansion and a reversion of series to solve for Mach number. This expression is shown in equation 46.

$$M_\infty = \frac{\sqrt{\sum_{i=0}^9 r_i(W^i)}}{W} \quad (46)$$

Here $W = 1.839371 \frac{P_\infty}{P_{t2}}$ and the coefficients of the summation are $r = [1.42857, -0.357143, -0.0625, -0.025, -0.012617, -0.00715, -0.0043458, 0, 0, -0.0087725]$. In theory the ε calculated using equations 37 and 40 should give similar results, however this is not the case and the results obtained are slightly different.

3.3 Evaluation of the FADS Calibration

The calibration parameters were estimated from the wind tunnel data using measured pressures to estimate α_e and β_e by means of the triples algorithm. Results for α_e and β_e are used with wind tunnel reference conditions for M_∞ and q_c to predict surface pressures at the measurement locations. The residuals between the predicted and measured pressures were then used to calculate for each test point using linear regression. Finally, trends in the residuals are curve fit to produce the calibrations. A description of the three component parts of the calibration follows, in detail.

3.3.1 Angle of Attack Calibration

The angle of attack calibration relates the local angle of attack to the free stream value. Residuals between the wind tunnel reference conditions and the estimates for α_e were curve fit with third order polynomials in α_e to give the correction factor $\delta\alpha$. The coefficients of the fit were scheduled as a function of M_∞ . The resulting calibration function is expressed in equation 47.

$$\delta\alpha = A_0(M_\infty) + A_1(M_\infty)\alpha_e + A_2(M_\infty)\alpha_e^2 + A_3(M_\infty)\alpha_e^3 \quad (47)$$

The true angle of attack is evaluated by subtracting the correction factor $\delta\alpha$ from the estimated value. Here $A_0 \sim A_3$ are calibration coefficients.

3.3.2 Sideslip Angle Calibration

In a manner identical to the angle of attack calibration, the sideslip angle calibration relates the correction to the local sideslip angle sensed by the FADS to the free stream value. The wind tunnel residual data were fit with third order polynomials β_e in with the coefficients scheduled as a function of Mach number. The resulting calibration function is expressed in equation 48.

$$\delta\beta = B_0(M_\infty) + B_1(M_\infty)\beta_e + B_2(M_\infty)\beta_e^2 \quad (48)$$

Here $B_0 \sim B_2$ are calibration coefficients.

3.3.3 Position Error ε Calibration

The position error calibration parameter adjusts the FADS pressure model for changes in the incident angle and Mach number. The wind tunnel data were curve fit with second order polynomials in angle of attack and sideslip angle, and the coefficients scheduled as a function of Mach number. The resulting calibration model is expressed in equation 49.

$$\varepsilon = \varepsilon_M(M_\infty) + \varepsilon_{\alpha_1}(M_\infty)\alpha_e + \varepsilon_{\alpha_2}(M_\infty)\alpha_e^2 + \varepsilon_{\beta_1}(M_\infty)\beta_e + \varepsilon_{\beta_2}(M_\infty)\beta_e^2 \quad (49)$$

During the implementation during flight test, there is no access to the Mach number, however if an epsilon is given in the equation 41, a Mach number estimate can be obtained. And due to the fact that a table of epsilon for various Mach number, angle of attack and sideslip angle is available (in equation 37), if the Mach number is known

an epsilon is known. This implies that a convergence method should be used with the two relations mentioned above. However the true epsilon and the one obtained with the equation 41 are different, as a consequence a $\delta\epsilon = \epsilon_{true} - \epsilon_{estimated}$ needs to be computed for relating the true epsilon and the estimated one which can be estimated using equation 50.

$$\begin{aligned} \delta\epsilon = & \delta\epsilon_M(M_\infty) + \delta\epsilon_{\alpha_1}(M_\infty)\alpha + \delta\epsilon_{\alpha_2}(M_\infty)\alpha^2 + \delta\epsilon_{\beta_1}(M_\infty)\beta \\ & + \delta\epsilon_{\beta_2}(M_\infty)\beta^2 \end{aligned} \tag{50}$$

CHAPTER 4. RESULTS AND ANALYSIS

4.1 Results of the Estimation Algorithm

The results for different Mach number condition M_∞ obtained from the wind tunnel test carried out so far are discussed in this chapter. The results for Mach number $M=0.5$ (2014), $M=0.9$ (2015), $M=1.0$ (2015), $M=2.0$ (2015) are shown. Using the wind tunnel data for various conditions of angle of attack, sideslip attack and Mach number, the results of the estimation algorithm are shown below:

4.1.1 Surface Pressure Distribution Results

The pressure measurement results p_i for each pressure hole of FADS specimen are described. Figure 33 shows the relationship between each pressure hole and colour. The pressure measurements p_i of each pressure port for Mach number $M=0.5$ (2014), $M=0.9$ (2015), $M=1.0$ (2015), $M=2.0$ are shown in Figure 34. The reference angle of attack α_{ref} is shown on the horizontal axis and the pressure measurements p_i is shown on the vertical axis. These results are for the case when reference sideslip angle β_{ref} is 0° .

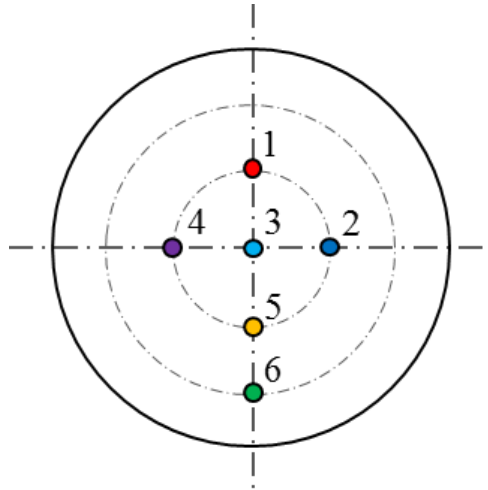


Figure 33 – Color arrangement of pressure ports

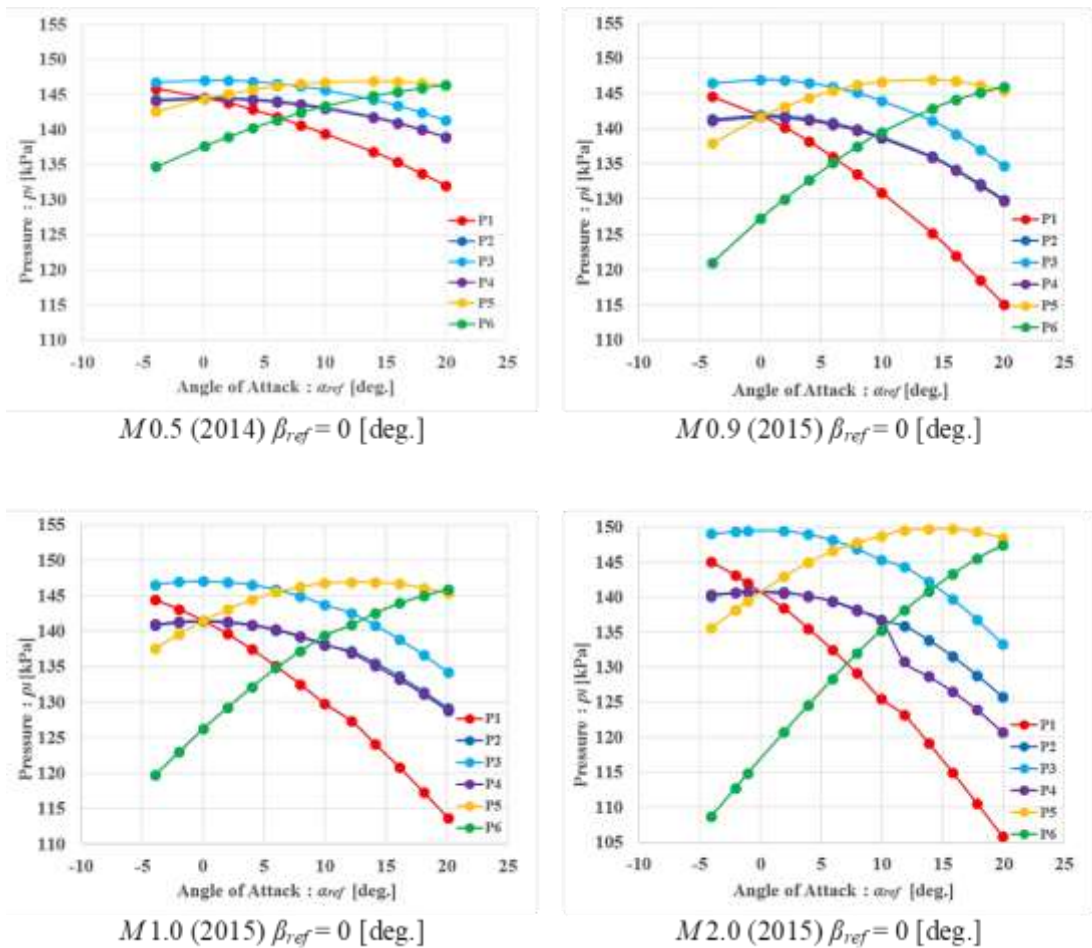


Figure 34 – Pressure distribution measurements for various Mach numbers

From Figure 34, when the main stream angle of attack α_{ref} is 0° , the pressure measurements p_i for holes 1, 2, 4, 5 coincide. Similar results are obtained for the pressure measurements p_i for different angle of attack for various Mach number M_∞ conditions. As an exception, however for $M=2.0$, when the reference sideslip angle β_{ref} is 0° , the pressure holes 2 and 4 which have the same geometric relationship should have same pressure measurements p_i . However, for reference angle of attack α_{ref} greater than 10° the pressure measurements do not coincide.

4.1.2 Estimation for Calibration Coefficient ε

The calibration coefficient ε is calculated from the pressure measurements p_i of each pressure hole for various Mach number M_∞ measured by the wind tunnel test. To obtain the calibration coefficient ε , local angle of attack α_e and local sideslip angle β_e should be estimated.

4.1.2.1 Results for Local Angle of Attack α_e and Local Sideslip Angle β_e

Local attack angle α_e and sideslip angle β_e results are estimated using the pressure measurements p_i of the each pressure holes and the geometrical angles λ_i , ϕ_i of each pressure holes for various Mach conditions are shown in Figure 35 to Figure 38. In each graph, the vertical axis represents the local angle of attack α_e and the local sideslip angle β_e estimated from the algorithm, and the horizontal axis shows the reference angle of attack α_{ref} and the reference sideslip angle β_{ref} .

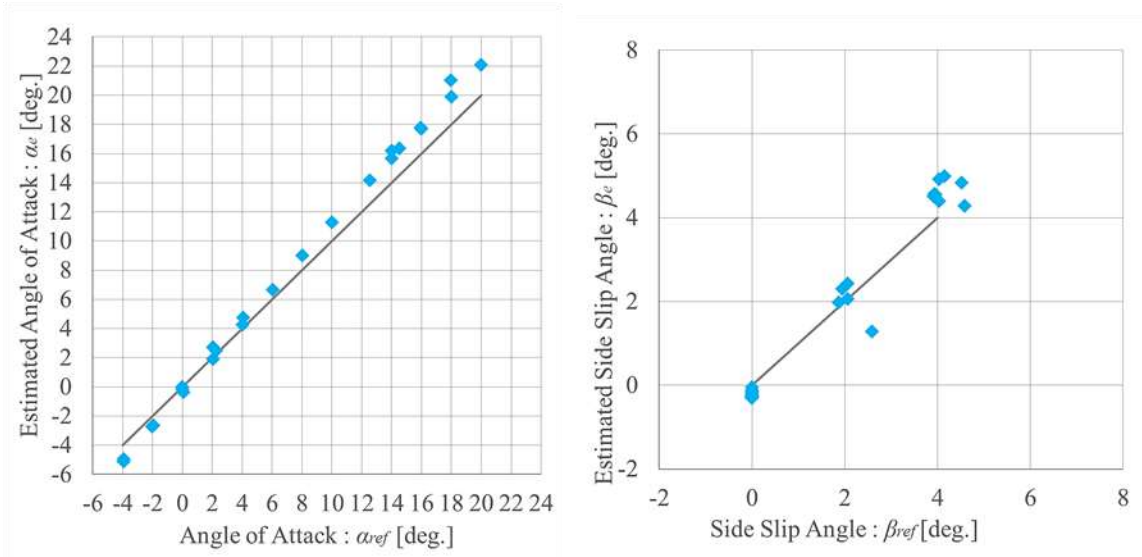


Figure 35 – Local angle of attack and local sideslip angle estimation results for $M=0.5$

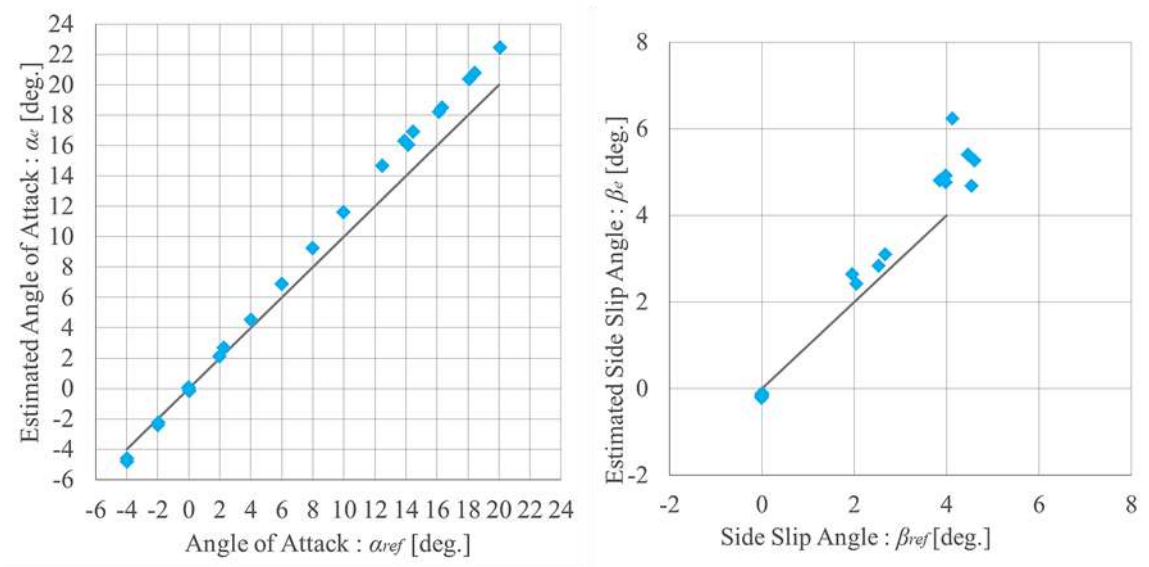


Figure 36 – Local angle of attack and local sideslip angle estimation results for $M=0.9$

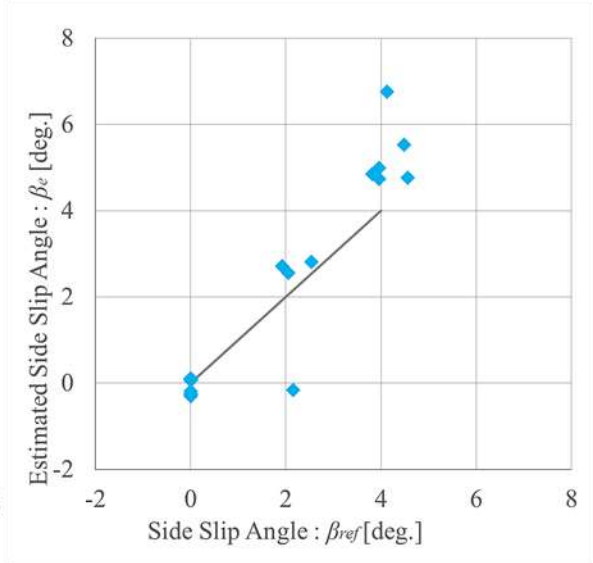
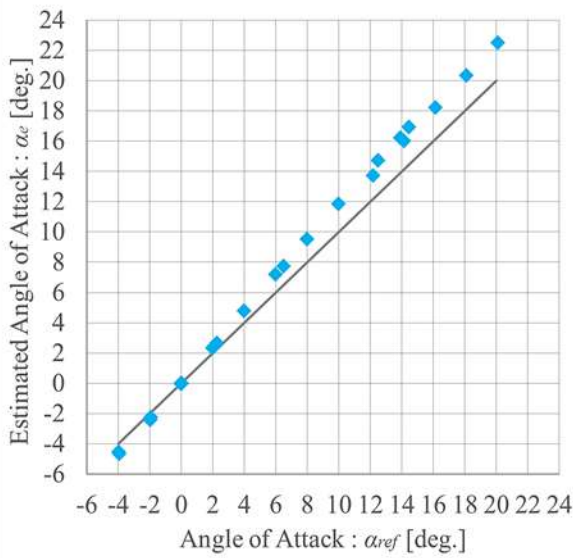


Figure 37 – Local angle of attack and local sideslip angle estimation results for M1.0

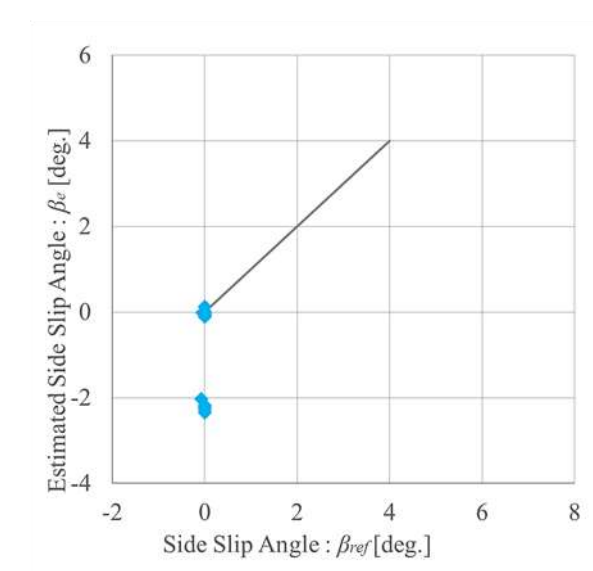
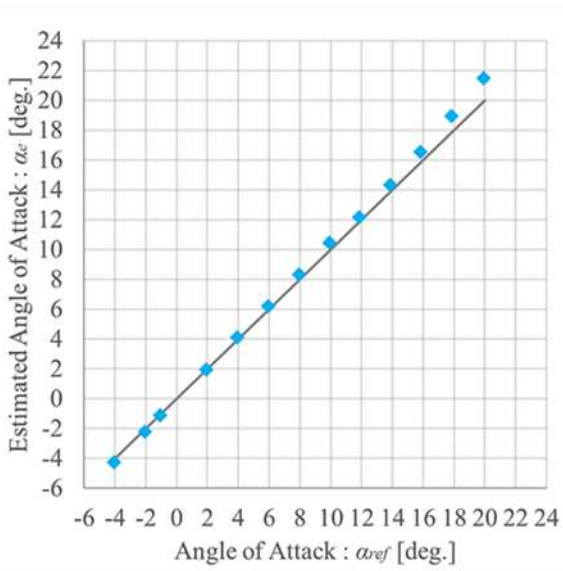


Figure 38 – Local angle of attack and local sideslip angle estimation results for M2.0

From above results, it can be observed that estimation of local angle of attack α_e for different Mach number conditions was estimated with high accuracy. On the other hand, for local sideslip angle β_e , the estimation accuracy varies for different local angle of attack α_e in the subsonic range. However, comparing with the results

of local angle of attack α_e , results of local sideslip angle β_e deteriorated. In supersonic range, there are cases where the estimation results deviated from the reference inputs.

4.1.2.2 Estimation Results for Incident Angle θ_i

Using the estimated local angle of attack α_e , the local sideslip angle β_e , and the geometric parameters λ_i , ϕ_i of each pressure hole are substituted into equation 15.

Figure 39 shows the incident angle θ_i results for various Mach number M_∞ conditions.

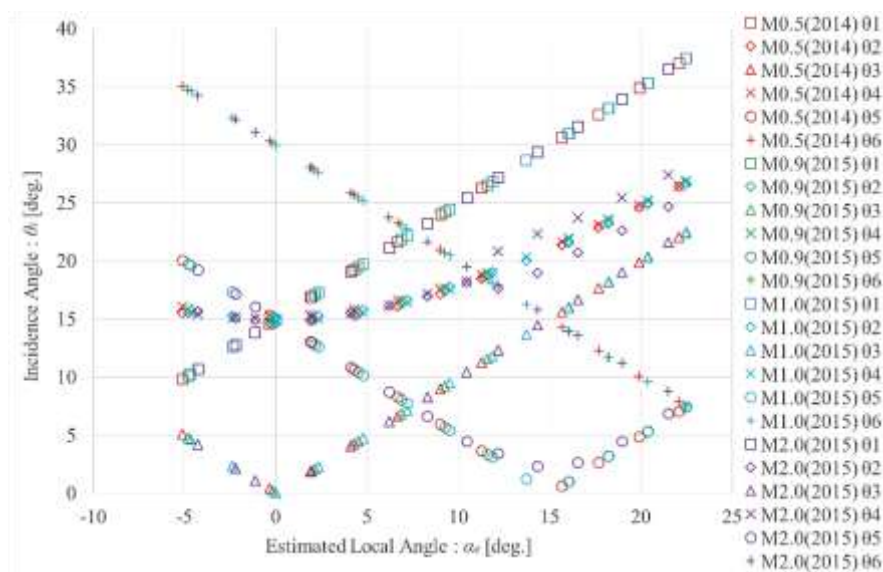


Figure 39 – Results of incident angle θ_i ($\beta_{ref} = 0$ [deg.]

4.1.2.3 Estimation Results for Position Error ε

The calculated incident angle θ_i , pressure measurement p_i from the wind tunnel test, static pressure P_∞ and the stagnation point total pressure are taken as inputs in equation 37 to estimate the position error ε . Here, the stagnation point total pressure uses the maximum value measured for pressure hole 3. Figure 40 shows the estimation results for various Mach number M_∞ conditions.

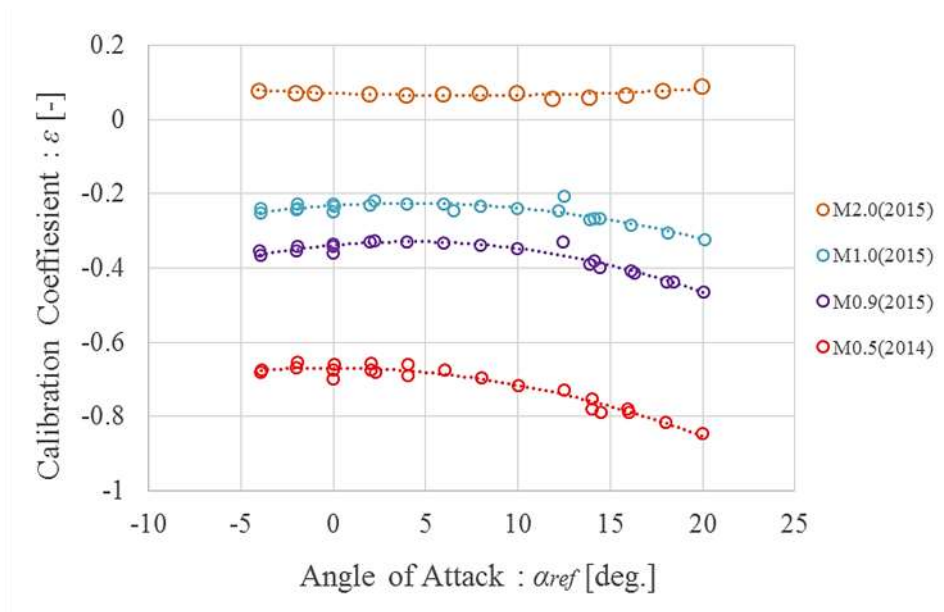


Figure 40 – Results of estimated calibration coefficient ϵ ($\beta_{ref} = 0, 2, 4$) [deg.]

4.1.2.4 Calibration Results for Mainstream Angle of Attack α_{∞} and Mainstream Sideslip Angle β_{∞}

As mentioned in previous chapter, equations 16, 17, 47 and 48 gives us the mainstream angle of attack α_{∞} and mainstream sideslip angle β_{∞} . Calibration results of local angle of attack and local Sideslip angle are shown from Figure 41 to Figure 44 for various Mach number conditions. For Mach number $M=2.0$, data is only available when the reference sideslip angle β_{ref} is 0° , hence the calibration is not successful.

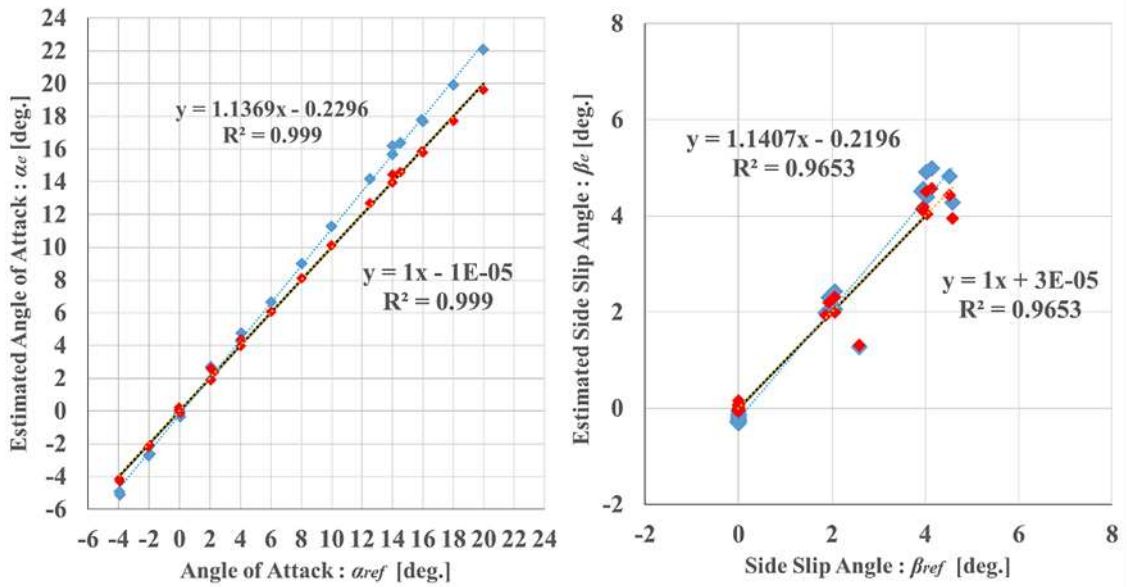


Figure 41 – Calibrated angle of attack and sideslip angle results at $M=0.5$

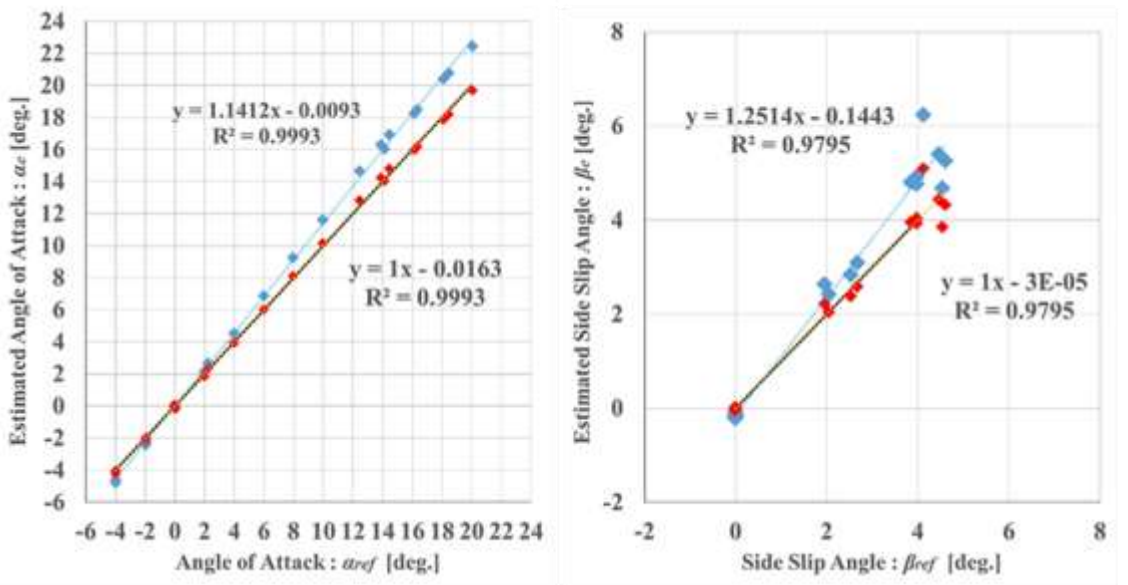


Figure 42 – Calibrated angle of attack and sideslip angle results at $M=0.9$

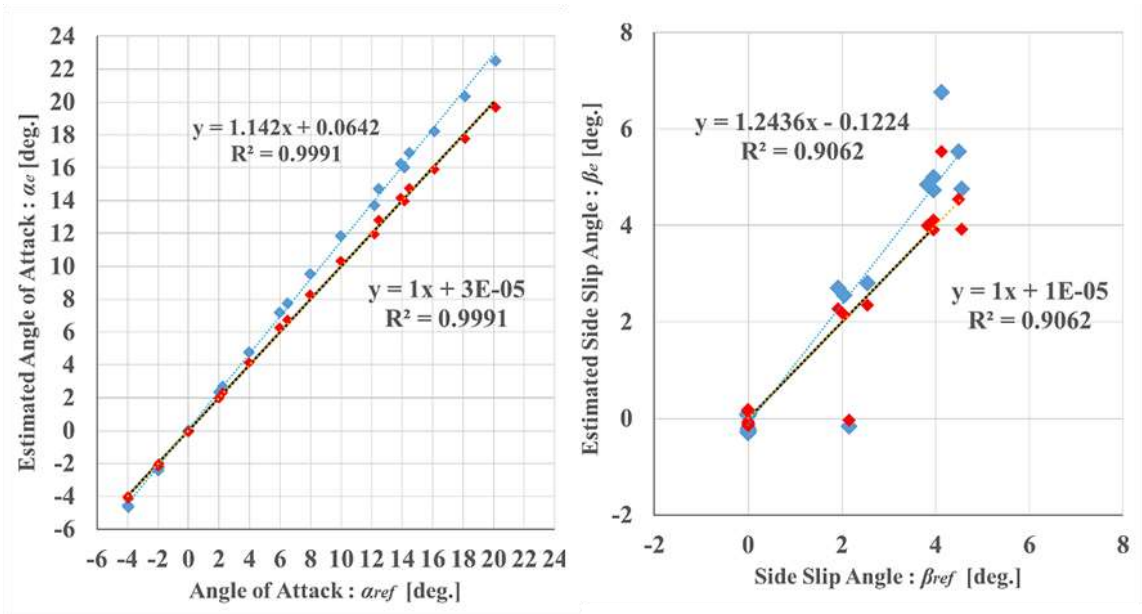


Figure 43 – Calibrated angle of attack and sideslip angle results at $M=1.0$

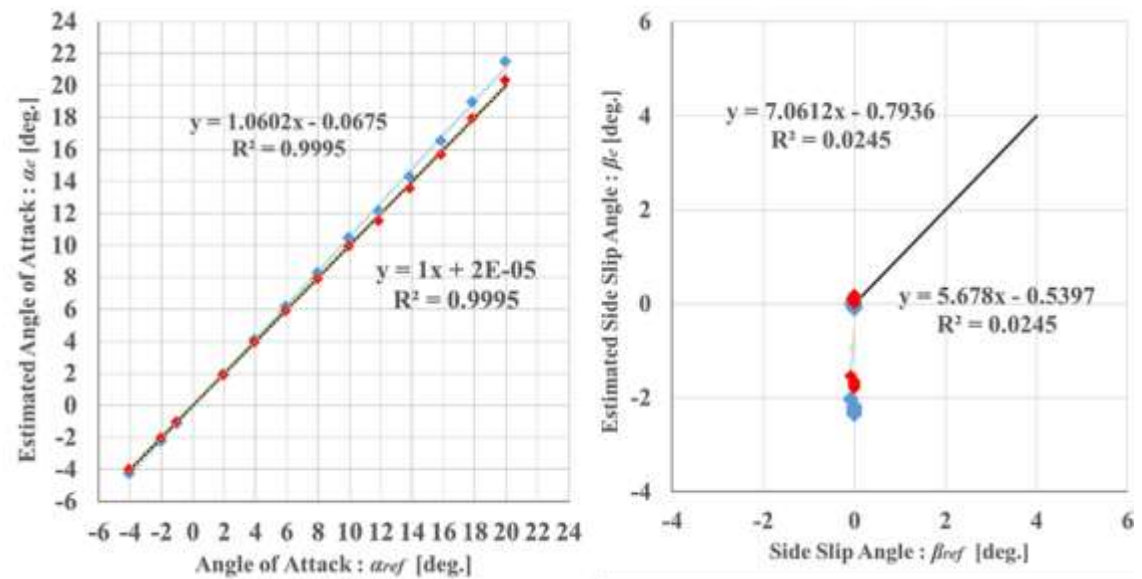


Figure 44 – Calibrated angle of attack and sideslip angle results at $M=2.0$

4.2 Analysis of the Estimation Results

4.2.1 Estimated Result of Local Sideslip Angle

As described in Section 4.1.2.1, the estimation accuracy of the local sideslip angle β_e deteriorated with the estimated local angle of attack α_e . Figure 45 shows the estimation result of the local sideslip angle β_e for the calibration algorithm of the Mach number $M=0.9$ as an example. It can be understood that the sideslip angle estimates deteriorated at higher angle of attack.

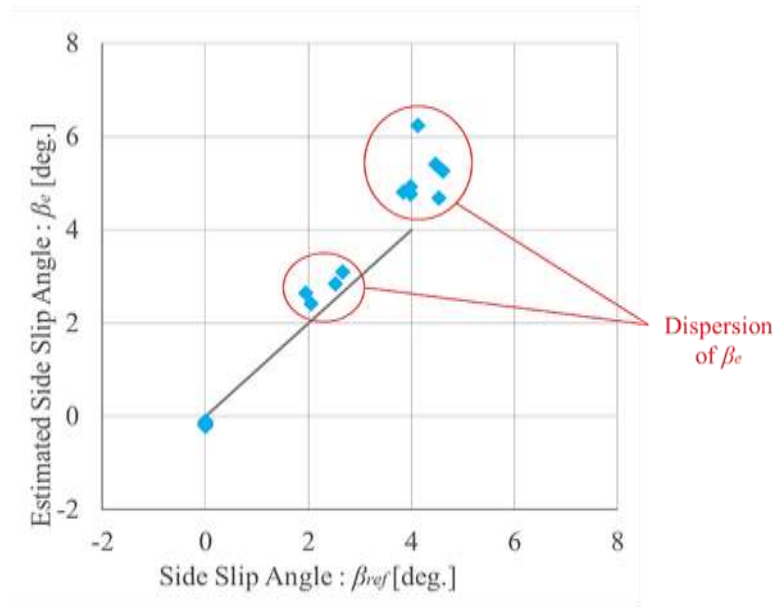


Figure 45 – Dispersion of estimated sideslip angle

For the estimation of the local sideslip angle β_e , as shown in Section 3.2.3, seven combinations of triples are strategically selected from the available 6 holes. The final estimate is the average value of the seven combinations for local sideslip angle β_e . Combinations used for estimating the local sideslip angle β_e are, symmetrical combinations such as 1, 2, 5, asymmetry combinations in the form of mirror image pair 3, 4, and 6, 7 shown in Figure 46.

In order to investigate the cause of this phenomenon, first, the estimation results of each local slip angle β_e for each combination of pressure holes are investigated. Table 9 shows the relationship between the estimation results of the local sideslip angle β_e for each combination of 1 to 7, reference angle of attack α_{ref} , reference sideslip angle β_{ref} , and the final average value. In addition, Figure 47 shows the deviation of the local Sideslip angle β_e estimated for each combination when the sideslip angle $\beta_{ref} = 0$ deg. Figure 48 shows the case when sideslip angle $\beta_{ref} = 2$ deg. and Figure 49 shows the case when the sideslip angle $\beta_{ref} = 4$ deg.

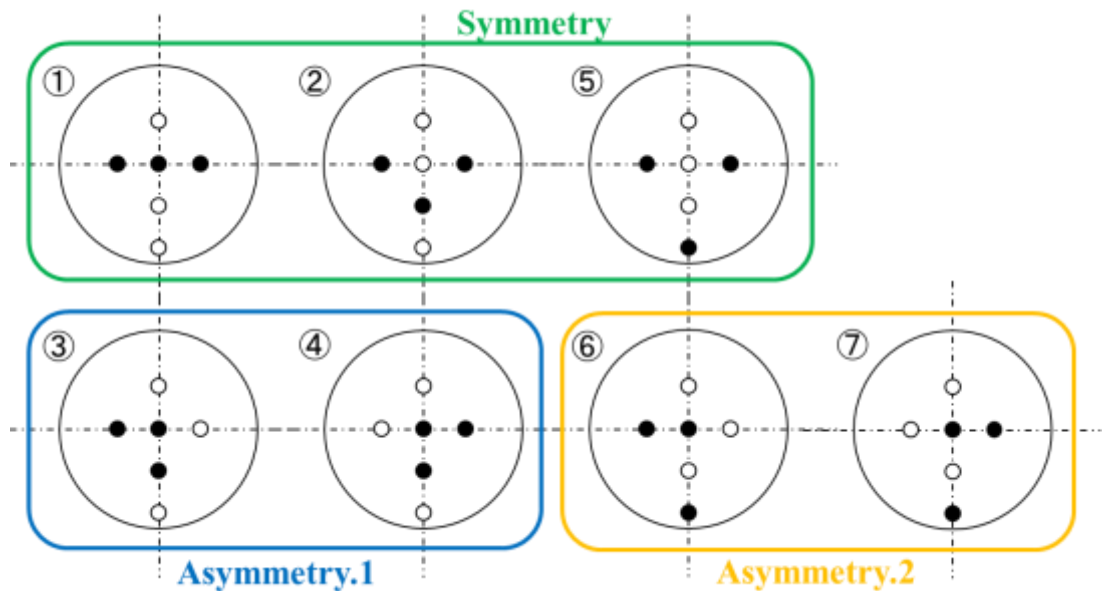


Figure 46 – Symmetry and asymmetry port combination for sideslip angle estimation

Table 9 – Sideslip angle estimation for each port combination at M0.9 (2015)

Target Value [deg.]		True Value [deg.]		Estimated Side Slip Angle [deg.]								Average
Alpha	Beta	Alpha	Beta	①	②	③	④	⑤	⑥	⑦		
-4	0	-3.97	0.00	-0.188	-0.183	-0.102	-0.270	-0.184	-0.069	-0.301	-0.185	
0	0	0.01	0.00	-0.196	-0.172	-0.174	-0.216	-0.193	-0.130	-0.257	-0.191	
2	0	2.00	0.00	-0.209	-0.210	-0.189	-0.227	-0.210	-0.230	-0.188	-0.209	
4	0	3.99	0.00	-0.194	-0.196	-0.065	-0.316	-0.199	-0.327	-0.068	-0.195	
6	0	5.98	0.00	-0.184	-0.188	1.328	-1.622	-0.194	-0.394	0.016	-0.177	
8	0	7.96	0.00	-0.152	-0.157	-1.591	1.228	-0.173	-0.482	0.164	-0.166	
10	0	9.97	0.00	-0.154	-0.160	-1.040	0.696	-0.088	-0.696	0.366	-0.154	
14	0	14.14	0.00	-0.120	-0.125	-0.769	0.509	-0.116	0.714	-0.925	-0.119	
16	0	16.12	0.00	-0.103	-0.107	-0.581	0.361	-0.102	0.083	-0.283	-0.104	
18	0	18.09	0.01	-0.136	-0.141	-0.499	0.213	-0.135	-0.026	-0.242	-0.138	
20	0	20.08	0.00	-0.149	-0.153	-0.433	0.124	-0.147	-0.059	-0.234	-0.150	
-2	2	-1.95	1.95	2.749	2.400	2.906	2.491	2.604	2.949	2.396	2.642	
0	2	0.00	2.53	3.050	0.960	2.974	3.343	3.158	2.932	3.443	2.837	
14	2	14.44	2.05	2.352	2.467	1.913	3.297	2.321	2.532	2.058	2.420	
16	2	16.34	2.67	2.997	3.135	2.667	3.932	2.971	3.068	2.927	3.100	
-4	4	-3.99	3.98	5.091	4.558	5.197	4.815	4.804	5.203	4.778	4.921	
-2	4	-1.98	3.98	4.689	4.692	4.689	4.947	4.713	4.678	4.997	4.772	
0	4	-0.01	4.54	5.308	9.823	5.284	5.782	5.500	5.247	6.005	6.136	
2	4	2.24	4.47	5.246	5.293	5.256	5.502	5.454	5.183	5.938	5.410	
12	4	12.46	4.12	4.842	5.049	4.619	6.284	4.628	2.845	15.447	6.245	
14	4	13.90	3.85	4.746	4.928	4.566	5.932	4.629	4.964	3.916	4.812	
18	4	18.45	4.60	5.104	5.256	5.014	6.028	5.060	5.131	5.248	5.263	

□ Faulty Value

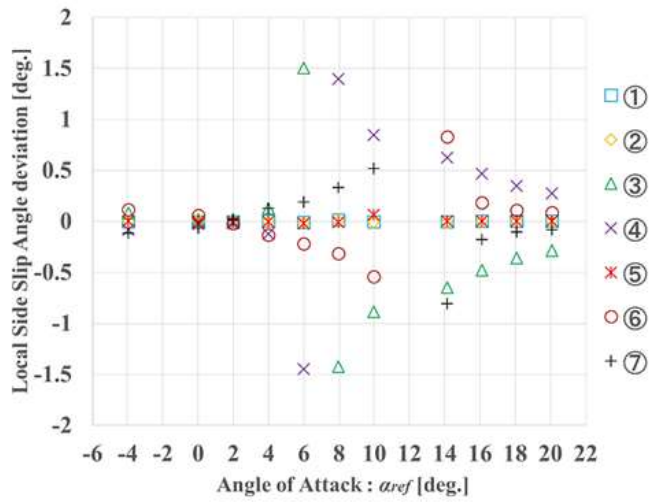


Figure 47 – Local Sideslip angle deviation at $M=0.9$ ($\beta_{ref} = 0$ [deg.]

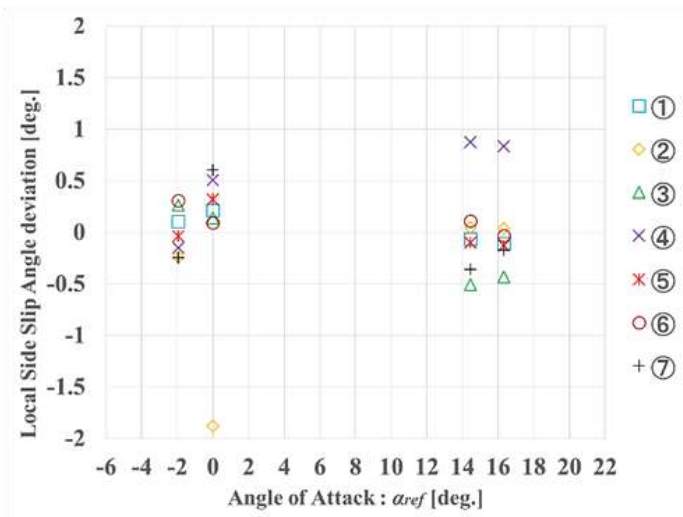


Figure 48 – Local Sideslip angle deviation at $M=0.9$ ($\beta_{ref} = 2$ [deg.]

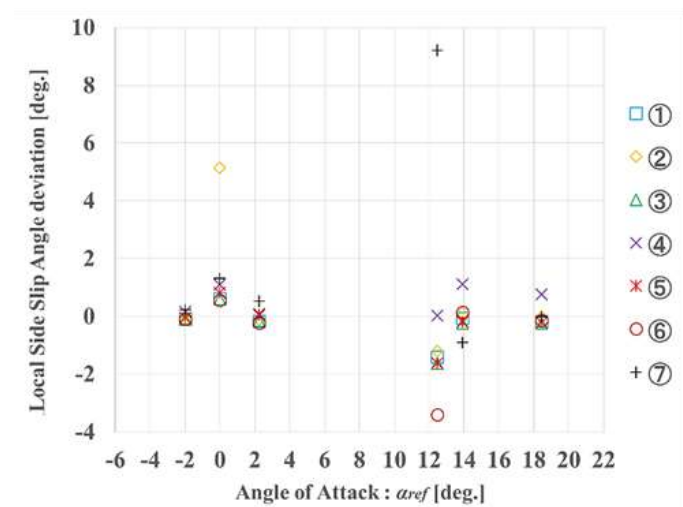


Figure 49 – Local Sideslip angle deviation at $M=0.9$ ($\beta_{ref} = 4$ [deg.]

When the reference sideslip angle β_{ref} is 0 deg., relatively good results are obtained in the final estimation result, however from Table 9 and Figure 47 if we observe the local sideslip angle β_e for each combination, the deviation for the mirror image combinations was cancelled out thus giving better results.

Similarly, for the reference sideslip angle β_{ref} is 2 and 4 deg., these mirror image pairs do not cancel each other. Therefore, there is a large deviation when estimating local sideslip angle β_e . Also some faulty point occurred for example when reference angle of attack α_{ref} is 0 deg., and reference sideslip angle β_{ref} is 2, 4 deg. The above tendency is also observed for other Mach number M_∞ conditions.

For reference, the estimated values of the local sideslip angle β_e for each combination in case of Mach number $M=0.5$ (2014) and Mach number $M=1.0$ (2015) are shown in Table 10 and Table 11.

Table 10 – Sideslip angle estimation for each port combination at $M=0.5$

Target Value [deg.]		True Value [deg.]		Estimated Side Slip Angle [deg.]							Average
Alpha	Beta	Alpha	Beta	①	②	③	④	⑤	⑥	⑦	
-4	0	-3.91	-0.01	-0.276	-0.293	-0.455	-0.110	-0.290	-0.584	0.010	-0.285
0	0	0.06	0.00	-0.266	-0.481	-0.424	-0.118	-0.281	-0.588	0.034	-0.303
2	0	2.04	0.00	-0.261	-0.253	-0.340	-0.186	-0.280	-0.660	0.112	-0.267
4	0	4.04	0.00	-0.241	-0.245	-0.047	-0.421	-0.264	-0.715	0.205	-0.247
6	0	6.03	0.00	-0.253	-0.264	1.640	-2.020	-0.287	-0.793	0.252	-0.246
8	0	8.01	0.00	-0.222	-0.235	-3.806	3.151	-0.286	-0.922	0.437	-0.269
10	0	10.02	0.00	-0.224	-0.239	-1.929	1.381	0.003	-1.154	0.652	-0.216
14	0	14.01	0.00	-0.181	-0.191	-1.026	0.623	-0.176	1.027	-1.329	-0.179
16	0	15.99	0.00	-0.140	-0.147	-0.712	0.409	-0.139	0.012	-0.287	-0.143
18	0	18.00	0.00	-0.116	-0.120	-0.587	0.341	-0.116	-0.110	-0.121	-0.118
20	0	19.98	0.00	-0.040	-0.041	-0.369	0.286	-0.040	-0.054	-0.026	-0.040
-2	2	-1.94	1.94	2.270	2.300	2.251	2.364	2.286	2.240	2.386	2.299
0	2	0.00	2.58	2.345	-5.848	2.233	2.627	2.541	2.024	3.030	1.279
2	2	2.07	2.06	2.375	2.307	2.288	2.611	2.461	2.247	2.691	2.426
14	2	14.51	2.06	2.000	2.137	1.306	3.291	1.956	2.399	1.333	2.060
16	2	15.94	1.87	1.928	2.018	1.495	2.734	1.909	2.047	1.763	1.985
-4	4	-3.93	3.92	4.452	4.395	4.467	4.618	4.467	4.443	4.717	4.508
-2	4	-2.01	4.03	4.688	4.969	4.643	5.145	4.941	4.567	5.486	4.920
0	4	-0.01	4.58	4.722	0.546	4.690	5.129	4.900	4.643	5.344	4.282
2	4	2.26	4.51	4.680	4.685	4.682	4.929	4.906	4.585	5.364	4.833
4	4	4.05	4.04	4.267	4.244	4.236	4.594	4.443	4.182	4.799	4.395
12	4	12.52	4.14	4.501	4.669	4.271	5.754	4.273	3.849	7.612	4.990
14	4	14.00	3.95	4.509	4.713	4.272	5.821	4.377	4.804	3.426	4.560

□ Faulty Value

Table 11 – Sideslip angle estimation for each port combination at $M=1.0$

Target Value [deg.]		True Value [deg.]		Estimated Side Slip Angle [deg.]								Average
Alpha	Beta	Alpha	Beta	①	②	③	④	⑤	⑥	⑦		
-4	0	-3.94	0.00	0.101	0.104	0.036	0.169	0.102	0.057	0.147	0.102	
-2	0	-1.98	0.00	0.098	0.104	0.007	0.192	0.100	0.031	0.168	0.100	
0	0	0.02	0.00	0.075	0.013	-0.024	0.192	0.084	-0.005	0.172	0.072	
2	0	1.99	0.00	0.101	0.098	-0.008	0.213	0.104	-0.059	0.265	0.102	
4	0	3.99	0.00	0.087	0.087	0.183	-0.012	0.092	-0.174	0.354	0.088	
6	0	5.99	0.00	0.085	0.087	2.595	-2.484	0.092	-0.249	0.427	0.079	
8	0	7.98	0.00	0.074	0.077	-1.443	1.624	0.094	-0.443	0.602	0.084	
10	0	9.98	0.00	0.061	0.064	-0.953	1.091	0.040	-0.672	0.806	0.062	
12	0	12.17	0.00	-0.179	-0.188	-1.006	0.608	-0.166	-1.559	1.134	-0.194	
14	0	14.14	0.00	-0.277	-0.293	-1.097	0.482	-0.271	0.487	-0.984	-0.279	
16	0	16.12	0.00	-0.291	-0.306	-0.981	0.346	-0.290	-0.255	-0.323	-0.300	
18	0	18.11	0.00	-0.240	-0.251	-0.807	0.290	-0.241	-0.305	-0.178	-0.247	
20	0	20.11	0.01	-0.246	-0.255	-0.656	0.137	-0.246	-0.280	-0.213	-0.251	
-2	2	-1.92	1.92	2.861	2.382	3.069	2.483	2.672	3.107	2.396	2.710	
0	2	0.00	2.54	3.138	-0.071	3.003	3.587	3.317	2.952	3.715	2.806	
6	2	6.49	2.15	2.704	2.801	48.313	-63.865	3.096	2.389	3.476	-0.155	
16	2	14.46	2.05	2.453	2.599	1.923	3.621	2.428	2.586	2.249	2.551	
-4	4	-3.97	3.96	5.253	4.539	5.382	4.804	4.859	5.392	4.743	4.996	
-2	4	-1.97	3.96	4.611	4.731	4.593	4.940	4.681	4.577	5.009	4.735	
0	4	-0.01	4.56	5.408	-0.645	5.367	6.009	5.645	5.338	6.199	4.760	
2	4	2.25	4.48	5.333	5.276	5.320	5.745	5.612	5.254	6.157	5.528	
12	4	12.48	4.13	4.867	5.081	4.643	6.338	4.658	2.065	19.706	6.765	
14	4	13.90	3.82	4.741	4.948	4.533	6.060	4.647	4.926	4.082	4.848	

□ Faulty Value

4.2.2 Evaluation of Calibration Coefficient using Theoretical Approach

The pressure model expressed in equation 24 mentioned in Chapter 3 can be written as equation 34. In this equation, the left side represents the measured values such as the pressure value P_i measured from each pressure hole, uniform flow total pressure P_∞ , impact pressure q_c , obtained from the wind tunnel test as shown in equation 51. The right side represents the estimated values from the incident angle θ_i and the calibration coefficient ε calculated by the calibration algorithm as shown in equation 52. Although the pressure field model in practical application has some error for the experiment value and the estimated value. An attempt was made to evaluate the calibration coefficient ε estimated by this error. This error ΔC_{pc} is shown in equation 53.

$$C_{Pc}(Measured) = \frac{P_i(\theta_i) - P_\infty}{q_c} \quad (51)$$

$$C_{Pc}(Estimated) = \cos^2 \theta_i + \varepsilon \sin^2 \theta_i \quad (52)$$

$$\Delta C_{pc} = C_{Pc}(Estimated) - C_{Pc}(Measured) \quad (53)$$

4.2.2.1 Evaluation of Pressure Coefficient

The pressure coefficient is calculated for different Mach number M_∞ condition such as $M=0.5$, 0.9 and 1.0 . Using equations 51 and 52 the results are shown in Figure 50, Figure 51 and Figure 52. The solid line shows C_{pc} (measured value), and the dotted line shows C_{pc} (estimated value).

The difference between the measured and estimated pressure coefficients is larger at lower condition of M_∞ such as $M=0.5$. The difference between the measured and estimated pressure coefficients becomes relatively smaller for higher Mach $M=0.9$ and 1.0 . There is a large difference for different Mach number M_∞ in the subsonic range. But on the other hand it was found that the values are almost equal at Mach number $M=1.0$.

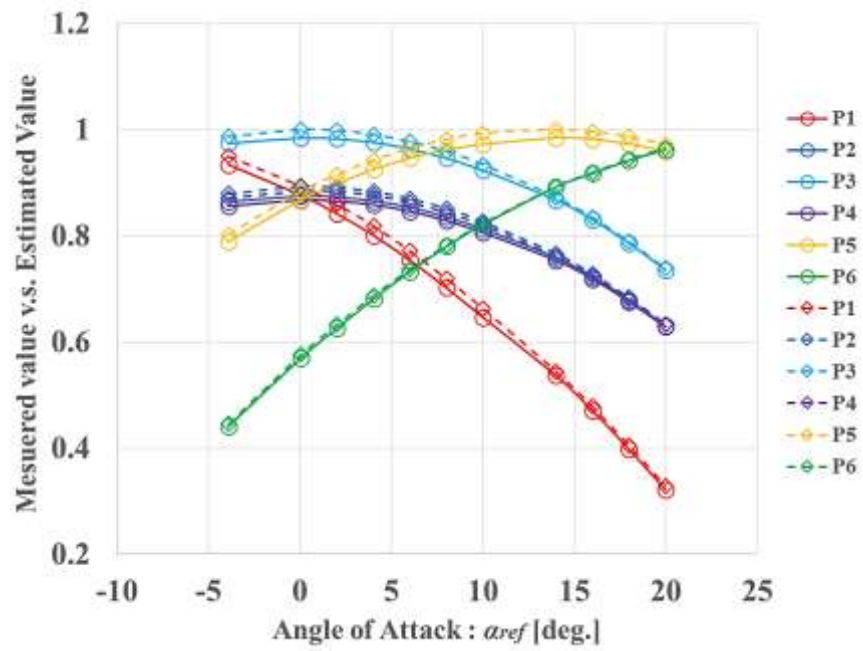


Figure 50 – C_{pc} measured v.s. estimated value at $M=0.5$

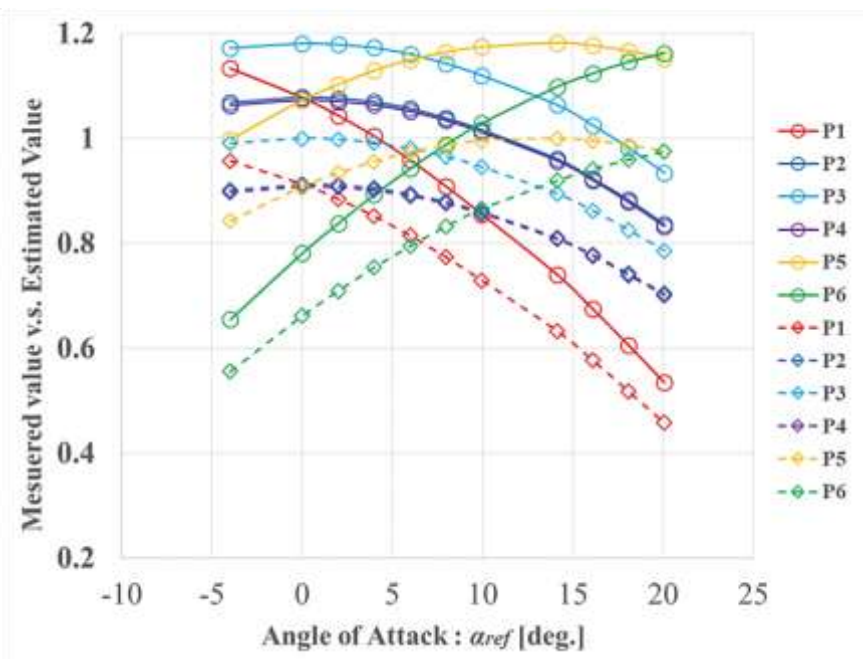


Figure 51 – C_{pc} measured v.s. estimated value at $M=0.9$

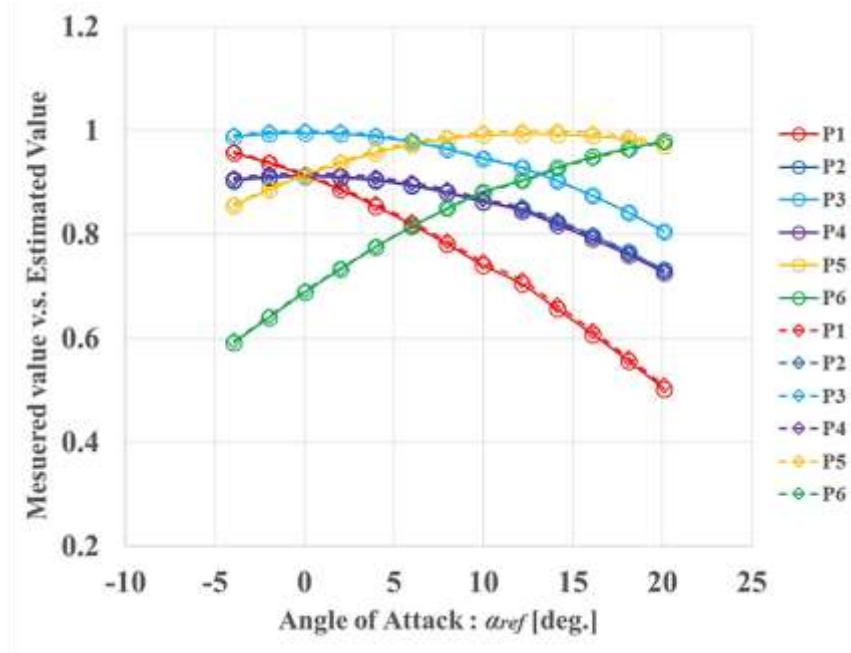


Figure 52 – C_{pc} measured v.s. estimated value at $M=1.0$

4.2.2.2 Estimation Result of Local Angle of Attack α_e

Local angle of attack α_e and the local sideslip angle β_e are estimated using the theoretical pressure distribution approach. For comparison, the local angle of attack α_e and the local sideslip angle β_e by wind tunnel test data are shown. Estimated pressure measurement data from the wind tunnel test for Mach number $M = 0.5, 0.9$ and 1.0 . The local angle of attack α_e is estimated using four combinations of pressure holes in Figure 31 mention in Chapter 3. In the estimation by the theoretical pressure distribution, when the target angle of attack is 0 [deg.], singularities occurred in the combinations 1 and 4 as shown in Table 12. This occurs in all the Mach number conditions of the estimation based on the theoretical pressure distribution. Due to the problem of graph display, data for which a singular point with target angle of attack $\alpha_{target} = 0$ [deg.] was obtained was excluded.

Table 12 – Local angle of attack estimates ($\beta_{target}=0$ [deg.], $M=0.5$)

α_{target} [deg.]	Pressure Port Combinations			
	1	2	3	4
-2	-1.998	-1.995	-1.999	-1.998
-1	-1.001	-1.000	-1.001	-1.001
0	-90.000	-1.001	0.002	-90.000
1	1.001	-1.001	0.999	1.000
2	1.998	-1.001	1.999	1.999

However, as described above, the estimation at the target angle of attack $\alpha_{target} = 0$ [deg.] gives the estimation result of -90[deg.] in the combinations 1 and 4, so when taking the average for the final local azimuth estimation, it is approximately -45[deg.]. Therefore, the estimation of local slip angle β_e at the above mentioned conditions are impossible.

4.2.2.3 Estimation Results of the Local Sideslip Angle β_e

Estimation of the local Sideslip angle β_e is performed using seven combinations of pressure holes shown in Figure 32 of Chapter 3. Also, in this estimation based on the theoretical pressure distribution, when the target sideslip angle $\beta_{target} = 0$ [deg.], singularities as indicated by red letters in the combinations A, B and E are obtained in the following Table 4-2. Furthermore, the estimation result for the target sideslip angle $\beta_{target} = 15$ [deg.] in combinations F and G is displayed as * as shown in Table 13 because of the singularity raised due to the denominator of the triples algorithm (equation 25) became zero.

Table 13 – Local sideslip angle estimates ($\beta_{target}=0$ [deg.], $M=0.5$)

α_{target} [deg.]	Pressure Port Combinations						
	A	B	C	D	E	F	G
13	-90.000	-90.000	-0.001	0.001	-90.000	-0.001	0.001
14	-90.000	-90.000	0.000	0.000	-90.000	0.002	-0.002
15	-90.000	-90.000	0.002	-0.002	-90.000	*	*
16	-90.000	-90.000	0.001	-0.001	-90.000	-0.002	0.002
17	-90.000	-90.000	-0.004	0.004	-90.000	0.000	0.000

Estimation of the local sideslip angle β_e uses the estimation result of the local angle of attack α_e as described in Chapter 3, so when the target angle of attack $\alpha_e = 0$ [deg.] the singular point is generated by estimation, the local Sideslip angle β_e cannot be estimated accurately.

4.2.3 Features of Singularity

From the above results, it was found that there is similarity between the singularity points obtained by the estimation result of the local sideslip angle β_e by the theoretical pressure distribution. The similarity is summarized in Table 14 below.

Table 14 – Similarity of singularity in local slip angle estimation by theoretical pressure distribution

Pressure Port Combinations	Sideslip Angle Condition	
	$\beta_{target} = 0[\text{deg.}]$	$\beta_{target} = 2[\text{deg.}], 4[\text{deg.}]$
A, B, E	<ul style="list-style-type: none"> Occurs for all target angle of attack α_{target} 	<ul style="list-style-type: none"> Does not occur
C, D	<ul style="list-style-type: none"> Similar to wind tunnel test, occurs at $\alpha_{target}=8[\text{deg.}]$ 	<ul style="list-style-type: none"> As β_{target} becomes larger, one of the errors of C and D becomes larger and the other terms becomes smaller
E	<ul style="list-style-type: none"> At $\alpha_{target}=15[\text{deg.}]$, there is no singularity in the combination E 	<ul style="list-style-type: none"> As β_{target} becomes larger, error becomes larger
F, G	<ul style="list-style-type: none"> For $\alpha_{target}=15[\text{deg.}]$, singularity arises due to the triples algorithm failure 	<ul style="list-style-type: none"> For $\beta_{target}=0[\text{deg.}]$, singularity arises due to the triples algorithm failure

First, the singularities occurring at the target sideslip angle $\beta_{target} = 0[\text{deg.}]$ of the combinations A, B and E occur under all Mach number conditions. Regarding the singularities occurring in combinations C and D, it is also reported in Moriyama et al. [7] that target singularity occurs symmetrically at the target Sideslip angle $\beta_{target} = 0[\text{deg.}]$. However, in the case of the target Sideslip angle $\beta_{target} = 2[\text{deg.}]$ and $4[\text{deg.}]$, it was found that the error for one of the combination was large and other was small.

In particular, the results of the wind tunnel test with the Mach number $M = 1.0$ show that the combination C is $48.3[\text{deg.}]$ and the combination D is $-63.8[\text{deg.}]$ for

the target angle of attack $\alpha_{target} = 6[\text{deg.}]$, and in actual flight it is thought that singular points with large errors will affect the estimation. Also, in this study, we found that a large error occurred at the target angle of attack $\alpha_{target} = 11[\text{deg.}]$.

Furthermore, in the estimation of the target angle of attack $\alpha_{target} = 15[\text{deg.}]$ for the combinations F and G, the triples algorithm becomes invalid as the denominator of the triples equations is zero making the calculation impossible. It was also confirmed that this is one of the conditions for the occurrence of singular point.

4.3 Countermeasures for Singularity

4.3.1 Cause of Singularity

4.3.1.1 Singularity when Estimating Local Angle of Attack α_e

As discussed in Section 4.2.2.2, it was found that a singular point occurred at the target angle of attack $\alpha_{target} = 0[\text{deg.}]$ when estimating local angle of attack α_e by the theoretical pressure distribution. This is not caused from the wind tunnel estimation. In order to investigate the cause, we consider an algorithm that estimates local angle of attack α_e . As mentioned in section 3.2.2, the quadratic equation (equation 54) is solved to estimate the local angle of attack α_e .

$$A \tan^2 \alpha_e - 1 + 2B \tan \alpha_e = 0 \quad (54)$$

$$\text{where } A = \Gamma_{ji} \sin^2 \lambda_k + \Gamma_{kj} \sin^2 \lambda_i + \Gamma_{ik} \sin^2 \lambda_j$$

$$B = \Gamma_{ji} \cos \phi_k \cos \lambda_k \sin \lambda_i + \Gamma_{kj} \cos \phi_i \cos \lambda_i \sin \lambda_j \\ + \Gamma_{ik} \cos \phi_j \cos \lambda_j \sin \lambda_k$$

In this case, the solution of the quadratic equation becomes the following equation 55. This equation is not valid for the cases, if the denominator A becomes zero, which causes a singular point. Also, there is a case when A is not zero and B is zero, still the solution cannot be estimated.

$$\alpha_e = \tan^{-1} \left(\frac{-B \pm \sqrt{B^2 - A^2}}{A} \right) \quad (55)$$

Looking at the value of A for the target angle of attack $\alpha_{target} = 0[\text{deg.}]$, as shown in Table 15, the values of A for the combinations 1 and 4 are zero (Red).

Table 15 – Value of A when estimating local angle of attack α_e

($\beta_{target} = 0[\text{deg.}]$, $M=0.5$)

$\alpha_{target}[\text{deg.}]$	Pressure Port Combinations			
	1	2	3	4
-2	-0.7724	-0.7707	-2.1118	-2.1101
-1	-0.3865	-0.3874	-1.0551	-1.0560
0	0.0000	0.0008	0.0008	0.0000
1	0.3865	0.3859	1.0566	1.0560
2	0.7724	0.7734	2.1091	2.1101

The reason is when looking at the pressure hole calculation value by the theoretical pressure distribution, the same pressure value in the red occurred which is caused due to the values of the pressure measurement differences Γ_{ik} , Γ_{ji} , Γ_{kj} are zero. In addition, the pressure measurements calculated by the pressure hole numbers 2 and 4 for the target Sideslip angle $\beta_{target} = 0[\text{deg.}]$ are all the same value (green letters) in Table 16. This is because in case of the target angle of attack $\alpha_{target} = 0[\text{deg.}]$, the geometric distances from the pressure hole number 3 which has the maximum pressure is same for the pressure hole numbers 1 and 5, therefore the same pressure value is obtained. This is because there is no influence due to the strategic

selection of the pressure hole for the local angle of attack α_e estimation; however the local Sideslip angle β_e has significant influence on the estimation.

In the estimation result by the wind tunnel test, the singularities do not occur as mentioned in the earlier case when estimating of local angle of attack α_e . This is because in the wind tunnel test, since the measured value of the pressure includes the measurement error, the difference of the pressure value is rarely zero, and it is considered that the singular point did not occur.

Table 16 – Calculated pressure measurement by the theoretical pressure distribution [kPa] ($M = 0.5$)

α_{target} [deg.]		Pressure Port Combinations					
β_{target} [deg.]		1	2	3	4	5	6
-2	0	255.05	249.26	271.38	249.26	243.52	178.91
-1	0	252.43	249.54	271.69	249.54	246.66	184.06
0	0	249.63	249.63	271.79	249.63	249.63	189.10
1	0	246.66	249.54	271.69	249.54	252.43	194.05
2	0	243.52	249.26	271.38	249.26	255.05	198.89

Therefore, for the estimation of the local angle of attack α_e using the FADS system, a singular point occurs in the combination of the pressure holes shown in Figure 53 for target angle of attack $\alpha_{target} = 0$ [deg.]. The cause of which is caused by the geometric arrangement of the pressure holes.

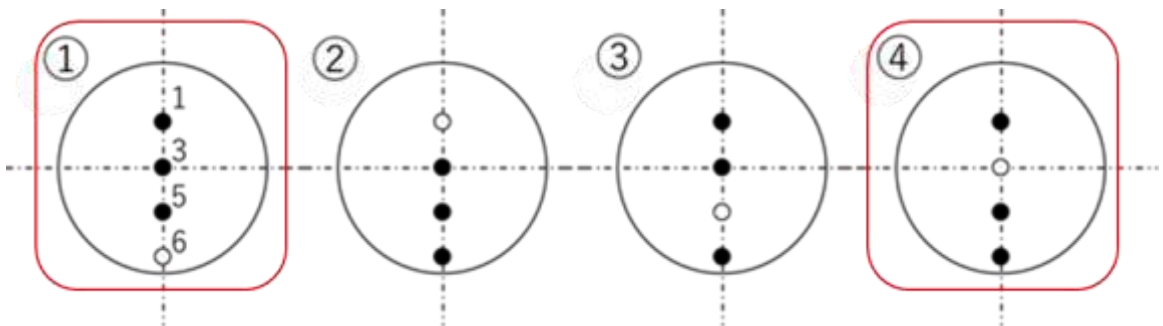


Figure 53 – Combination of pressure holes where singularity point occurs

4.3.1.2 Singularity when Estimating Local angle of attack β_e

As shown in Table 14, the occurrence of singular points for local slip angle β_e by the theoretical pressure distribution is discussed. Here, similar to the estimation result of the local angle of attack α_e , it is necessary to investigate the cause the singularity occurrence generated from the expression used for estimating the local sideslip angle β_e . The equation used to estimate the local sideslip angle β_e is the following equation 56.

$$A' \tan^2 \beta_e + 2B' \tan \beta_e + C' = 0 \quad (56)$$

$$\text{where } A' = \Gamma_{ik} \sin \phi_j \sin \lambda_j^2 + \Gamma_{ji} \sin \phi_k \sin \lambda_k^2 + \Gamma_{kj} \sin \phi_i \sin \lambda_i^2$$

$$B' = \left\{ \begin{array}{l} \Gamma_{ik} (\cos \alpha_e \cos \lambda_j + \sin \alpha_e \cos \phi_j \sin \lambda_j) (\sin \phi_j \sin \lambda_j) \\ + \Gamma_{ji} (\cos \alpha_e \cos \lambda_k + \sin \alpha_e \cos \phi_k \sin \lambda_k) (\sin \phi_k \sin \lambda_k) \\ + \Gamma_{kj} (\cos \alpha_e \cos \lambda_i + \sin \alpha_e \cos \phi_i \sin \lambda_i) (\sin \phi_i \sin \lambda_i) \end{array} \right\}$$

$$C' = \left\{ \begin{array}{l} \Gamma_{ik} (\cos \alpha_e \cos \lambda_j + \sin \alpha_e \cos \phi_j \sin \lambda_j)^2 \\ + \Gamma_{ji} (\cos \alpha_e \cos \lambda_k + \sin \alpha_e \cos \phi_k \sin \lambda_k)^2 \\ + \Gamma_{kj} (\cos \alpha_e \cos \lambda_i + \sin \alpha_e \cos \phi_i \sin \lambda_i)^2 \end{array} \right\}$$

In this case, the local sideslip angle β_e is estimated by solving the quadratic equation as shown in equation 56 and 57. Conditions shown in

Table 17 exist as conditions for generating singular points. When A' is zero , singularity points will arise in the algorithm.

$$\beta_e = \tan^{-1} \left(\frac{-B' \pm \sqrt{B'^2 - A'C'}}{A'} \right) \quad (57)$$

Table 17 – Conditions when singularity points occur

For A'	For B'	For C'	Computability
A' = 0	B' = 0	C' = 0	No
		C' ≠ 0	No
	B' ≠ 0	C' = 0	No
		C' ≠ 0	Yes
A' ≠ 0	B' = 0	C' = 0	No
		C' ≠ 0	Yes
	B' ≠ 0	C' = 0	Yes
		C' ≠ 0	Yes

Table 18 shows the values of A' when estimating the local sideslip angle β_e . Actually, the values of A' for the combinations C and D for the target angle of attack $\alpha_{target} = 7[\text{deg.}]$ and $8[\text{deg.}]$ are very close to zero (Red letters). In addition, A' for the combinations A, B and E is zero (green letters), and due to this influence, the singularity is occurs for all the target sideslip angle when $\beta_{target} = 0[\text{deg.}]$.

Furthermore, looking at the values of A' for the combinations F and G for the target angle of attack $\alpha_{target} = 15[\text{deg.}]$, we see that A' is zero (Blue).

Table 18 – Value of A' when estimating local sideslip angle β_e

($\beta_{target} = 0[\text{deg.}]$, $M=0.5$)

$\alpha_{target}[\text{deg.}]$	Pressure Port Combinations						
	A	B	C	D	E	F	G
6	0.000	0.000	0.300	0.300	0.000	3.423	3.423
7	0.000	0.000	0.100	0.100	0.000	3.054	3.054
8	0.000	0.000	-0.100	-0.100	0.000	2.679	2.679
9	0.000	0.000	-0.300	-0.300	0.000	2.303	2.303
10	0.000	0.000	-0.500	-0.500	0.000	1.923	1.923
11	0.000	0.000	-0.222	-0.222	0.000	0.491	0.490
12	0.000	0.000	-0.285	-0.285	0.000	0.368	0.368
13	0.000	0.000	-1.904	-1.904	0.000	0.772	0.772
14	0.000	0.000	-1.290	-1.290	0.000	0.387	0.387
15	0.000	0.000	-1.484	-1.484	0.000	0.000	0.000

16	0.000	0.000	-1.677	-1.677	0.000	-0.387	-0.387
17	0.000	0.000	-1.866	-1.866	0.000	-0.772	-0.772

The pressure values calculated for each pressure hole are shown in Table 19. In particular, the pressure values obtained are near or equal to the pressure hole numbers 3 and 5 (red letters) used for the combinations C and D and the pressure hole numbers 3 and 6 (blue letters) used for the combination F and G, A' becomes a value very close to zero or zero, indicating that a singular point is generated.

Also, under the condition of the target Sideslip angle $\beta_{target} = 0[\text{deg.}]$, the acquired pressure value for the pressure hole numbers 2 and 4 is the same for all target angle of attack α_{target} (green letters). The commonly used pressure hole for combinations A, B and E (Figure 54) is the cause, and singularities occur for the combinations A, B and E under all conditions with the target sideslip angle $\beta_{target} = 0[\text{deg.}]$.

Table 19 – Calculated pressure measurement by the theoretical pressure distribution [kPa] ($M = 0.5$)

α_{target} [deg.]	β_{target} [deg.]	Pressure Port Combinations					
		1	2	3	4	5	6
6	0	158.01	163.40	170.36	163.40	168.94	154.12
7	0	156.76	163.01	169.95	163.01	169.47	155.46
8	0	155.46	162.57	169.47	162.57	169.95	156.76
9	0	154.12	162.07	168.94	162.07	170.36	158.01
10	0	152.74	161.51	168.34	161.51	170.71	159.21
11	0	151.31	160.90	167.68	160.90	171.00	160.37
12	0	149.84	160.23	166.96	160.23	171.22	161.47
13	0	148.34	159.50	166.19	159.50	171.38	162.52
14	0	146.80	158.73	165.36	158.73	171.48	163.52
15	0	145.23	157.90	164.47	157.90	171.51	164.47
16	0	143.63	157.02	163.52	157.02	171.48	165.36
17	0	141.99	156.08	162.52	156.08	171.38	166.19

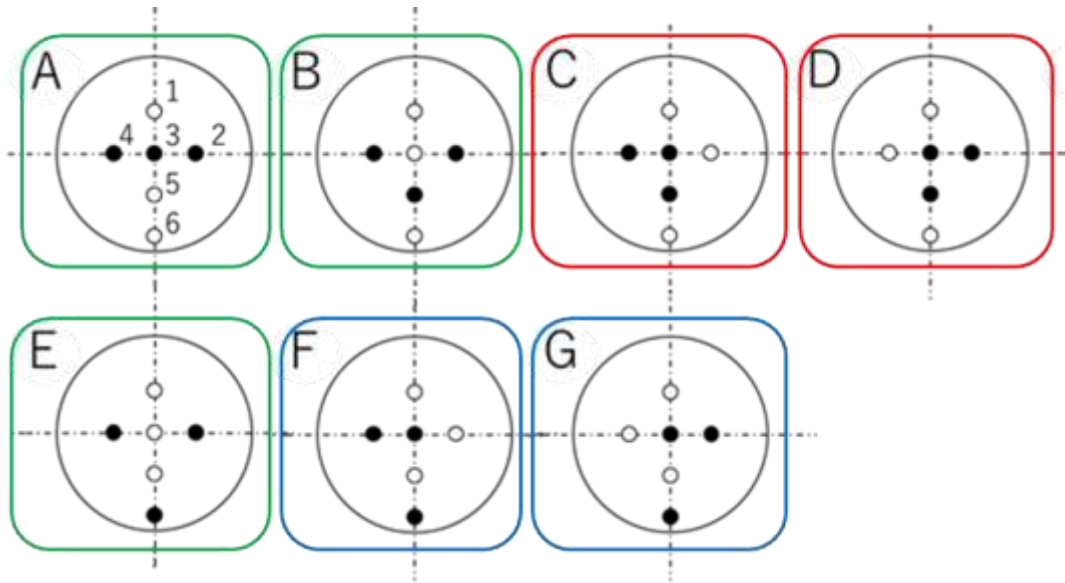


Figure 54 – Combination of pressure holes where singularity point occurs

Figure 54 shows the combination of pressure holes where singularities occur when estimating the local sideslip angle β_e . Color coding is same as the Table 18. For both the estimation of the local angle of attack α_e and local sideslip angle β_e , when the pressure values are the same among the combinations of pressure holes used for estimation, singularity occurs. It was also found that even when the difference in pressure value is very small like the combinations C and D, a singular point which produces a large error in the estimation result. Therefore, from the theoretical point of view, all the combinations of the pressure holes used for the local Sideslip angle β_e have angular conditions that fall into singular points.

4.3.2 Measures for Singularity

From this Chapter 4, it is understood that if the acquired pressure measurement becomes same or close value due to the geometrical relationship of the pressure hole, singularity points occur. In order to avoid the occurrence of singularities^[20, 21, 22], it may be considered not to use combinations that are peculiar

depending on the angle of attack and the sideslip angle of the vehicle, however considering that the FADS system for WIRES vehicle will actually be used for various Mach numbers, angles of attack and sideslip angles, so it is impossible to neglect this singularity issue. Particularly for the estimation of the local sideslip angle β_e , there are lot of conditions that fall into singularity, and in addition to the conditions described in this research, there can also be conditions not described here.

Therefore, the following points are cited as measures for singularities of the winged experimental rocket.

1. A threshold value should be set for the values of A and A', and when it approaches zero, the result estimated using the combination of the pressure holes is removed from the final average operation.
2. Since there are four combinations for local angle of attack α_e and seven combinations of pressure holes for the local sideslip angle β_e , the estimation result is determined by majority decision and the singularity is removed from the final average operation.
3. Select a combination of pressure holes to be used according to the attitude condition.

CHAPTER 5. FAULT TOLERANCE CAPABILITY AND RESULTS

5.1 Concept of Fault Tolerance Capability

After thorough analysis mentioned in the previous chapter, it is understood that the singularity is the cause of the deterioration of the accuracy when estimating the sideslip angle at higher angle of attack. Using the necessary modifications in the previous chapter, the singularity issue can be resolved and achieve accuracy. However, we still have the problems arising during the high temperature supersonic and hypersonic flights where the pressure ports or sensors still have a high risk of failure that makes the acquisition of the air data unreliable, to result in loss of flight controllability. In parallel to FADS estimation and implementation algorithm for reusable space transportation vehicle, it is necessary to introduce fault tolerance capability^[23, 24] to the system to be “fail-operational”.

For a system to be fault tolerant,

- First, the fault in the system must be detected
- Second, the cause of the fault must be identified and
- Third, the fault must be isolated (in other words tolerance)

To overcome these issues, selection of appropriate ports and increasing the number of ports from 6 to 9 (in Figure 55) from the 17 available ports for the estimation is one of the suitable solutions for fault tolerance. Therefore, for angle of attack estimation 10 combinations of pressure ports and for sideslip angle estimation 55 combinations can be employed in the algorithm. When the port combinations are

increased, there is a wide selection of combinations for various attitudes of the flight to eliminate the combinations that cause the singularity and if any of pressure sensors or ports fails during the re-entry, the faulty ports or sensors can be detected using the change detection criteria (in Figure 56) and weighted out of the algorithm. This weighting-out allows up to maximum 2 pressure sensor failures to be weighted out of the algorithm while still estimating the air data parameters such as angle of attack, sideslip angle, Mach number, static pressure, and impact pressure.

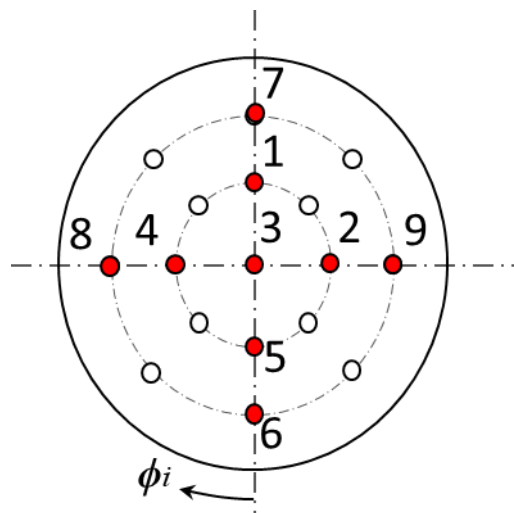


Figure 55 – Port combinations for fault tolerance

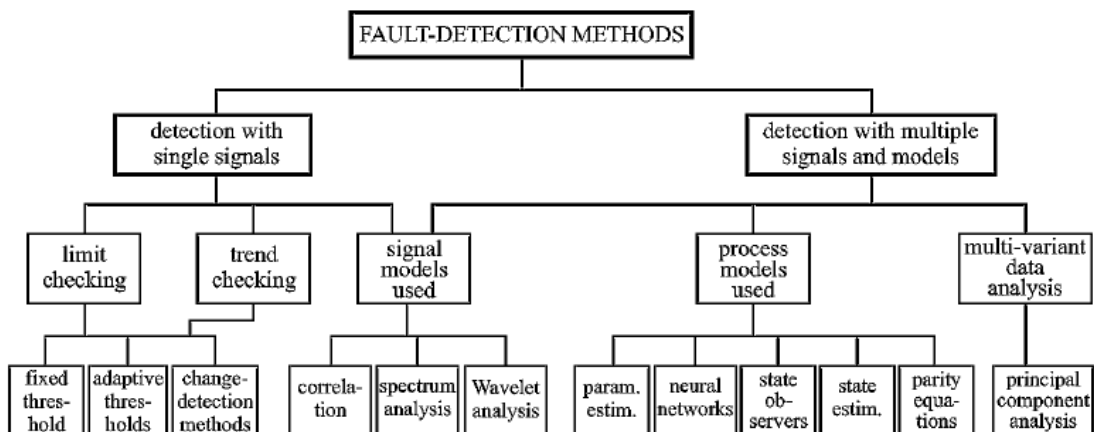


Figure 56 – Various fault detection methods for single and multiple signals

5.2 Fault Detection and Isolation Scheme

5.2.1 Fault Detection and Isolation for Pressure Ports

To identify the faults of a pressure sensor, which occur in the form of failure of a pressure sensor or leakage in the pipe connecting the measurement hole on the vehicle surface to the sensors is by employing the change detection criteria during the on-board estimation method. Using the NASA's algorithm, Mach number estimates can be derived from the impact pressure and dynamic pressure (q_c and P_∞) using equations 39, 40, 41, 44 and 45.

$$M_j = \begin{bmatrix} \cos^2\theta_1 + \varepsilon^j \sin^2\theta_1 & 1 \\ \vdots & \vdots \\ \cos^2\theta_{17} + \varepsilon^j \sin^2\theta_{17} & 1 \end{bmatrix} \quad (58)$$

$$Q = \begin{bmatrix} q_1 & 0 & 0 & 0 & 0 & 0 \\ 0 & q_2 & 0 & 0 & 0 & 0 \\ 0 & 0 & \ddots & 0 & 0 & 0 \\ 0 & 0 & 0 & \ddots & 0 & 0 \\ 0 & 0 & 0 & 0 & q_{16} & 0 \\ 0 & 0 & 0 & 0 & 0 & q_{17} \end{bmatrix} \quad (59)$$

$$\begin{bmatrix} \hat{q}_c \\ \hat{P}_\infty \end{bmatrix}_{j+1} = \begin{bmatrix} M_{(j)}^T Q M_{(j)}^{-1} & M_{(j)}^T Q \end{bmatrix} \begin{bmatrix} P_1 \\ \vdots \\ P_{17} \end{bmatrix} \quad (60)$$

$$M_\infty = \sqrt{\frac{2}{\gamma-1} \left\{ \left(\frac{q_c}{P_\infty} + 1 \right)^{\frac{\gamma-1}{\gamma}} - 1 \right\}} \quad (61)$$

$$\begin{aligned}
\frac{P_{02}}{P_{\infty}} &= \frac{P_{02}}{P_{01}} \frac{P_{01}}{P_{\infty}} \\
&= \left\{ \left(\frac{\gamma+1}{\gamma-1} \frac{M_{\infty}^2}{M_{\infty}^2+2} \right) \left(1 + \frac{\gamma-1}{2} M_{\infty}^2 \right) \right\}^{\frac{\gamma}{\gamma-1}} \times \left(\frac{\gamma+1}{2\gamma M_{\infty}^2 - \gamma - 1} \right)^{\frac{1}{\gamma-1}} \\
&= \left(\frac{\gamma+1}{2} \frac{M_{\infty}^2}{M_{\infty}^2+2} \right)^{\frac{\gamma}{\gamma-1}} \left(\frac{\gamma+1}{2\gamma M_{\infty}^2 - \gamma - 1} \right)^{\frac{1}{\gamma-1}}
\end{aligned} \tag{62}$$

In this method, multiple iterations of Mach number estimates M_e are calculated for various Q matrices (in equation 40) where weight of each sensor $q_1 \sim q_{17}$ are set to zero assumes that particular sensor has failed as shown in Figure 57.

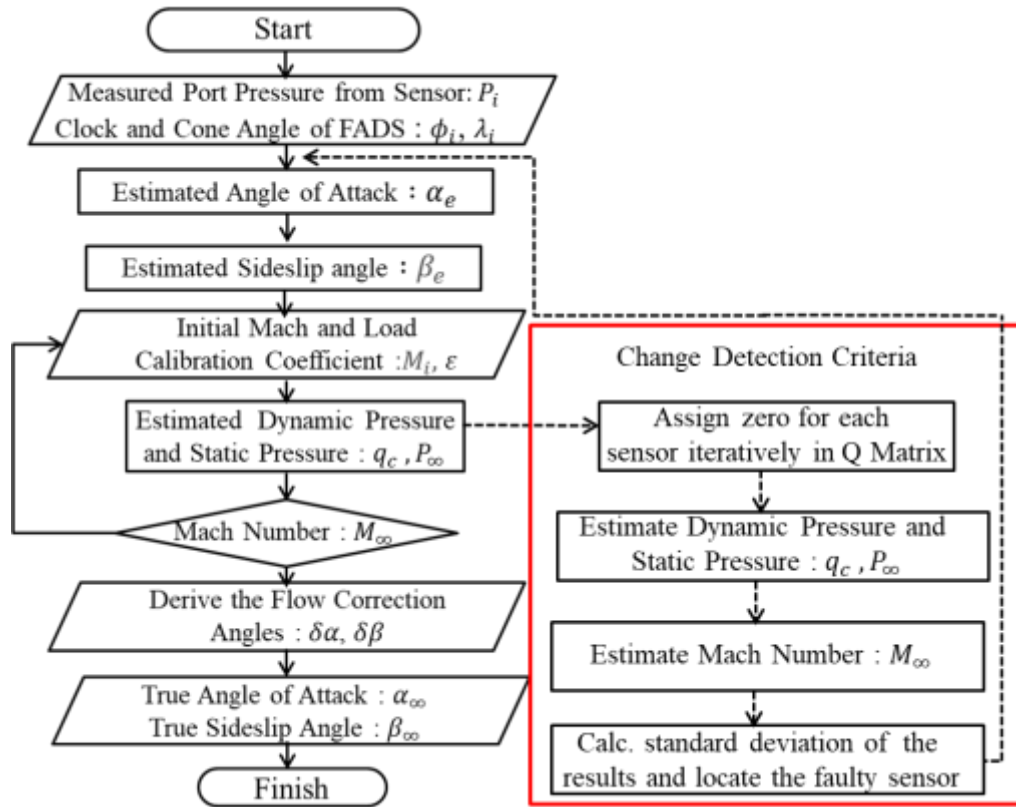


Figure 57 – Change detection method for identifying the pressure sensor faults

When a non-faulty sensor is set to zero estimated Mach number will have the equal error for all cases. However, when the faulty sensor value is set to zero, the

Mach number estimates deviates from the other estimates. Fault detection examples for case when one sensor failed i.e. port 6 (in Figure 58) and two sensors failed i.e. port 6 and 8 (in Figure 59).

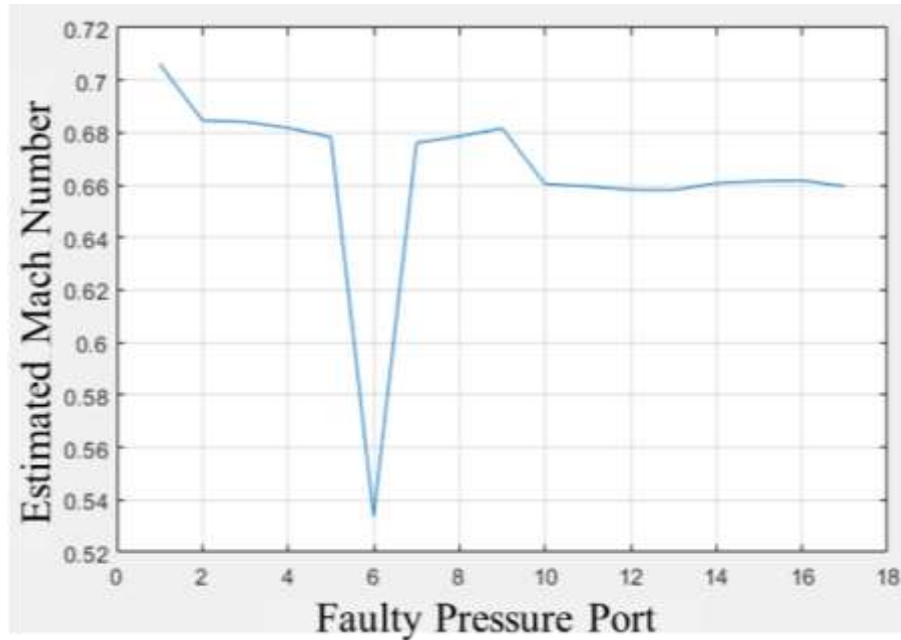


Figure 58 – Fault detection case for one sensor failure (port 6)

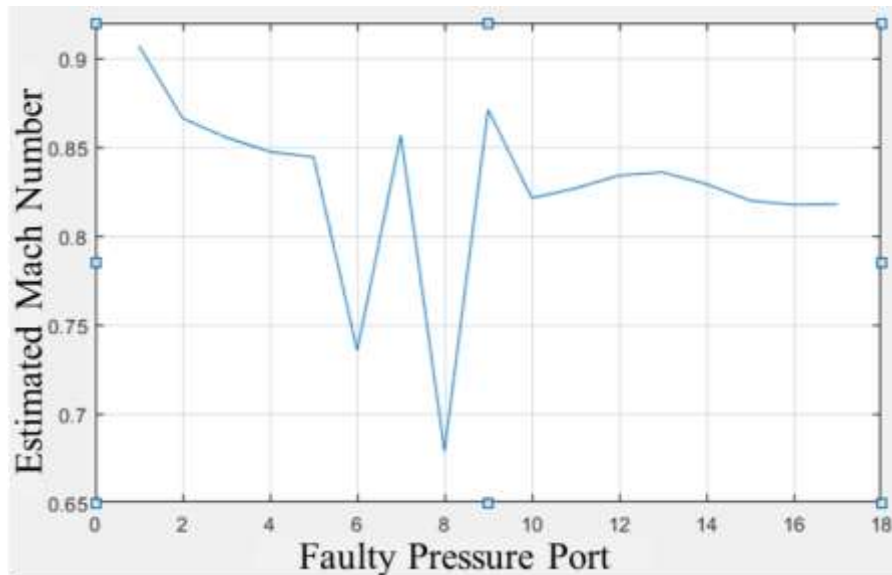


Figure 59 – Fault detection case for two sensors failure (port 6 and 8)

Applying the standard deviation method (in equation 58) to the estimates of the Mach number, the faulty sensors can be identified and eliminated from the combinations for estimating the angle of attack and sideslip angle.

$$\mu(M_e) - \sigma(M_e) < M_e < \mu(M_e) + \sigma(M_e) \quad (63)$$

5.2.2 Fault Detection and Isolation in Estimation of Angle of Attack

Using the same concept mentioned in Chapter 3.2, the estimation of angle of attack α_e can be decoupled from sideslip angle β_e by using only pressures aligned along a vertical meridian (where $\phi = 0^\circ$ or 180° shown in Figure 31 and Table 7). In this geometry arrangement, terms related to sideslip angle β_e are eliminated from equation 26. The result is a quadratic expression in $\tan(\alpha_e)$ of the form shown in equation 30. The output angle of attack is determined as the mean of the values computed using the ten individual triples (in Figure 60) as shown in equation 31.

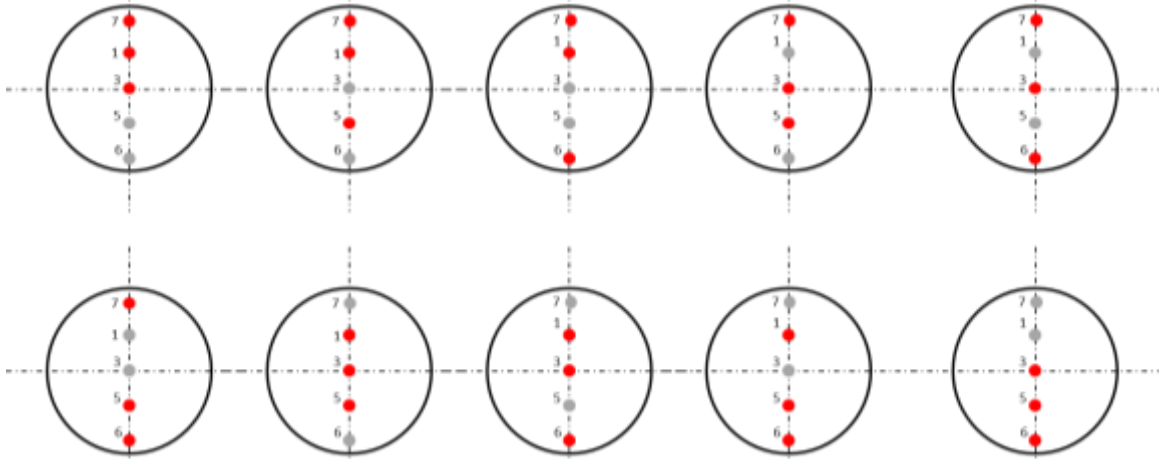


Figure 60 – Pressure port combination for angle of attack estimation with fault tolerance

$$A(\tan^2 \alpha_e - 1) + 2B\tan\alpha_e = 0 \quad (64)$$

$$\alpha_e = \frac{1}{n} \sum_{x=1}^n \alpha_{e_{(i,j,k)_x}} \left[P_{\{i,j,k\}}, \lambda_{\{i,j,k\}}, \phi_{\{i,j,k\}} \right] \Big|_{n=10} \quad (65)$$

First, the triples equation mentioned in equation 25 will be made sure that the singularity issue mentioned in previous chapter is eliminated. Then the averaging procedure provides the estimate of the local angle of attack. In this procedure, this averaging method provides a measure of noise rejection for the estimator. Clearly, if one of the ports along the vertical meridian is deemed unusable due to the pressure sensor failure and it is weighted out of the algorithm using the standard deviation method. If 5 ports on the vertical meridian are employed for the estimation, we have 10 possible combinations, then four valid triple remains for computing the angle of attack. If two sensors are failed, then one valid triple remains for the computing the angle of attack. The failed sensors are detected and isolated from the estimation algorithm.

5.2.3 *Fault Detection and Isolation in Estimation of sideslip angle*

Similarly for sideslip angle, the number of ports is increased from 5 to 9 considering all the ports on the vertical and horizontal meridian which give us 55 triple combinations. These combinations will improve the accuracy from the previous method and can be suitable for at least up to two sensor failures, considering the angle of attack limitation (due to the number of ports used for the estimation are only 5 ports). The same logic applied in the previous section will be employed for the estimation of the sideslip angle.

5.3 **Formula to Calculate the Number Ports for Estimation with Failure**

5.3.1 *Ports Required for Calculating Angle of Attack with Failure*

The limiting factor for the number of vertical ports is angle of attack. To calculate at least one combination of three verticals ports are used. This can be represented by

$$Number_{combination} (Angle\ of\ Attack) = \frac{N_{vertical}!}{(N_{vertical}-3)!3!}.$$

The minimum number of combination needed is one, therefore:

$$1 = \frac{N_{vertical}!}{(N_{vertical} - 3)! 3!}$$

This implies that $N_{vertical} = 3$. But it is important to notice that $N_{vertical}$ corresponds to all the working port.

$$N_{vertical} = N_{All\ vertical} - N_{vertical\ failure}$$

This gives us immediately the number of vertical port needed if the number of failures acceptable is known:

$$N_{All\ vertical} = 3 + N_{vertical\ failure}$$

5.3.2 Ports Required for Calculating Sideslip Angle with Failure

The limiting factor for the number of horizontal ports is sideslip angle. To calculate this at least one combination of three verticals/horizontal ports are used. However if only vertical holes are used the values given are erroneous as a consequence these combinations are removed. Giving us

$$\begin{aligned} &Number_{combination} (Sideslip\ angle) \\ &= \frac{(N_{vertical} + N_{horizontal})!}{(N_{vertical} + N_{horizontal} - 3)! 3!} - \frac{N_{vertical}!}{(N_{vertical} - 3)! 3!} \end{aligned}$$

The minimum number of combination needed is one, therefore:

$$1 = \frac{(N_{vertical} + N_{horizontal})!}{(N_{vertical} + N_{horizontal} - 3)! 3!} - \frac{N_{vertical}!}{(N_{vertical} - 3)! 3!}$$

Solving this equation is the same that to solve a third order polynomial in $N_{horizontal}$.

After that as previously mentioned for angle of attack the equation becomes:

$$N_{All\ horizontal} = N_{horizontal} + N_{horizontal\ failure}$$

It is not necessary to “solve” the polynomial equation because we just need the real solution. The polynomial equation is rewritten as follow:

$$A * N^3 + AD * N^2 + C * N = 1$$

$$\text{Then } (A \ B \ C) \begin{pmatrix} N^3 \\ N^2 \\ N \end{pmatrix} = 1 \Rightarrow \begin{pmatrix} N^3 \\ N^2 \\ N \end{pmatrix} = ((A \ B \ C)^T (A \ B \ C))^{-1} (A \ B \ C)$$

Where only N (Combinations for sideslip angle) are needed.

5.4 Simulation Conditions of the Fault Tolerant Flush Air data Algorithm

The FADS estimation algorithm has been updated with the following improvements and conditions:

- Increasing the number of ports from 6 to 9
- Eliminating the cases with singularity

Employing fault tolerance capability for pressure sensor failure and leakage (degradation of pressure value obtained from wind tunnel to 5, 10, 20 and 50 %) with the following cases.

Case 1: One sensor on the vertical meridian,

Case 2: Two sensor on the vertical meridian,

Case 3: One sensor on vertical and one on horizontal meridian

5.5 Results of the Fault Tolerant Flush Air data Sensing Algorithm

5.5.1 Estimation Results for One Sensor Failure on Vertical Meridian for Mach Number 0.8

The calibrated angle of attack and sideslip angle estimates for $M=0.8$ are shown in Figure 61. The angle of attack estimates are relatively accurate with respect to the wind tunnel reference data. The sideslip angle estimates on the other hand are in the deviation range of less than 0.5 [deg.] with respect to the wind tunnel reference data. The accuracy of the sideslip estimates however was improved compared with the estimates in Figure 35 and for higher sideslip angles the deviation from the reference value was minimal. The Mach number estimates for $M=0.8$ (in Figure 62) are in the deviation range of less than 0.02 which is far better than the NASA's X-33 results. Here, the fault detection algorithm detects the leakage and weighted out of the algorithm for all the cases but could not detect the leakage at 5%, thus the estimated angle of attack value has error. The error impact in estimating the angle of attack deteriorated the sideslip angle estimation at 5% error.

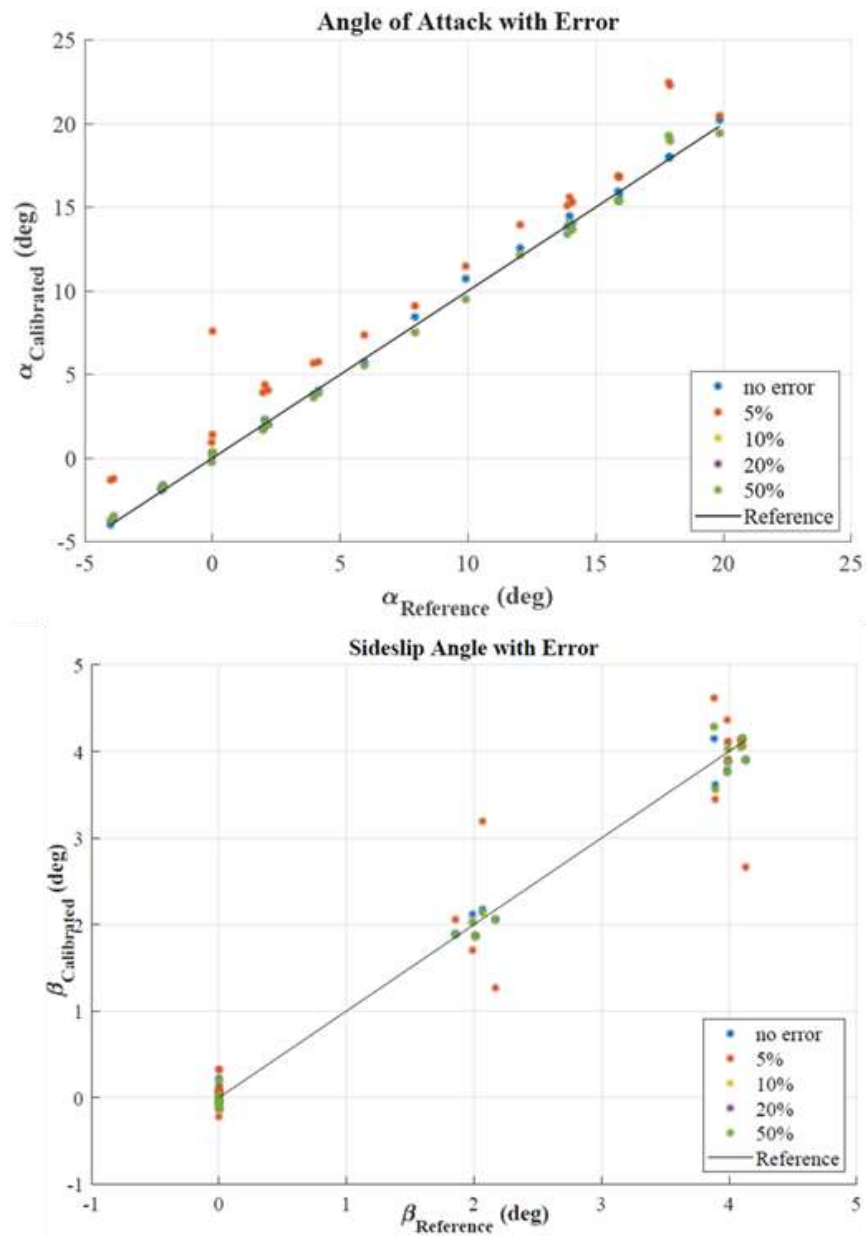


Figure 61 – Calibrated angle of attack and sideslip angle estimation results for M=0.8 (case 1)

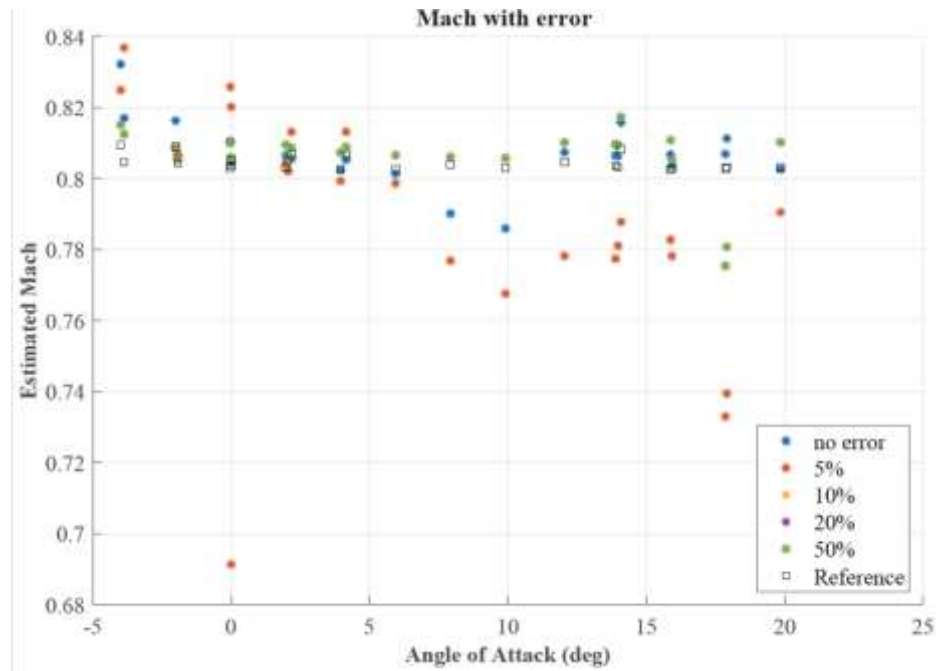


Figure 62 – Mach estimation results for M=0.8 (case 1)

5.5.2 Estimation Results for One Sensor Failure on Vertical Meridian for Mach Number 1.0

The calibrated angle of attack and sideslip angle estimates for M=1.0 are shown in Figure 63. The angle of attack estimates are similar to that of the M=0.8 estimates with respect to the wind tunnel reference. Here, the fault detection algorithm detects the leakage and weighted out of the algorithm for all the cases but could not detect leakage at 5 and 10%, thus the estimated angle of attack value has error. The error impact in estimating the angle of attack deteriorated the sideslip angle estimation at 5 and 10 % error. The sideslip angle estimates are in the deviation range of less than 0.3 [deg.] with respect to the wind tunnel reference data. The Mach number estimates for M=1.0 (in Figure 64) are in the deviation range of less than 0.015. As the angle of attack increases, the estimation of Mach deteriorated.

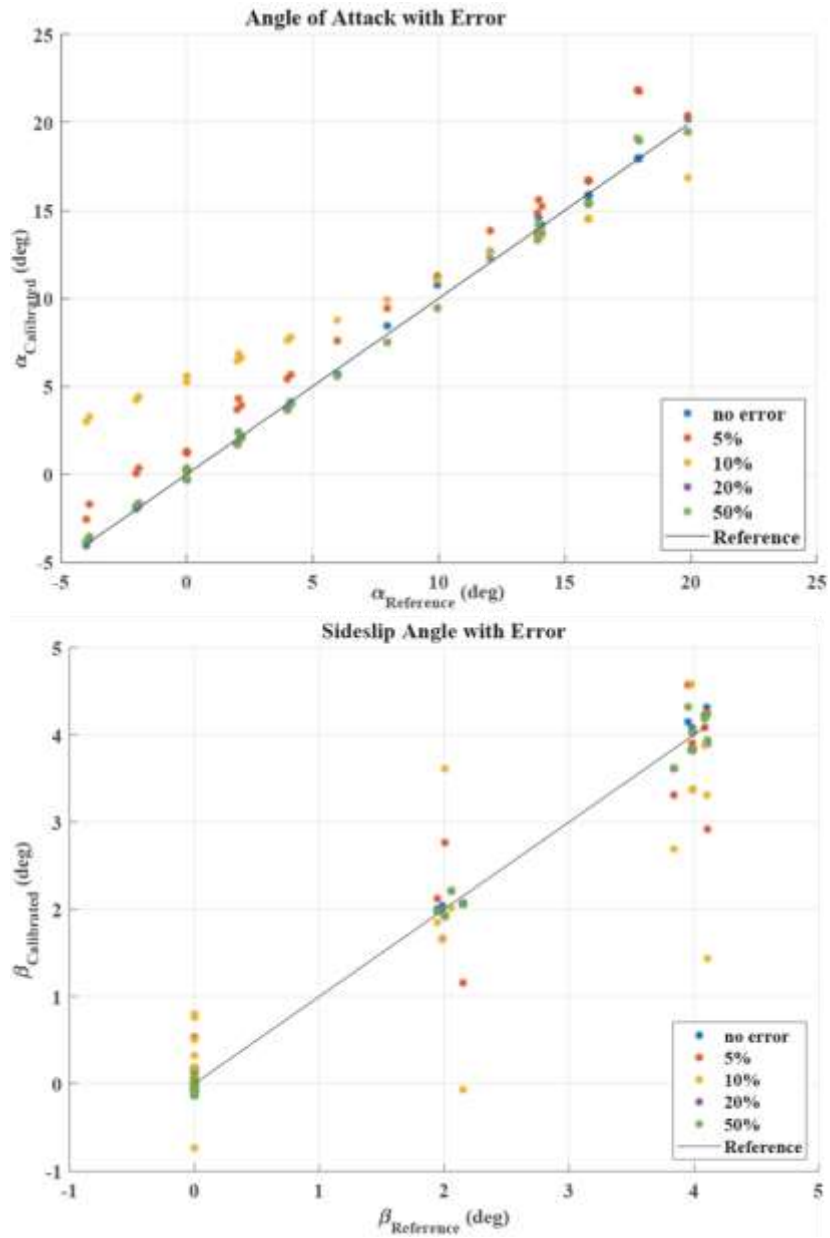


Figure 63 – Calibrated angle of attack and sideslip angle estimation results for M=1.0 (case 1)

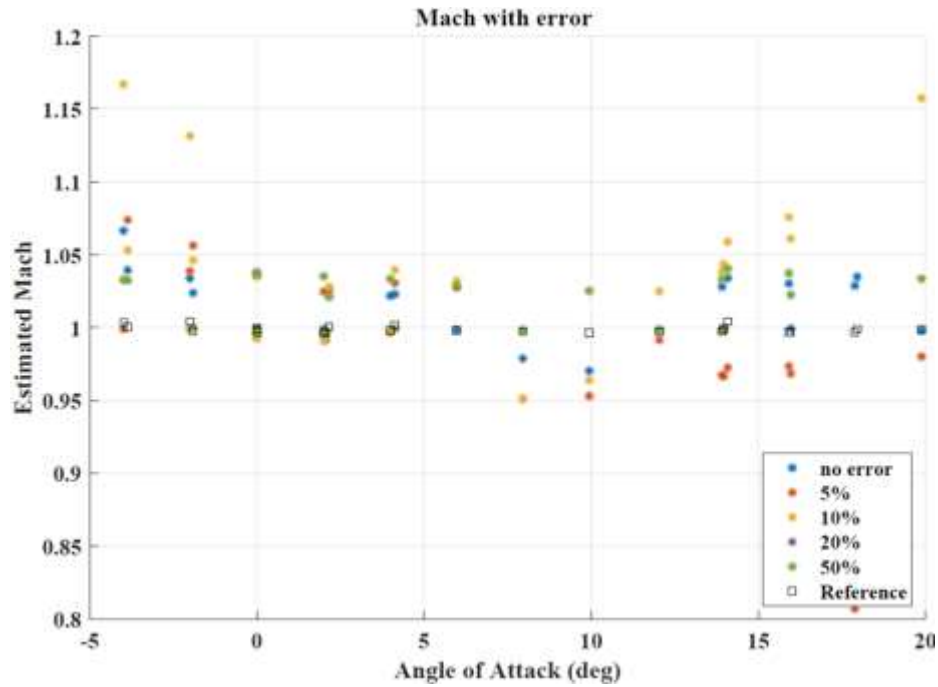


Figure 64 - Mach estimation results for M=1.0 (case 1)

5.5.3 Estimation Results for One Sensor Failure on Vertical Meridian for Mach Number 2.0

The calibrated angle of attack and sideslip angle estimates for M=2.0 are shown in Figure 65. The angle of attack estimates are relatively accurate with respect to the wind tunnel reference data. The sideslip angle estimates on the other hand are in the deviation range of less than 0.5[deg.] with respect to the wind tunnel reference data. Here, the fault detection algorithm detects leakage and weighted out of the algorithm for all the cases but could not detect leakage at 5%, however the estimation of angle of attack improved for Mach 2.0. The error impact in estimating the angle of attack, deteriorated the sideslip angle estimation at 5% error but the overall estimation improved for Mach 2.0 .However, the Mach number estimates for M=2.0 (in Figure 66) are not estimated with respect to the wind tunnel reference data and Mach number estimation at higher angle of attack deteriorated than the estimation at low angle of attack..

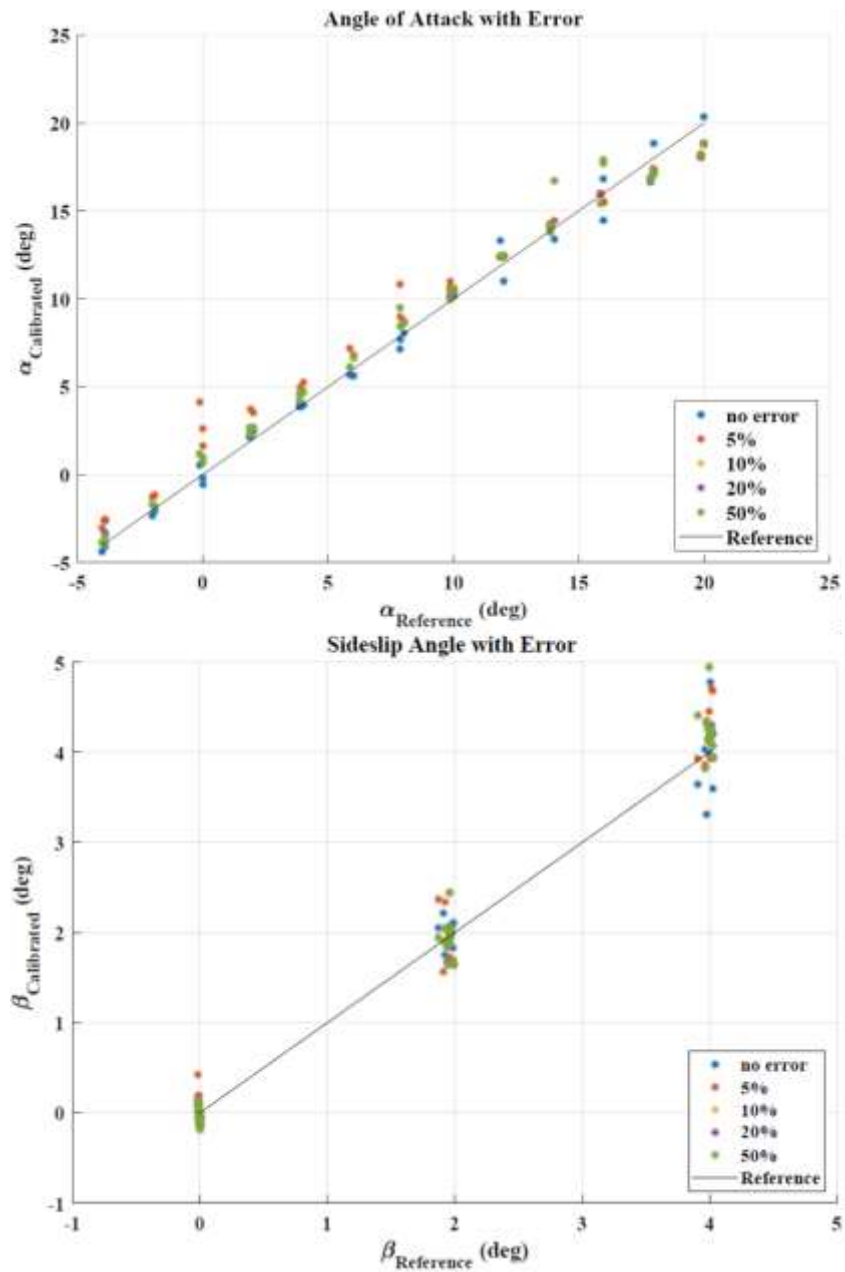


Figure 65 – Calibrated angle of attack and sideslip angle estimation results for M=2.0 (case 1)

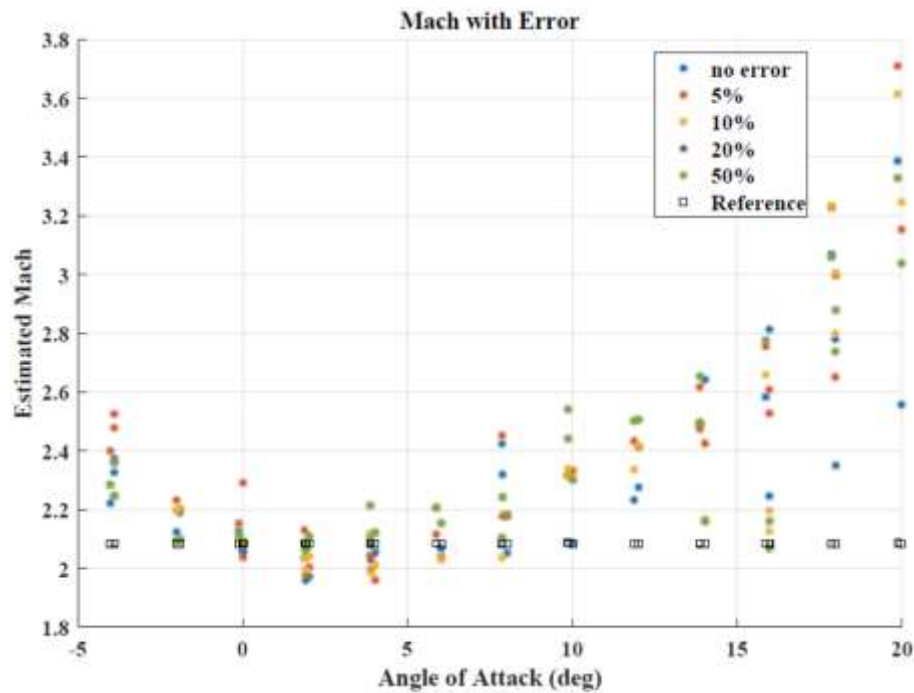


Figure 66 – Mach estimation results for M=2.0 (case 1)

5.5.4 Estimation Results for Two Sensor Failure on Vertical Meridian for Mach Number 0.8

The calibrated angle of attack and sideslip angle estimates for M=0.8 are shown in Figure 67. The angle of attack estimates have some dispersion with respect to the wind tunnel reference data and as the angle of attack increases the estimation deteriorates. The sideslip angle estimates on the other hand have large deviations with respect to wind tunnel data for sideslip angle from 0[deg.] to 4[deg.]. Here, the fault detection algorithm could not detect leakage for most of the cases except when the error is significantly higher. Also, when there is two sensors failure there is only one combination used for estimating the angle of attack. Since, the estimates of angle of attack and sideslip accuracy deteriorated, the Mach number estimates for M=0.8 (in Figure 68) also had the effect.

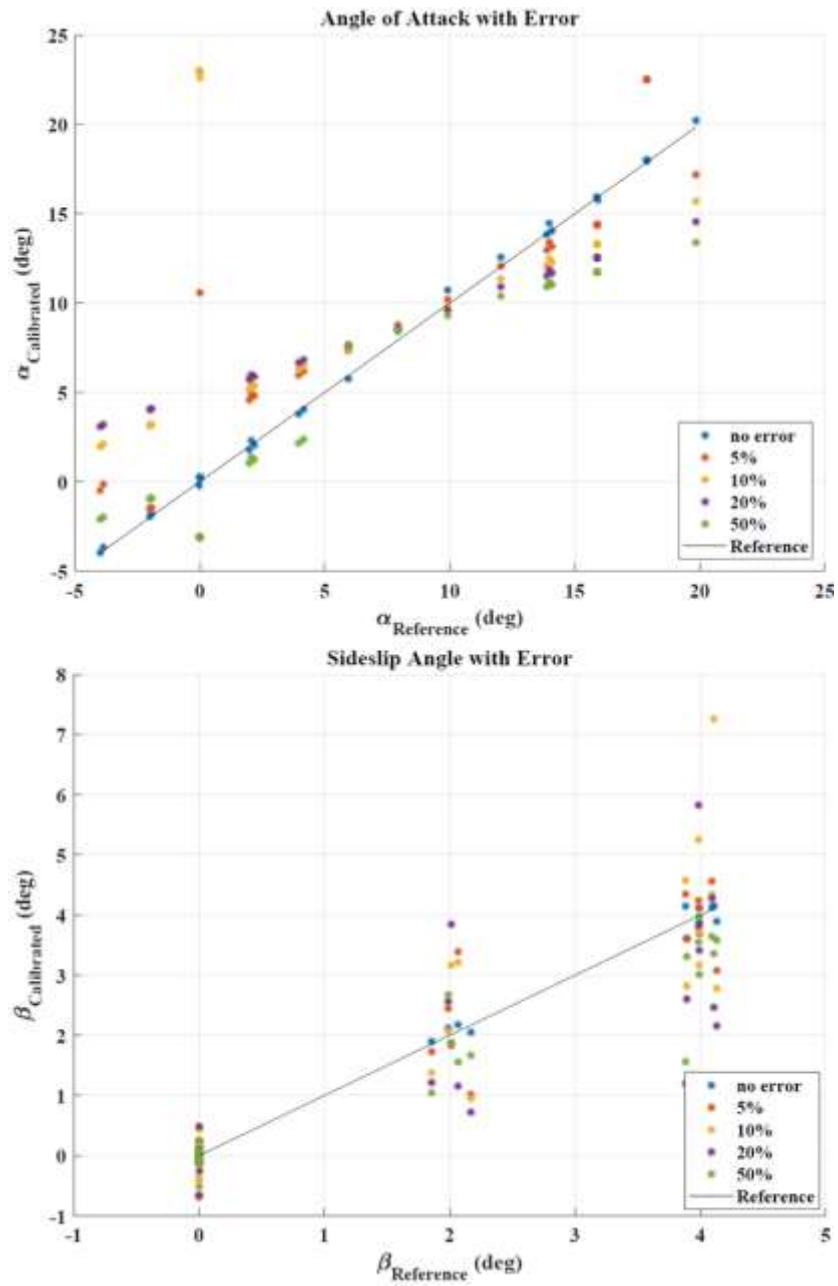


Figure 67 – Calibrated angle of attack and sideslip angle estimation results for M=0.8 (case 2)

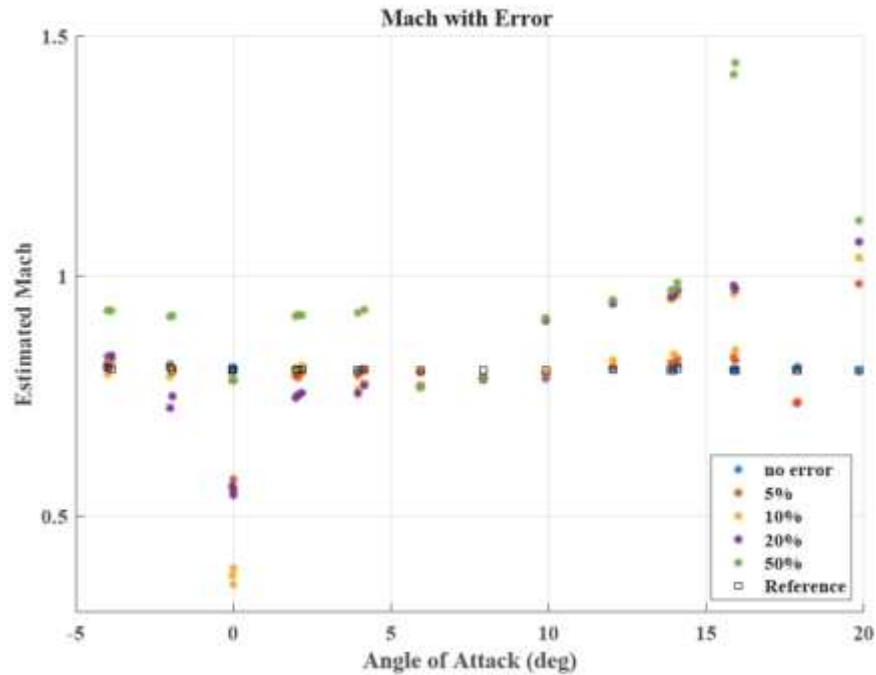


Figure 68 – Mach estimation results for M=0.8 (case 2)

5.5.5 Estimation Results for One Sensor Failure on Vertical Meridian and Horizontal Meridian for Mach Number 0.8

The calibrated angle of attack and sideslip angle estimates for M=0.8 are shown in Figure 69. The angle of attack estimates have similar dispersion as seen in case 2 for two sensor failure and as the angle of attack increases the estimation deteriorates. The sideslip angle estimates on the other hand have large deviations with respect to wind tunnel data for Sideslip angle from 0[deg.] to 4[deg.]. Since, the estimates of angle of attack and sideslip accuracy deteriorated the Mach number estimates for M=0.8 (in Figure 70) had the influence of angle of attack and sideslip angle.

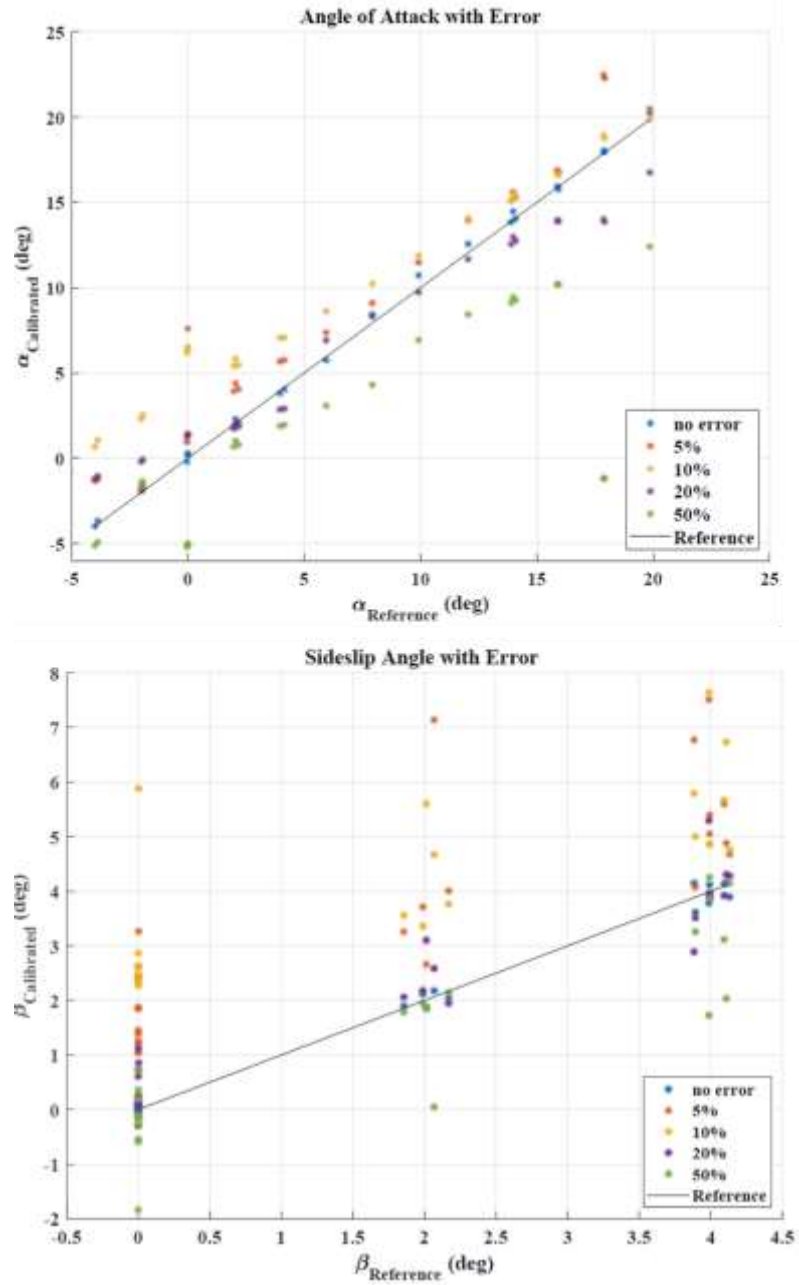


Figure 69 – Calibrated angle of attack and sideslip angle estimation results for M=0.8 (case 3)

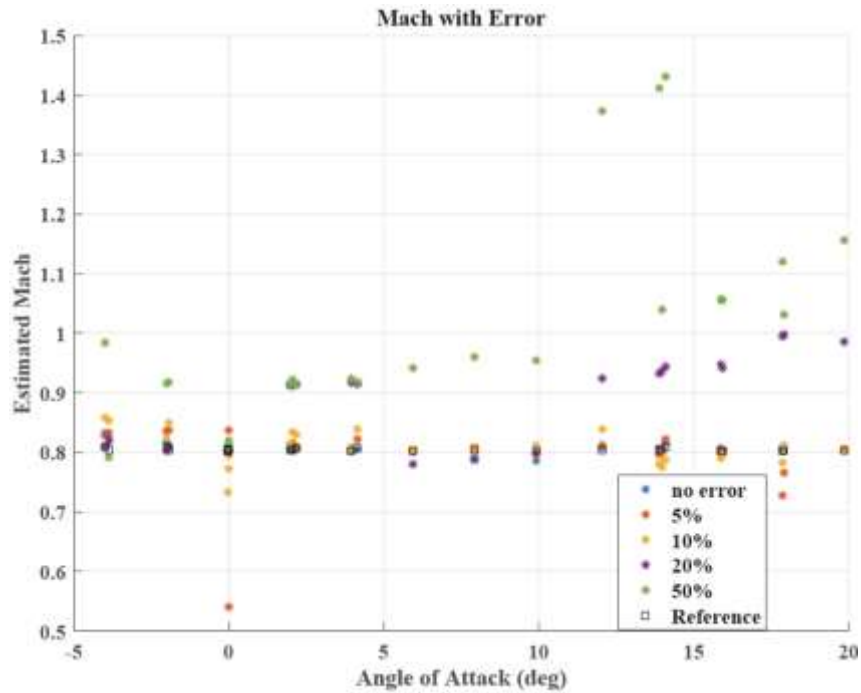


Figure 70 – Mach estimation results for M=0.8 (case 3)

5.6 Limitations for the Fault Tolerance FADS Algorithm

The fault detection technique employing “Change Detection Criteria” is not able to detect faults when the leakage is 5% as the leakage did not make any considerable difference to weight out of the algorithm. In some cases for the no leakage cases, the sensors data with no faults was also removed resulting in deterioration in the estimating results. For two sensor failure on vertical meridian case, there is only one combination left in the angle of attack estimation algorithm resulting in deteriorating the results. For one sensor failure on vertical meridian and one sensor failure on horizontal meridian, improvement is necessary to isolate the leakage as the standard deviation could not isolate the failed sensors. However the singularity issue was removed from the algorithm but improvement is necessary in the fault detection technique for multiple sensor failure or when leakage is small.

CHAPTER 6. CONCLUSIONS

The fault tolerant flush air data sensing (FADS) system is derived as a synthesis of the incompressible potential flow around a sphere and modified Newtonian flow theory for a wide Mach range. The pressure model and its solution algorithm provide a method for extracting the entire air data parameters such as angle of attack, sideslip angle, Mach number, static pressure and impact pressure except true airspeed from flush surface pressure measurements. However, the true airspeed cannot be measured with this algorithm as the measurement or estimate of free-stream temperature is needed to calculate the speed of sound. The fault detection and isolation method proposed in this research can make the FADS system redundant for two pressure sensor failure. Additionally, the accuracy of the estimates has been improved by removing the singularity issue and increasing the number of pressure ports. This research uses the wind tunnel test data for the calibration of the FADS pressure model for flight configurations. The general structure of the calibration curves was consistent across the wide range of shapes, Mach numbers, and angles of attack that were tested.

Major finding and lessons learned from the algorithm are as follows:

- The pressure model adapted from the solution for potential flow over a sphere can be calibrated for a wide variety of blunt fore body shapes.
- The calibration parameters are composed of three terms: a shape and compressibility parameter ε , flow correction terms such as an up wash parameter $\delta\alpha$, and a side wash parameter $\delta\beta$. Using these three parameters, the pressure model is calibrated to equivalent levels of accuracy for each of

the data sources analysed. When plotted as a function of Mach number, angle of attack, and sideslip angle, the calibration parameters exhibited very similar characteristics.

- All three calibration parameters were found to be smooth, monotonic functions that are easily storable in a real-time system. At high Mach numbers, ε universally approached zero, which reduces the pressure model to modified Newtonian flow. Also, for Mach numbers greater than approximately 1.5, the variation in ε with angle of attack and sideslip angle is negligible.
- The angle of attack and sideslip angle calibration parameters $\delta\alpha$ and $\delta\beta$, are generally a function of angle of attack and Mach number. However, at high Mach numbers these values diminish to small, constant-bias values. This high Mach number result along with the earlier conclusion that the effect of angle of attack is negligible at high Mach numbers greatly reduces the complexity of the calibration matrix, which must be tested for supersonic flow conditions. Furthermore, these results are reassuring in that they verify the pressure model converges to modified Newtonian flow theory at high Mach numbers.
- The ill conditioning with respect to Mach number is an unavoidable consequence of the flow physics. For Mach 3 and below, where air data are required for the vehicle flight control system, potential mathematical singularities and iterative instabilities in the nonlinear estimating algorithm can be observed and this issue can be prevented by using simple logic.
- A threshold value should be set for the values of A and A' from the angle of attack estimator and sideslip angle estimator, and when it approaches zero, the result estimated using the combination of the pressure holes is removed from the final average operation.

- Increasing the number of ports from 5 to 9, there are 10 combinations of local angle of attack α_e and 55 combinations of pressure holes for the local sideslip angle β_e , the estimation result is determined by “Change Detection Criteria” and the faulty sensors or leakage issues can be removed from the final average operation. This can detect the fault from the combination and isolate them from the estimation algorithm.
- The fault detection and isolation method proposed in this research can make the FADS system redundant for one pressure sensor failure. Additionally, the accuracy of the estimates has been improved by removing the singularity issue and increasing the number of pressure ports.
- For two sensor failure on vertical meridian case, there is only one combination left in the angle of attack estimation algorithm resulting in deteriorating the results.
- For one sensor failure on vertical meridian and one sensor failure on horizontal meridian, improvement is necessary to isolate the leakage as the standard deviation could not isolate the failed sensors.
- The fault detection technique employing “Change Detection Criteria” needs to be improved when the leakage is small but the affect is considerably.
- When there are multiple sensor failures such as two sensor failure on vertical meridian or one sensor failure on vertical and horizontal meridian, additional detection criteria are necessary for fault detection.

- Based on the estimation results and understanding the sensitivity of the system, the hardware components for the system have to be selected carefully such as selection of the pressure sensors.
- For calibration purposes instead of wind tunnel experiments, Computational simulation such as CFD can be employed to increase the calibration data package for various cases.

To conclude, this algorithm needs a brush up in the Mach number convergence in the supersonic region which will improve the estimates of the dynamic pressure and static pressure. The algorithm can remove singularity and isolate the faulty sensors from the estimation but improvement in the fault tolerance capability is needed for multiple sensor failures. Also, it would be very suitable if the number of ports of the vertical meridian can be increased or if the sensors on the diagonal meridian can be incorporated in the algorithm.

REFERENCES

- [1] Hayato Tobiyama, Development Status of Experimental Winged Rocket WIRES#014-3A, 31st International Symposium on Space Technology and Science, 2017
- [2] Eiji KAMEMOTO, Detailed Design of Winged Rocket WIRES#015 with Liquid Methane Engine, 31st International Symposium on Space Technology and Science, 2017
- [3] Takahiro Fujikawa, Research and Development of Winged Reusable Rocket: Current Status of Experimental Vehicles and Future Plans, Asia-Pacific International Symposium on Aerospace Technology, 2017
- [4] Yonemoto, K. et al., Recent Development of Flight Demonstrators for Reusable Suborbital Technologies and It's Application Proceedings of the 69th International Astronautical Congress, IAC-18-F2.6.2 (11 Pages), 2018.
- [5] 高木亮治, 滝沢実, HYFLEX における ADS 計測, 航空宇宙技術研究特別資料 32 号, 1996.
- [6] Tashiro Shinichi, Yoshiki Haruo, "Flow Measurement of Dynamic and Static Pressure Gradients by means of a Multi-hole Yaw meter", Institute of Industrial Science, University of Tokyo, 33(9), pp. 384-387, 1981.
- [7] Suenaga Hisashi et al, "Wing-tip Vortex Measurement by 7-hole Probe", National Aerospace Laboratory materials, 765, pp. 2-5, 2002.
- [8] Larson, Terry J., Timothy R. Moes, and Paul M. Siemers, III, Wind-Tunnel Investigation of a Flush Airdata System at Mach Numbers From 0.7 to 1.4, NASA TM-101697, 1990.
- [9] Whitmore, S. A., Cobleigh, B. R., and Haering, E. A., Design and Calibration of the X-33 Flush Airdata Sensing (FADS) System, NASA TM-1998-206540, 1998.
- [10] Brent R. Cobleigh et al., Flush Airdata Sensing (FADS) System Calibration Procedure and Results for Blunt Forebodies, NASA, pp.1-9, 1999.

- [11] Stephen A. Whitmore et al., Design and Calibration of the X-33 Flush Airdata Sensing (FADS) System, NASA, pp.1-31, 1998.
- [12] Anderson, J. D., Hypersonic and High Temperature Gas Dynamics, Second Edition, AIAA, pp. 306-312, 2006.
- [13] 忽那祐輝, 耐故障性フラッシュ型エアデータセンシングシステム (FADS) の開発と校正手法の研究, 九州工業大学大学院 修士論文, 2015.
- [14] 森山大亮, 有翼ロケット実験機に搭載するフラッシュ型エアデータセンシングシステムの設計, 九州工業大学 学位論文, 2017
- [15] Cary, John P. and Earl R. Keener, Flight Evaluation of the X-15 Ball-Nose low-Direction Sensor as an Air- Data System, NASA TN D-2923, 1992
- [16] Siemers, Paul M., III, Martin W. Henry, and James B. Eades, Jr., “Shuttle Entry Air Data System (SEADS) Advanced Air Data System Results: Air Data Across the Entry Speed Range,” Orbiter Experiments (OEX) Aerothermodynamics Symposium, CP 3248, Part 1, pp. 49–78, 1995.
- [17] Currie, I. G., Fundamental Mechanics of Fluid, McGraw-Hill Book Company, New York, 1974.
- [18] Anderson, John D., Jr., Hypersonic and High Temperature Gas Dynamics, McGraw-Hill Book Company, New York, 1989.
- [19] Whitmore, Stephen A., Roy J. Davis, and John Michael Fife, In-Flight Demonstration of a Real-Time Flush Airdata Sensing (RT-FADS) System, AIAA-95-3433, 1995.
- [20] Whitmore, Stephen A., Roy J. Davis, and John Michael Fife, In-Flight Demonstration of a Real-Time Flush Airdata Sensing System, AIAA Journal of Aircraft, vol. 33, no. 5, pp. 970-977, 1996.
- [21] Shapiro, Ascher H., The Dynamics and Thermodynamics of Compressible Fluid Flow, Volume I, John Wiley Sons, New York, pp. 83–88, 154, 1953.
- [22] Haering, E. A., Jr., Airdata Calibration Techniques for Measuring Atmospheric Wind Profiles, Journal of Aircraft, Vol. 29, No. 4, pp. 632–639, 1992.

- [23] V. Venkata Subramanian, A review of process fault detection and diagnosis, Part I: Quantitative model-based methods, *Computers and Chemical Engineering* 27 293 / 311, 2003.
- [24] Whitmore, Stephen A., and Timothy R. Moes, Failure Detection and Fault Management Techniques for a Pneumatic High Angle of Attack Flush Airdata Sensing (HI-FADS) System, NASA TM-4335, 1992.